Pedro Miguel Rocha Carneiro

Architecture optimization of electromagnetic energy harvesting

Otimização da estrutura de geradores eletromagnéticos

Pedro Miguel Rocha Carneiro

Architecture optimization of electromagnetic energy harvesting

Otimização da estrutura de geradores eletromagnéticos

Dissertação apresentada à Universidade de Aveiro para cumprimento dos requisitos necessários à obtenção do grau de Mestre em Engenharia Mecânica, realizada sob a orientação científica do Doutor Marco Paulo Soares dos Santos, professor auxiliar convidado do Departamento de Engenharia Mecânica da Universidade de Aveiro e do Doutor Jorge Augusto Fernandes Ferreira, professor auxiliar do Departamento de Engenharia Mecânica da Universidade de Aveiro.

o júri / the jury

presidente / president

Professor Doutor Vítor Manuel Ferreira dos Santos
Professor Associado com Agregação da Universidade de Aveiro

vogais / examiners committee

Professor Doutor Raul Manuel Pereira Morais dos Santos
Professor Associado com Agregação da Escola de Ciências e Tecnologia da Universidade de Trás-os-Montes e Alto Douro

Doutor Marco Paulo Soares dos Santos
Professor Auxiliar Convidado da Universidade de Aveiro (orientador)

acknowledgements

Paulo Coelho once said "When you are enthusiastic about what you do, you feel this positive energy. It's very simple.". I only wish the concept of electromagnetic energy harvesting systems were that easy. Fortunately, I have had the privilege of being guided by Professor Marco Santos, to whom I owe all the patience, knowledge and spectacular mentoring skills and without whom this thesis would not be pass the form of a mere dream of an enthusiastic student. All my gratitude goes to you. Another word of appreciation goes to my co-adviser Professor Jorge Ferreira for his very useful suggestions on how to improve this work, giving a very important contribute for shaping it in the final product. I can't also disregard the opportunity to acknowledge the care of Renato, who started clearing this path one year ago and was always ready to help me along the journey. I would also like to thank my incredible girlfriend, who has had an infinite and unspeakable amount of patience for the last months. All the smiles and encouragement words were crucial for me to keep pushing forward. To my friends, because life can't always be about work, and who were always there to fill in the pauses with laughter and companionship. The final word goes to my family, to whom I can't thank enough. They have put up with me in the most stressful situations, loving me, supporting me and rooting for me even when I could not be as present as I would wish. You are the best. Behind every great play there is a whole set of fundamental people that one can easily forget, and this thesis is no exception. Thank you all for the amazing support and for always believing this would be possible.

palavras-chave

Geração de energia, gerador eletromagnético, levitação magnética, otimização do desempenho, arquitetura adaptativa, metodologia de otimização.

resumo

A importância dos sistemas de geração autónoma de energia tem vindo a crescer significativamente na comunidade científica, visando solucionar a insatisfação perante as soluções atuais de fornecimento de energia. Este trabalho foca-se na otimização dos sistemas eletromagnéticos de geração de energia com arquitetura em levitação magnética. Na literatura estão descritos diferentes tipos de abordagens para modular, simular e analisar a dinâmica das componentes mecânica e elétrica destes transdutores. Contudo, nenhuma metodologia se mostrou adequada para otimizar o desempenho destes geradores não lineares, principalmente na ocorrência de excitações diferentes da qual foi geometricamente projetado. O principal objetivo deste estudo é a maximização do desempenho destes geradores, através do desenvolvimento de uma metodologia de otimização geométrica. Desenvolveu-se uma ferramenta de otimização para controlar a dinâmica do(s) íman(es) em levitação, tanto para excitações conhecidas *a priori*, como para excitações variáveis. Usando um modelo que aborda analiticamente a dinâmica fundamental destes geradores, foi variada a frequência, aceleração, comprimento do gerador e a massa do(s) íman(es) em levitação. O comprimento adaptativo ótimo foi explorado a partir da análise paramétrica, permitindo deste modo obter maiores eficiências face a variações nos padrões de excitação.

keywords

Energy harvesting, electromagnetic generator, magnetic levitation, performance optimization, adaptative architecture, optimization tool.

abstract

The importance of autonomous energy harvesting systems has been rising among the scientific community. These systems are seen as the answer for the dissatisfaction felt towards the actual energy harvesting devices. Different approaches to modulate, simulate, and analyse the mechanical and electrical dynamics of these transductors are described in the literature. However, no methodology has been proved effective in the optimization of these non linear generators' performance, especially in what the occurrence of different excitations than the ones to which it was geometrically projected is concerned. The present thesis focus in the optimization of energy harvesting from the oscillations of magnetic levitation. The main goal of this work is to maximize the harvesters' performance. This was accomplished through the development of a geometric optimization tool, by means of a sophisticated method that controls the levitating magnet's dynamics for either *a priori* known or variable frequencies. Based on a model that analytically approaches the fundamental dynamics of these harvesters, the frequency, acceleration, length of the generator and mass of the levitating magnet(s) were varied. The optimal adaptive length was examined, which allowed a higher efficiency when faced with variations in the excitation patterns.

Contents

List of publications

This paper was published throughout this work. Two more articles are expected to be written and published in international journals in the scope of this research.

P. Carneiro, Marco P. Soares dos Santos, Jorge A. F. Ferreira (2018). *"Levitação magnética na geração autónoma de energia"*, Proceedings of the 1st Congresso do Centro de Tecnologia Mecânica e Automação, Aveiro, Portugal, June 11, pp. 20.

Terminology

$a_1, a_3, a_5, a_7,$ $a_9, a_{11},\ a_{13}$	electromechanical polynomial coefficients
a_c	half of depth of a block magnet at the origin
A	area of the coil turn
A_c	half of depth of a block magnet centered in $(\alpha_c, \beta_c, \gamma_c)$
A_z	external excitation amplitude
b_c	half of length of a block magnet at the origin
B	magnetic field density
B_c	half of length of a block magnet centered in $(\alpha_c, \beta_c, \gamma_c)$
B_r	residual magnetic flux density
c	total damping coefficient
c_{air}	air damping
c_c	half of height of a block magnet at the origin
c_e	electrical damping
c_{fr}	friction damping
c_m	mechanical damping
C_c	half of height of a block magnet centered in $(\alpha_c, \beta_c, \gamma_c)$
d_0	distance between the levitating and the bottom/top magnet
$E(k)$	complete elliptic integral of the first kind
f_{bw_n}	break-away forces for negative $\dot{y}$
f_{bw_p}	break-away forces for positive $\dot{y}$
f_{CO_n}	Coulomb forces for negative $\dot{y}$
f_{CO_p}	Coulomb forces for positive $\dot{y}$
F_1	excitation amplitude
F_d	force of dry friction
F_{fr}	friction force

F_g	gravity force
F_{lz}	Lorentz force
F_R	repulsive magnetic force
F_{Rd}	repulsive magnetic force between the moving magnet and the bottom magnet
F_{Ru}	repulsive magnetic force between the moving magnet and the top magnet
g	acceleration due to gravity
H	magnetic field strength
I	induced current
J	equivalent linear current density
J_1	first order Bessel function
k, k_3, k_5	repulsive magnetic force polynomial coefficients
$K(k)$	complete elliptic integral of the second kind
k_{v_n}	viscous friction coefficients for negative $\dot{y}$
k_{v_p}	viscous friction coefficients for positive $\dot{y}$
l	coil length
L_i	coil impedance
L_m	length of the moving magnet
L_{mc}	distance between the moving magnet and coil
L_u	length of the top fixed magnet
m	mass of the levitating magnet
M	saturation magnetization of the block magnet at the origin
M'	saturation magnetization of the block magnet centered in $(\alpha_c, \beta_c, \gamma_c)$
M_d	saturation magnetization of the bottom fixed magnet
M_m	saturation magnetization of the moving magnet
M_u	saturation magnetization of the top fixed magnet
N	number of coil turns
N_i	number of independent multi-turn coils
N_r	number of radial turns in a coil
N_y	number of vertical turns in a coil
p	magnetic spatial period
Q	quality factor
r_i	inner radius of the coil
r_m	mean coil radius

R_c	auxiliary variable as a function of the coil parameters
R_{di}	radius of the hole of the annuli base magnet
R_i	coil internal resistance
R_l	load resistance
R_m	radius of the levitating magnet
R_{mi}	radius of the hole of the annuli levitating magnet
R_u	radius of the top fixed magnet
S	section of the wire
S_d	distance between the moving magnet and the fixed magnet at the bottom
S_u	distance between the moving magnet and the fixed magnet at the top
t	time
v_{min}	low speed region $-v_{min} < \dot{y} < v_{min}$, where $\dot{y} = 0$ was considered
V	electromotive force (voltage)
y	reference frame to describe the displacement of the levitating magnet, relative to the device
$\dot{y}$	velocity of the levitating magnet
$\ddot{y}$	acceleration of the levitating magnet
y_0	initial position of the levitating magnet
z	fixed reference frame to describe the motion of the device
$\ddot{z}$	acceleration of the device
α	electromechanical coefficient
α_c	x coordinate of the block magnet centre
α_p	parity phase equal to 0 or $\pi/2$ for an even or uneven number of alternate magnets, respectively
β_c	y coordinate of the block magnet centre
γ_c	z coordinate of the block magnet centre
μ	coulomb's friction coefficient
μ_0	free space magnetic permeability
μ_r	relative magnetic permeability
ξ	damping factor
ρ	wire resistivity
τ	magnetic moment
ϕ	magnetic flux
ω	angular frequency
ω_n	angular ressonant frequency
Ω	angular frequency of excitation

List of Figures

List of Tables

Chapter 1

Introduction

1.1 Context

Nowadays, the concept of energy harvesting system is of progressive importance in the scientific community [1]. There have been great efforts in the development of micro-systems, ultra-low power systems and high performance distributed sensor systems. Any of these generators can be attached to a load and used to power an external system for future applications in autonomous sensor operation, mobile applications, communication network, wearable devices and biomedical implants. Nonetheless, current solutions to power supply those types of equipments still cannot completely satisfy some requirements and the use of batteries continues to be a problem, as they either have a limited ability to storage energy or its replacement is impractical or inconvenient. Energy scavenging sources from the environment is increasingly becoming an interesting option for powering electronic devices, including the use of batteries with lower energy requirements [2]. Despite presenting themselves as an interesting alternative, renewable energies, such as the wind and the sun, are intermittent, leading to a complex network management (non continuous production expenses, energy storage systems development, expensive devices and installation costs) that still require improvement. Therefore, the need to exploit and develop better solutions to the non-intermittent renewable energy production endures.

Mechanical kinetic energy can be converted into useful electric energy through piezoelectric, electromagnetic, electrostatic and magnetostrictive transduction mechanisms [3].

This work is focused on the electromagnetic energy harvesting systems using magnetic levitation architectures. They hold potential for the implementation of high performance energy harvesting for a wide range of technologies due to their distinctive properties, such as their easy application, non-complex design and ability to operate autonomously with stable performances for long periods of time, due to the reduced maintenance requirements [4].

The basic configuration of these systems relies on a hollowed structure tube, 3 permanent magnets and a coil. The polarity of the magnets is disposed so that the levitating magnet experiences a repulsive force due to the fixed magnets, which are attached to the extremities of the container [5]. A portion of the cylinder is wrapped in a multilayer coil around the outer surface of the container [4]. Several variations of this model have already been proposed concerning structure geometry (circular, rectangular), number of levitating magnets (up to 4), number of coil windings (up to 5) and geometry of the magnets (spherical, cylindric, block

and ring). In addition, guidance systems have also been considered in levitation magnets.

When an acceleration is applied to the device, the levitating magnet oscillates in the guided container, moving relative to the coil and causing the magnetic flux through the coil to change [6]. In the best-case scenario, the frequency of the moving magnet matches the resonant frequency and thus the power output is maximized [5]. However, this only happens for harmonic mechanical inputs with a dominant frequency [7]. Morever, low frequency excitations add significant challenges to maximize energy harvesting [8]. In fact, it is difficult to match low frequencies while keeping the structure as minimal as possible [9].

There is no scientific description of a tool that stipulates the harvester's performance according to specific constructive measurements and external excitations. The geometrical optimization is of paramount importance in order to maximize the harvester's behavior. Among all the parameters prone to optimization, the generator's optimal length ought to be explored, since it can be used to fulfil the adaptability requirements to excitation variations. Furthermore, it presents itself as a sophisticated method to control the levitating magnet's dynamics.

It is important to notice that it is hard to ensure optimal performances if generators are not intelligently controlled. Since the external excitation are usually not known *a priori* and present time-variating patterns, a suitable generator geometry must be designed, so the levitating magnet can easily vibrate ensuring resonant conditions [10]. When using linear system models, geometric optimization and adaptative positional control of components prior to fabrication cannot be carry out, as such systems exhibit highly non-linear behaviour [4].

1.2 Objectives

This study aims to develop an optimization tool to design electromagnetic generators that will allow: (1) geometrical optimization to *a priori* known excitations; and (2) controlled geometrical optimization to variable excitations. In order to accomplish this goal, a method capable of maximizing the efficiency of these transducers, including for variable excitation patterns, is presented.

This technological tool must allow to analyse the potential of adjusting the generator length according to variable excitations, variable damping coefficients and variable levitating masses, such that energy harvesting can be maximized.

As described in the literature review of the chapter 2, no similar research was already conducted by the scientific community. Some stages were required to accomplish this study, which are described in detail below:

- Identify a non-linear model for suitable energy harvesting analysis;
- Identify design parameters that are able to be optimized;
- Identify geometric constrains that must be considered prior to design optimization;
- Analyse the impact of geometric optimization on the dynamics of levitating magnet and energy harvesting of two manufactured generators.

Chapter 2

Literature Review

In order to better understand the transduction mechanism of harvesting systems using magnetic levitation, a summary and explanation of the current state of knowledge is made in this section. Relevant articles on this scope were selected, whose key findings were highlighted with the purpose of providing a constructive analysis of the methodologies and approaches of the researches. Throughout this work it was published a paper that concerns a brief bibliographic review on this type of electromagnetic generators [11].

Section 2.1 analyses different types of configurations such as the experimental procedures that validate each model. Section 2.2 is focused on the parameters that play a significant role on the dynamic governmental differential equations of motion, magnetic field from levitating magnets, repulsive magnetic force between permanent magnets, induced electromotive force from the relative motion between coil and magnet, electric current, electromechanical coupling coefficient, friction and damping forces. Each phenomenon was studied and qualitatively compacted - empirical, analytical, semi-analytical or through finite element method (FEM) - on a table that figures in the beginning of section 2.2. Likewise, each phenomenon is individually analysed, to introduce the main equations used by the authors to characterize their models.

2.1 Types of configurations and experimental validation

Constantinou, Mellor and Wilcox [12, 13] proposed an arrangement that consists of three cylindrical annuli permanent magnets, with similar poles facing each other. The two outer magnets are fixed and suspend the central magnet. To constrain the levitating magnet, a shaft is positioned throw the centre axis of the structure. A non-linear spring effect is afforded by the repulsive forces between magnets. This arrangement is shown in figure 2.1.

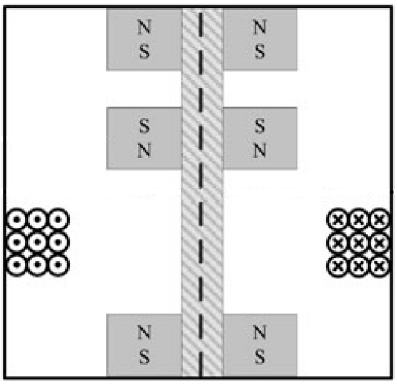

Figure 2.1: Schematic representation of the electromagnetic harvester proposed by Constantinou, Mellor and Wilcox [12, 13].

It is observed that for three different outer magnet separations, the magnet displacement varies as a function of the frame excitation frequency. It is shown the distinct measured voltages generated across the coil terminals for different separation distances between fixed magnets [12].

By comparing measured and computed frequency responses of the absolute velocity when the system is excited at a sinusoidal frame wave, the mechanical damping term is assumed to be viscous (the measurements were under open circuit conditions, eliminating any electrical damping contributions). Besides, under the same conditions and using the same methodology, the mechanical damping factor was compared from responses to calculated frequencies using a linear model of suspension, for different shaft materials. The measured and calculated absolute velocity of levitating magnet for different excitation amplitudes under unloaded conditions, open circuit voltage harvested under a frame excitation of 2g and frequency of 36 Hz, power curves at excitation frequencies of 37 and 38 Hz and frame acceleration of 2.1g are compared. Different parameters were included like the power density, the normalized power density (with respect to the input acceleration squared) and the effectiveness (a measure of how closely a specific design approaches its ideal performance and aims to compare the performances of devices as functions of their overall size) [13].

Similarly, by Mann and Sims [14] and Morgado *et al.* [6] the device comprises two fixed and an oriented levitating centre magnet, as one can see in figure 2.2. Moreover, two coils are wounded around the outer casing. The main difference between the two systems is that in [14] the ends of the tube are threaded so that, statically, it can be used to vary the spacing between the magnets.

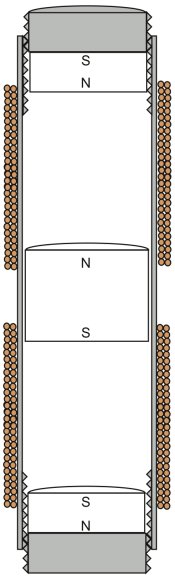

Figure 2.2: Schematic representation of the electromagnetic harvester proposed by Mann and Sims [14].

The model proposed by Mann and Sims [14] was used to perform a series of relative velocity predictions with frequency for several excitation amplitudes and two damping levels (there is a significant decrease in relative velocity associated with an increase in damping). Two important conclusions rely on the fact that those curves show the system nonlinearity which could potentially be used to provide large relatively velocities over a winder range of excitation frequencies and that the maximum relative velocity does not always occur at the location of the linear resonance. Their study also compares the relative velocity responses of the nonlinear device with those of a linear device. Theoretical predictions are validated with experimental tests. Obtained velocity predictions show that with low excitation levels, there is no hysteresis in upward or downward responses. However, the increase of excitation will cause multiple periodic attractors and hysteresis. The authors also developed an expression for the excitation frequency where the maximum power occurs.

In the model proposed by Morgado *et al.* [6], the magnetic force is represented together with a linear and a cubic polynomial approximation. Here, reasonable approximations (specially the cubic) on small fitting regions can be obtained, but if the fitting region is increased, large errors will be expressed by fitting curves. The vector field is presented where, due to the cylindrical symmetry, only the longitudinal semi-plane is represented. Also, four experimental curves of the harvested electromotive force together with a simulated one are given.

A electromagnetic energy harvester using magnetic levitation similar to the structure previously addressed is presented in [4, 10, 3, 15], but with only one coil instead of two. A schematic representation of this device is illustred in figure 2.3.

The model presented by Santos *et al.* [4] was validated comparing the steady-state and transient responses for the experimental and simulated voltage versus time, for different amplitude and sinusoidal frequency excitations. Very good agreement of these results demonstrates that results were achieved with energy errors lower than 15% and cross-correlations higher than 86%.

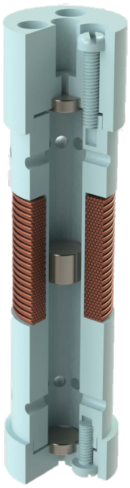

Figure 2.3: Schematic representation of the electromagnetic harvester proposed by Santos *et al.* [4].

The model proposed by Saha *et al.* [10] analyses three different types of structures: one identical to [4]; other similar to [1] in which to increase the flux linkage, two levitating magnets were used (instead of one); other similar to the latter, but the generator has only one fixed magnet to increase the displacement.

By Kecik *et al.* [3] is proposed a new definition of the coupling coefficient (inductive) which relates mechanical and electrical components. Experimental tests show that this coefficient is a nonlinear function of the magnet position and highly depends on the magnet coordinate in the coil (the maximum energy is obtained in the coil ends). It is shown the quasi-static and the dynamic tests of the coupling coefficient. The authors compared the resonance curves of magnet's displacement, velocity and recovered current for the fixed and the proposed polynomial. It is also showed the bifurcation diagram of the magnet's displacement versus the frequency of excitation for three fixed and polynomial values of coupling coefficient. Finally, it is analysed the bifurcation diagram of the coupling coefficient versus harvested current for two specific angular frequencies.

By Foisal, Hong and Chung [15] two models with an array of four generators (all of them resembling the one presented in [4] but arranged as in figure 2.4) are designed to demonstrate the possibility of harvesting energy from different environmental frequencies. In the model (a), the structure consists of all generators placed side-by-side while in model (b), the generators are placed one above the other. Here, it is studied the influence of the magnetic field intensity of the top and moving magnet on a moving mass and spring constant, and at resonant frequency. The measured open circuit voltage as a function of the frequency for different combinations of moving and fixed magnets as well as the measured output power and rectified voltage at different input frequencies are analysed.

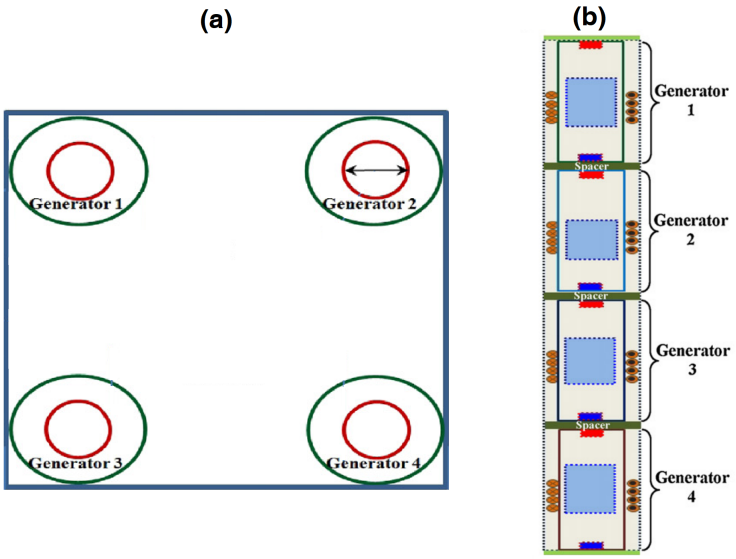

Figure 2.4: Schematic representation of the electromagnetic harvester array proposed by Foisal, Hong and Chung [15]: model (a) (top view) and model (b) (cross sectional view).

The new generator proposed by Morais *et al.* [16] is composed of two external coils wired in opposite directions with a gap between them. Inside the tube, there is a neodymium magnet and a spring; at the bottom there is also a magnet that functions as a magnetic break, as it is displayed in figure 2.5.

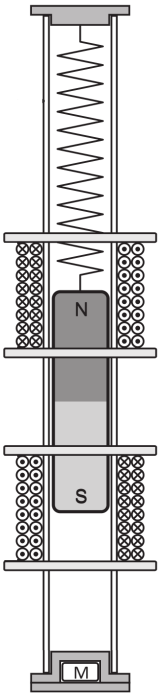

Figure 2.5: Schematic representation of the electromagnetic harvester proposed by Morais *et al.* [16].

The first prototype was composed by a coil and a magnet. Poor results were obtained due to the magnet's smaller length when compared to the coil's. This phenomena was mostly explained by the reduced weight of the inertial mass, which could not allow resonance. Moreover, the proximity of the magnet poles was also having a negative impact on the results - the coil's signal had an amplitude, positive and negative, smaller than the one measured in each separated coil. As a result, the poles of the magnet were working against each other in what concerns the coil. To reduce or eliminate the opposite effects, the distance between the poles was increased through the implementation of a longer magnet so that the magnetic field lines became almost perpendicular to the wiring direction of the coil. Careful design optimizations led to the construction of a new generator without increasing the initial volume. The effects on the output voltage were compared in the two configurations. The transducer's theoretical and practical voltage and power evolution for a set of loads and different external excitation frequencies were evaluated.

A new electromagnetic harvester model, with block magnets, was proposed by Berdy, Valentino and Peroulis [17, 5] and harvest one of the highest reported power densities. This specific structure's shape (figure 2.6) allows more flexibility in design compared to the typical cylindrical magnet devices (allows it to be thinner). It was implemented to harvest energy through human walking. The fixed magnets could be (optionally) at the top end of the tube, depending on the orientation of the device with respect to the gravity.

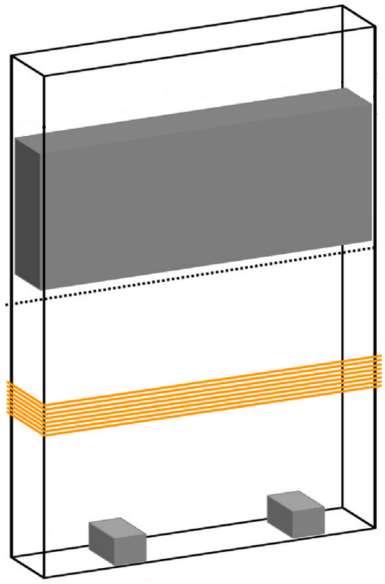

Figure 2.6: Schematic representation of the electromagnetic harvester proposed by Berdy, Valentino and Peroulis [17, 5].

Berdy, Valentino and Peroulis [17] added a term for dry friction damping to the parasitic damping (as it is typically modelled as viscous damping). A significant difference is the inclusion of both viscous and dry friction dampings. The model was implemented and was computed using *Simulink*. The static displacement and resonant frequency calculations were repeated for several different fixed magnets lengths. The modelled and measured open circuit ringdown waveforms were analysed. In order to evaluate the optimal operating frequency,

the open circuit voltage amplitude was found frequency at 0.05g excitation acceleration. To estimate the optimal resistance and frequency to maximize RMS[1] power output, the resistive load was swept while also using several frequencies between 6.3 and 6.6 Hz. Fixing the frequency in 6.4 Hz, the coil location was swept to certify that the device was assembled in the best possible way. As expeted the results show a sudden decrease in voltage at frequencies slightly below the peak. The error was justified due to the simplification of the damping parameter.

Two main factors were explored in order to improve the device performance by reducing parasitic damping. Two container sections are studied and consist of a container with and without a guide rail - the purpose of the guide rail is to minimize the contact area of the container with the levitating magnet and, consequently, to achieve a lower damping. As the coefficients of friction vary between materials and the container material is limited to electrical insulators (conductive materials could induce eddy currents), Berdy, Valentino and Peroulis [5] made containers of acrylic and polytetrafluorethylene (also known as Teflon). A third effect studied is the angle of attachment and how does this affects power output and damping. For that, three different apparatuses on the shaker instrumented with accelerometer: vertical, 15 angle offset and 30 angle offset conditions were tested. For all three containers (acrylic, no rail; acrylic, with rail; Teflon, with rail) mounted in three different configurations: (i) the open circuit ringdown waveform was captured; (ii) a resistance was loaded to the device and the RMS power was found; the resonant frequency was also analysed and the output power for each device was measured for accelerations between 0.05g to 0.2g. For the first time, the power output was studied when placed on 10 human participants while walking and running on a treadmill from 3.2 km/h to up to 7 km/h. An acceleration waveform and its Fourier transform are shown. The measured and calculated voltage across the load for one participant are compared, as well as the error between them. There was observed a large variation in the power harvested between participants and it was validated by ploting the step frequency as function of walking speed, acceleration amplitude and frequency of the five harmonics of the step frequency and power versus 3^{rd} harmonic frequency with 3^{rd} harmonic acceleration amplitude.

The energy transducer proposed by Dallago, Marchesi and Venchi [1] consists of four magnets, two movable and two fixed, inside a Teflon tube. The generator proposed by Wang *et al.* [18] is similar, but it comprises three levitating magnets. In these transducers, the levitating magnets are disposed so that the opposite poles are facing each other, as one can see in figure 2.7.

In [1], the damping was estimated on a prototype. Initially, the quality factor was analysed. The amplitude of the applied acceleration was fixed at 1g and the peak of the induced voltage was measured, while variating the frequency. In a no-load condition, a comparison was made between the simulated and the measured voltage and the position and the flux linkage versus time was plotted. To better understand its behaviour an analysis to the damping factor was carried out by simulating the frequency response in terms of the peak of the induced voltage at various damping factors. As Lorentz's force was considered, and to demonstrate the impact of this phenomena on model accuracy, the peak load voltage for a given acceleration amplitude and frequency while variating the load resistance was evaluated. The maximum error between the measurement and the simulations without the Lorentz's force varies between 20% and

[1]root mean square

80%. Considering an optimum load resistance (similar to coil resistance) the error drops to 6% at resonant frequency. Finally, it is compared the mean power delivered to the load at the resonant frequency, as function of the load resistance with and without the Lorentz's force.

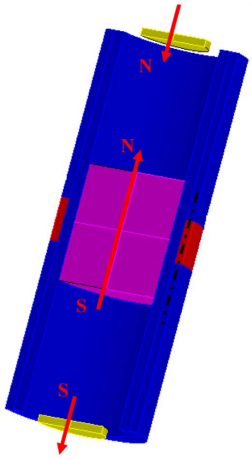

Figure 2.7: Schematic representation of the electromagnetic harvester proposed by Dallago, Marchesi and Venchi [1].

Wang *et al.* [18] analyse the difference between same pole and opposite pole facing each other, in terms of the distribution of the magnetic field and generated voltage. They simulated the voltage responses for forward (maximum relative error lower than 15%) and reverse frequency sweep (discrepant results in comparison to the numerical results) under different excitation levels. The voltage responses when the generator is vertically attached to the leg for three and six levitating magnets were evaluated under different velocities. Finally, the average output power was analysed for different mass at various motion speeds when the generator was attached to leg vertically and transversely, for two participants.

By Munaz, Lee and Chung [2] and Pancharoen, Zhu and Beeby [19] a similar configuration to the latter model is proposed, but with a slight modification: the magnet stack is obtained by placing several magnets together with same pole facing each other.

For different case scenarios, when the levitating structure comprises one to five magnets (keeping the aspect ratio same), Munaz, Lee and Chung [2] analyses the magnetic field and flux lines and obtained better performances when using three magnets with a minimum possible gap between magnet and coil. The different experimental configurations mentioned previously are compared with the simulation in order to understand the open circuit voltage harvested. Also, the load power and voltage are analysed in function of the load resistance. The load power is also varied with the increase of the air gap distance.

By Arroyo *et al.* [20] the evolution of the harvested power is studied as a function of its coupling and loss coefficients and its mechanical quality factor. The evolution of the power is observed as a function of the normalized angular frequency and load coefficient, for several modified coupling coefficients and with a defined mechanical quality factor and the product between modified coupling coefficient - mechanical quality factor and the load coefficient for several losses coefficient. Additionally, the power and the respective phase difference

between the mass displacement and the input acceleration is shown. Then, the optimal load coefficient was analysed as a function of the product between modified coupling coefficient and mechanical quality factor for several resistive losses. They analyse the levels of power that can theoretically be harvested. The authors also compared the calculated and measured power as a function of the load coefficient. Additionally, power is plotted as function of the losses coefficient, for a defined mechanical quality factor.

By Haroun, Yamada and Warisawa [9] a novel micro-electromagnetic vibration energy harvester based on free/impact motion is presented, as it can be seen from figure 2.8. The device consists of a thin walled tube, closed at both ends by two thin washers, comprising a cylindrical (it can also take other shapes) permanent magnet inside and a small gap in between. Copper wire is wounded over the tube forming a multiple layer winding. By driving an input vibration directly connected to the vibration source, the magnet can move freely and collide with end washers (stoppers) so that electrical voltage is harvested.

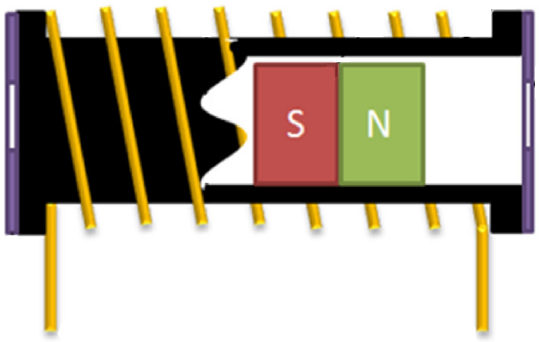

Figure 2.8: Schematic representation of the electromagnetic harvester proposed by Haroun, Yamada and Warisawa [9].

Here, the analysis is made with horizontal vibrations and it is important to notice that exists four modes of tube/magnet relative motion forms. Sticking mode appears at very low input accelerations and both tube and magnet move together (no relative motion appears). Free mode can start by increasing the input acceleration. The relative displacement occurs, but its amplitude is not large enough to allow the magnet to reach both stoppers periodically. Increasing the acceleration indicates that the impact mode is activated and the magnet can reach both stoppers periodically. Besides that, the magnet can also make few impacts on one stopper followed by other consecutive impacts with the other stopper, which they called the multiimpact mode. Therefore, the predicted output voltage versus time is shown at different motion modes and the predicted relative displacement at different input amplitudes and frequencies. Is also analysed the existence region of each mode of motion according to the input amplitude and frequency. Frequency and amplitude thresholds of impact mode decreases by decreasing the magnet stroke. The authors show the evolution of predicted flux rate with respect to the relative displacement for different coil lengths. At constant frequency, increasing the amplitude after exceeding the free mode threshold increases the relative velocity, as well as the relative displacement. It is demonstrated the RMS of the predicted output voltage and power with the input acceleration, under a known frequency. The impact and travelling times and how they changed with the input amplitude is showed. Two experiments were conducted: in the first, four prototypes having identical sizes and coils,

but different magnet shapes; the second is performed using two different size prototypes, with the same magnets but different number of coil turns. The RMS voltage and power produced versus frequency for each prototype are measured. Then the measured and predicted output voltage over a range of frequencies is compared. Finally the RMS measured power and power density of each prototype at a defined frequency over the range of input amplitudes is shown.

A new design of the first completely orientation-independent magnetic levitation energy harvester for low frequency was proposed by Gutierrez *et al.* [21] and is representated in figure 2.9. A free moving disk magnet lies on a two-dimensional plane allowing radial movement. A circular sidewall exists to constrain the centre magnet and hold fixed magnets. To provide a spring force, which returns the free magnet to an equilibrium position, stationary axially magnetized cuboidal magnets are distributed around the circumference of the sidewall. The casing is machined out of Teflon for its low friction coefficient.

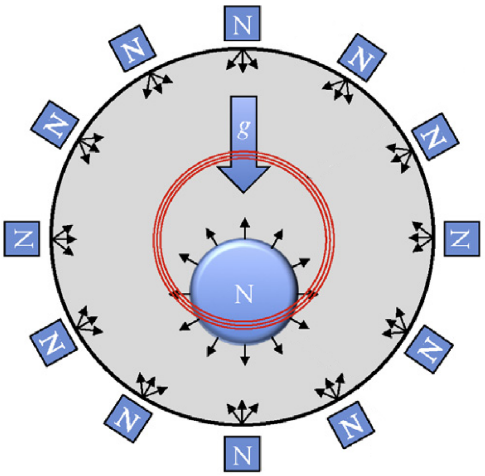

Figure 2.9: Schematic representation of the electromagnetic harvester proposed by Gutierrez *et al.* [21].

The authors compared the simulated and measured ringdown tests conducted at two starting heights above the centre under open circuit load and conducted at a starting height above the centre under known load (in this last one, significant electromagnetic damping from FEM is verified). Error as function of friction parameters was presented. The power delivered to a known load as function of coil radius and location on the harvester casing is shown as well as the power output under defined load and frequency as function of radius to perimeter magnets. It is shown, under constant excitation, the measured and modelled power delivered to varying load sizes. An analysis to the power transferred to a load as function of frequency for two acceleration values and as function of maximum excitation acceleration, under a specific frequency is conducted. Additionally the power evolution to a known load as function of device rotation was demonstrated.

An electromagnetic energy harvester model that uses two flux-guided magnet stacks to harvest energy from common-body-induced motions such as hand-shaking, walking and slow running was proposed by Halim *et al.* [22]. The design aims to up-convert the low-frequency vibration generated by human-body-induced motion to a high-frequency vibration by

mechanical impact of a spring-less structure. Before constructing the prototype, the authors analysed the best configuration for the levitating magnets by simulating different magnetic structures: single magnet, two magnet stack without a spacer and two magnet stack with a spacer (opposite poles facing each other and like-poles facing each other). As shown in figure 2.10, it consist of two front-facing high-frequency generators that are consecutively excited by a freely-movable inertial mass. Each high-frequency generator is attached to one end of a helical compression spring and is constituted by a spacer and with same poles facing each other. The movable mass is a non-magnetic metal ball that couples the low-frequency vibrations generated and transfers the kinetic energy to the spring-mass-damper systems by mechanical impact. Figure 2.10 (b) presents a simplified structure.

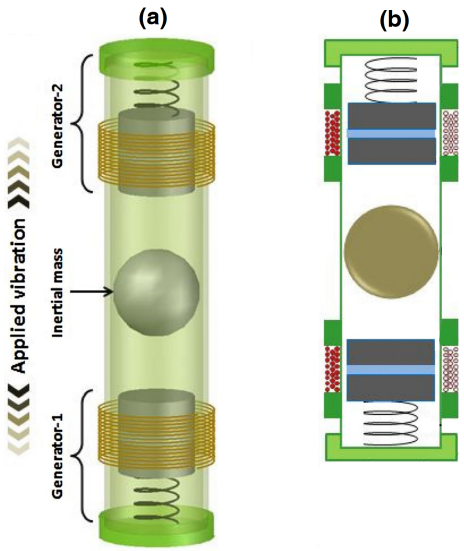

Figure 2.10: Schematic representation of the electromagnetic harvester proposed by Halim *et al.* [22].

It was observed that the flux densities of this magnetic structure decrease with the increase of the spacer thickness. To each individual generator and the series connected generators, the open circuit voltage waveforms harvested was compared, as well as the RMS voltage and average power on various load resistances. It is analysed the instantaneous power waveforms across the optimum load resistance generated by the series connected generators.

The model proposed by Masoumi and Wang [23] investigates the repulsive magnetic scavenger, which is capable of harvesting ocean waves energy with a unique repelling permanent magnet array (provides a stronger and more uniform magnet field, compared to its attracting magnetic counterparts). The levitating magnets are stacked together around a threaded rod so that the same pole is facing each other, and the two fixed magnets are arranged as in the usual configuration (it works also as braking mechanism when high amplitude vibrations occur). The arrangement is exhibited in figure 2.11.

In order to validate the model, due to different gap fillers (material used to fill the gap between the levitating magnets), a comparison between the normal flux density ranging from a carbon steel with a very low relative permeability to a 99.95 percent of iron with a high permeability is made. Metal filling increases the magnetic field intensity more than that of air

filling; however, there is no noticeable difference between metals with different permeabilities. The different frequency responses of the device (under the assumption of some parameters for nondimensional force values and electric damping values) is plotted. The natural frequency versus maximum displacement of the magnet stack is analysed during the vibration of the system. The repulsive magnetic scavenger device was tested and the voltage under sinusoidal excitation force for different excitation frequency for 0.2 s was adressed. Aditionally, the voltage with different amplitudes and a specific frequency is presented.

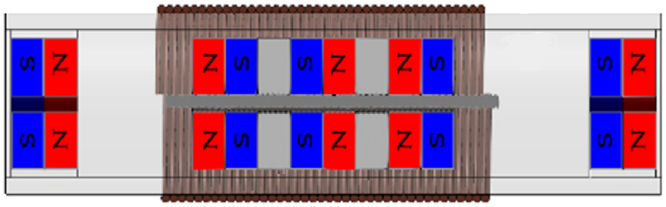

Figure 2.11: Schematic representation of the electromagnetic harvester proposed by Masoumi and Wang [23].

It was proposed a multi-coil multi-magnet multi-spacer configuration of an electromagnetic harvester system by Saravia, Ramrez and Gatti [24, 25] and Geisler *et al.* [7]. The main difference between the previous model [23] and the involved ones is that these have multi-coil windings wounded around the outer casing, as one can see in figure 2.12.

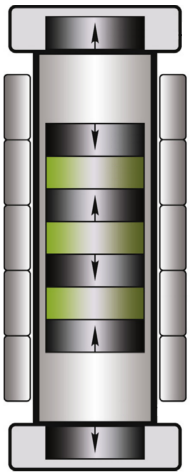

Figure 2.12: Schematic representation of the electromagnetic harvester proposed by Saravia, Ramrez and Gatti [24, 25].

Saravia, Ramrez and Gatti [24, 25] made a comparation of the flux variation for four magnet stack and three spacers configuration vs a seven magnet stack configuration. As expeted, the magnetic flux changes its shape as the stack moves closer to the end magnet. It is observed the simulated and measured voltage signals at a specific operative frequency and viscous damping coefficient for different friction coefficients. The correlation of the voltage signal between the experimental and the simulation for one period of motion for a specific frictional damping coefficient was obtained. The same analysis is made setting the viscous

damping (for a greater base excitation). It is analysed the correlation of the peak voltage for an known input acceleration, the average power and the peak power between the proposed computational approach and the physical experiment.

The model proposed by Geisler *et al.* [7] aims to develop a method to optimize an electromagnetic harvester which converts the low-frequency body motion to power wireless body sensors. The maximum peak-to-peak displacement and optimal average electrical power was observed over the system's natural frequency in the unconstrained case and with 5 cm peak-to-peak displacement limitation. Also, it is analysed the optimal electrical damping coefficients in function of the natural frequency for the unconstrained and constrained cases. The authors observed: the average load power over simulation frequency, under a constant acceleration; the average electrical power in the optimal load versus the treadmill running speed, for various combinations of repulsive magnets; the 'linear model' figure of merits of the tested prototype relative to two different mass containments and the optimal electric damping coefficient associated to the linear generator. Finally, they tested the prototype at different locations and different running speeds to analyse the average harvested power.

In the work conducted by Nammari and Bardaweel [8] it was investigated some of the design issues and limitations of traditional magnetic levitation energy harvesters such as damping schemes and stiffness nonlinearities. The proposed harvester in figure 2.13 consists of a levitated magnet placed between two stationary top (optional) and bottom permanent magnets. The main difference is the levitating magnet attached to (linear) mechanical springs from the wall sides. A stationary coil is fixed around the rest position of the movable magnet. This has several advantages such as the ability to align the levitated magnet along the stationary magnet's common axis. Since the magnetic springs present weak nonlinearity over moderate displacements, the added oblique springs from the side walls induce a negative stiffness mechanism while enhancing the total nonlinearity of the energy harvester.

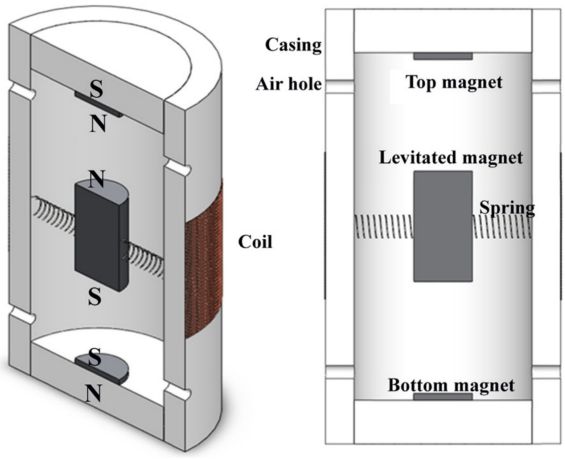

Figure 2.13: Schematic representation of the electromagnetic harvester proposed by Nammari and Bardaweel [8].

The magnetic force versus displacement considering disc and ring magnets was evaluated. It is analysed the force and stiffness for different non-dimensional quantities. Again, the estimated nonlinearity of the system is analysed, varying the linear stiffness

parameter, nonlinear stiffness parameter and spring inclination. Also, the analysis of the non-dimensional potential energy varying the same variables was conducted. Finally, it is analysed the power versus frequency graphic.

The energy transducer proposed by Nammari *et al.* [26] presents a non-resonant magneto-mechanical vibration energy harvester (figure 2.14). The levitating magnet is guided using 4 rubber oblique mechanical springs, which introduce geometric, negative and nonlinear stiffness and improves the harvester's response towards lower frequency range. The top part contains latches, air holes and a fixed upper magnet attached to an adjustable screw; the bottom part contains air holes, springs, a levitated magnet, two coil windings and a fixed lower magnet attached to an adjustable screw.

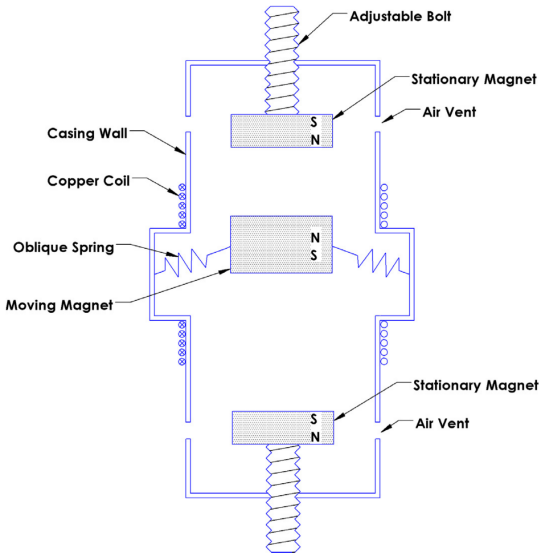

Figure 2.14: Schematic representation of the electromagnetic harvester proposed by Nammari *et al.* [26].

The authors tested the effect of inclination angle in oblique mechanical spring forces versus displacement graphic. It is analysed the measured and modelled potential energy as function of displacement. They also showed the measured and modelled generated voltage and power as function of the frequency for three different excitation acceleration.

2.2 Transduction mechanisms

This section aims to presents an intensive analysis to the phenomena that play a significant influence on the response of the magnetic levitation harvester dynamics.

Twenty one of the twenty four models considered in Section 2.1 were selected (provided by nineteen authors). The overall analysis of the modeling methodologies considered by all authors are detailed in table 2.1.

Some models presented in the previous section were not included in the present section, because their innovative architecture configuration results in slight differences in which the behaviour of the system is concerned [8, 21, 26]. Consequently, the parameters of these models cannot be compared to the others. These three models take other factors that are not framed for this work in consideration. For instance, the model proposed by Gutirrez *et al.* [21] was excluded because the authors proposed that the levitating magnet is free to perform axial and radial movements. Similary, models considerated by Nammari and Bardaweel [8] and Nammari *et al.* [26] were excluded because their models were developed considering that the levitating magnet is attached to mechanical springs from the wall sides, and that inclusion leads, once again, to slightly different dynamic considerations.

Table 2.1: Overall analysis of the modulation methodologies considered by all authors

References	**Magnetic Field**	**Repulsive Magnetic Field**	**Voltage**	**Induced Current**	**Coupling Coeff.**	**Friction/ Damp. F**
Constantinou, Mellor, Wilcox [12]	N/D	SA	N/D	N/D	A	N/D
Constantinou, Mellor, Wilcox [13]	N/D	SA	A	N/D	A	SA/E
Saha *et al.* [10]	FEM	FEM	A	N/D	N/D	SA
Mann and Sims [14]	E	E	N/D	A	SA	A
Dallago, Marchesi and Venchi [1]	FEM	FEM	A	A	SA	SA/E
Morais *et al.* [16]	E	E	A	N/D	N/D	N/D
Morgado *et al.* [6]	SA	SA	A	N/D	N/D	E
Arroyo *et al.* [20]	N/D	N/D	A	A	SA	N/D
Foisal, Hong and Chung [15]	SA	A	A	N/D	SA	A
Munaz, Lee and Chung [2]	SA/FEM	N/D	A	N/D	N/D	N/D
Berdy, Valentino and Peroulis [17]	A	A	A	A	A	A
Berdy, Valentino and Peroulis [5]	A	A	A	A	A	A
Haroun, Yamada and Warisawa [9]	SA	N/D	A	A	N/D	A
Halim *et al.* [22]	FEM	E	A	N/D	N/D	N/D
Santos *et al.* [4]	SA	SA	SA	A	SA	A
Masoumi and Wang [23]	FEM	E	A/FEM	N/D	SA	A
Saravia, Ramírez and Gatti [24]	FEM	E/FEM	A	A	N/D	A
Saravia and Oberst [25]	FEM	E/FEM	A	A	N/D	A
Kecik *et al.* [3]	E	E	N/D	A	E	E
Geisler *et al.* [7]	SA/FEM	SA	SA	N/D	N/D	SA
Wang *et al.* [18]	FEM	E	A/FEM	N/D	N/D	A
Pancharoen, Zhu and Beeby [19]	SA	E	A	N/D	N/D	SA

N/A: not defined; SA: semi-analytical; A: analytical; E: empirical; FEM: finite element method.

2.2.1 Modeling the levitating magnet motion

The governing equations for the mechanical system are the result of a sum of forces in the vertical direction. According to the Newton's second law, the modeling include the effects due to the mass of the mover (m), the damping coefficient (c,used to represent the combined electrical and mechanical damping) and the constant (k) or variable parameter (F_R) that includes the interaction magnet force between the levitating and the fixed magnets. If the excitation vibrations are vertically driven, the effect of gravity need to be included in the analysis. Also, it is important to include the effect of the inertia force. In order to make a better approximation, some models consider the mechanical coupling coefficient (α), which relates mechanical and electrical components, while others consider the Lorentz force (F_{lz}), where the induced current gives rise to a magnetic force that opposes the motion of the moving magnet. The friction force (F_{fr}) between the moving magnet and the container's inner surface was also considered. All cases have at least two reference frames, one fixed in space, to describe the motion amplitude and frequency (z), and other that describes the motion of the centre magnet (y). Some authors provide a system reduction to a Duffing oscillator under both static and dynamic loads. The Runge-Kutta numerical method was also used to numerically solve this main equation. The equations of motion used by the authors are detailed in table 2.2.

Table 2.2: Equations of motion

Equations	**References**
$-m\ddot{z} = m\ddot{y} + c\dot{y} + ky$	[2, 10, 16]
$m\ddot{z} = m\ddot{y} + c\dot{y} + ky + \alpha I$	[1, 20]
$-m\ddot{z} = m\ddot{y} + c\dot{y} + F_R(y)$	[7, 12, 15, 18, 23]
$-m\ddot{z} = m\ddot{y} + c\dot{y} + F_R(y) + mg$	[6, 13, 19, 24, 25]
$-m\ddot{z} = m\ddot{y} + c\dot{y} + F_R(y) + \alpha I + mg$	[3, 14]
$-m\ddot{z} = m\ddot{y} + c\dot{y} + F_{fr} + F_R(y) + mg$	[5, 17]
$-m\ddot{z} = m\ddot{y} + F_{lz}(I) + F_{fr} - F_R(y) + mg$	[4]
$-m\ddot{z} = c\dot{y} + \frac{y}{\lvert y\rvert} + \frac{\dot{y}}{\lvert\dot{y}\rvert}\mu mg$	[9]
$\dot{y} = \frac{mA_z\omega_n e^{-\xi\omega_n t}}{k\sqrt{1-\xi^2}}\sin(\omega_n\sqrt{1-\xi^2})t$	[22]

2.2.2 Modeling the magnetic field

The magnetic field of the levitating magnet was mainly modelled by means of semi analytical and FEM methodologies; it was also be obtained by experimental procedures. As the magnetic field variation is the event required to drive the mechanical-electrical transduction mechanism, it is important that it is well modelled. Only few methods were proposed to predict this phenomenon, but it was found that the "equivalent" surface current model (discretization of the magnet into a finite set of current loop elements and then superimposition of the magnetic fields of each layer result) is the most accurate technique. The remaining semi-analytic deductions induce errors in the approximation of this parameter, since they use, for example, the average radius of the winding for its calculation. Even so, there are still authors who consider magnetic field constant in space. The authors who use a methodology based on finite element analysis to simulate the behaviour of this parameter exclusively mention the software used and do not make specifications about the model design. The equations mentioned by the authors to model the magnetic field are detailed in table 2.8.

Table 2.3: Equations of magnetic field

Equations	**References**
$B = \mathrm{c}^{te}$	[3, 14, 16, 20]
$B(y,r) = \mu_0 \frac{M_m}{2\pi} \int_{z+y-\frac{1}{2}L_m}^{z+y+\frac{1}{2}L_m} f(y,\dot{y})[Z_t(y,\dot{y})E(k) + K(k)]\mathrm{d}\dot{y}$ **(1)**	[4]
$B = \frac{B_r}{2}\left[\frac{L_{mc}+L_m}{\sqrt{{R_m}^2+(L_{mc}+L_m)^2}} - \frac{L_{mc}}{\sqrt{{R_m}^2+{L_{mc}}^2}}\right]$	[15]
$B(y) = \frac{B_r}{2}\left[\frac{y+L_m}{\sqrt{(y+L_m)^2+{R_m}^2}} - \frac{y}{\sqrt{y^2+{R_m}^2}}\right]$ **(2)**	[19]
$B(y) = \frac{\mu_0 \tau}{2}\left[\frac{1}{\sqrt{{r_m}^2+y^2}} - \frac{y^2}{\sqrt{({r_m}^2+y^2)^{3/2}}}\right]$	[9]
$B = \sum_{i=0}^{1}\sum_{j=0}^{1}\sum_{k=0}^{1}(-1)^{i+j+k}\frac{M}{4\pi\mu_0}\arctan\left[\frac{(x-x_i)(y-y_i)}{(z-z_k)\xi_{ijk}}\right]$ **(3)**	[5, 17]
$B = \mu_0(H+M)$	[2]
$B = \nabla \times \left(\frac{M_m}{2}\sqrt{\frac{R_m}{r}}\left[\xi k\left(\frac{k^2+h^2-h^2k^2}{h^2k^2}K(k^2) - \frac{1}{k^2}E(k^2) + \frac{h^2-1}{h^2}\Pi(h^2\|k^2)\right)_{\xi-}^{\xi+}\right]\right)$ **(4)**	[6]

The authors who appeal to FEM analysis, use the following software:

Table 2.4: Software to simulate magnetic field

Software	**References**
Finite Element Analysis Software	[10]
Flux® 2D Software	[1]
ANSOFT Maxwell Software	[18]
Finite Element Method Magnetics Software	[22, 23, 24, 25]
COMSOL Multiphysics® Software	[7]
ANSYS Finite Element Analyis Software	[2]

(1)

$$E(k) = \int_0^{\frac{\pi}{2}} \sqrt{1 - k^2 sin^2(\phi)} \mathrm{d}\phi$$

$$K(k) = \int_0^{\frac{\pi}{2}} \frac{1}{\sqrt{1 - k^2 sin^2(\phi)}} \mathrm{d}\phi$$

$$f(y, \dot{y}) = \frac{1}{\sqrt{(R_m + r)^2 + (y - \dot{y})^2}}$$

$$k = \sqrt{\frac{4 r R_m}{(R_m + r)^2 + (y - \dot{y})^2}}$$

$$Z_t = \frac{R_m^2 - r^2 - (y - \dot{y})^2}{(R_m - r)^2 + (y - \dot{y})^2}$$

(2)

$$B_r \approx \mu_0 H$$

(3)

$$\xi_{ijk} = \sqrt{(x - x_i)^2 + (y - y_i)^2 + (z - z_i)^2}$$

(4)

$$h^2 = \frac{4 R_m \rho}{(R_m + \rho)^2}; \quad k^2 = \frac{4 R_m \rho}{(R_m + \rho)^2 + \xi^2}$$

$$\xi \pm = y \mp \frac{L_m}{2}; \quad [F(\xi)]_{\xi-}^{\xi+} = F(\xi+) - F(\xi-)$$

$$K(s) = \int_0^{\frac{\pi}{2}} \frac{1}{\sqrt{1 - s \sin^2(\theta)}} \mathrm{d}\theta$$

$$E(s) = \int_0^{\frac{\pi}{2}} \sqrt{1 - s \sin^2(\theta)} \mathrm{d}\theta$$

$$\Pi(s|t) = \int_0^{\frac{\pi}{2}} \frac{1}{(1 - s \sin^2 \theta)\sqrt{1 - t \sin^2 \theta}} \mathrm{d}\theta$$

2.2.3 Modeling the repulsive magnetic force

The total magnetic force is given by the sum of the repulsive magnitude forces due to top and bottom fixed magnets. It is important to notice that changes in the magnet spacing will modify the stiffness and resonance frequency of the system. In literature, this phenomenon is commonly deduced empirically by fitting experimental measurements into a power series. In this type of analysis, the authors find the coefficients using a least-squares procedure. Another way that was proposed to compute this parameter was to apply Bessel integral functions of first order. Hybrid approaches were also considered, when analytically is computed the results from Bessel's functions and, then, results are fitted using polynomial technique. Other techniques were also used as the Coulombian or equivalent charge model, Amperian or equivalent current model, as well as the Maxwell's stress tensor method to deduce the force imposed between permanent magnets. The authors who use a methodology based on finite element analysis to simulate the behaviour of this parameter exclusively mention the software used and do not make specifications about the model design. The author's studies to model the repulsive magnetic force are based on the equations described in table 2.5.

Table 2.5: Equations of repulsive magnet force

Equations	**References**
$k = \mathrm{c}^{te}$	[16, 22]
$F_{Rd} = 2\pi R_{mi} \int_{S_d}^{S_d+L_m} \frac{JdA_{R_m,R_{di}}(y)}{dy} dy + 2\pi R_m \int_{S_d}^{S_d+L_m} \frac{JdA_{R_m,R_m}(y)}{dy} dy$ $+2\pi R_m \int_{S_d}^{S_d+L_m} \frac{JdA_{R_{di},R_m}(y)}{dy} dy + 2\pi R_{mi} \int_{S_d}^{S_d+L_m} \frac{JdA_{R_{di},R_{di}}(y)}{dy} dy$ **(1)**	[12, 13]
$F_{Ru} = \mu_0 \pi R_u R_m M_u M_m \int_0^\infty J_1(\varepsilon R_u) J_1(\varepsilon R_m) [e^{-\varepsilon(S_u+L_u)}$ $+e^{-\varepsilon(S_u-L_m)} - e^{-\varepsilon(S_u)} - e^{-\varepsilon(S_u+L_u-L_m)}] \varepsilon^{-1} \mathrm{d}\varepsilon$ **(2)**	[4, 7]
$F_R = ky + k_3 y^3$	[3, 14, 18, 19, 23]
$F_R = ky + k_3 y^3 + k_5 y^5$	[24, 25]
$F_R = \frac{\mu_0 M_m}{4\pi} \left[\frac{M_u}{{S_u}^2} - \frac{M_d}{{S_d}^2} \right]$	[15]
$F_R = \frac{MM'}{4\pi\mu_0} \sum_{i=0}^{1} \sum_{j=0}^{1} \sum_{k=0}^{1} \sum_{l=0}^{1} \sum_{p=0}^{1} \sum_{q=0}^{1} (-1)^{i+j+k+l+p+q} \phi_y$ **(3)**	[5, 17]
$F_{Ru}(y) = -\frac{M_u M_m}{2\mu_0} \sum_{i=1}^{2} \sum_{j=3}^{4} a_{i,j}^{(1)} a_{i,j}^{(2)} a_{i,j}^{(3)} (-1)^{i+j} f_{i,j}^{u}$ **(4)**	[6]

The authors who appeal to FEM analysis, use the following software:

Table 2.6: Software to simulate repulsive magnet force

Software	**References**
FE transient simulation (k=c^{te})	[10]
Flux® 2D Software (k=c^{te})	[1]
Finite Element Method Magnetics Software	[24, 25]

(1)

$$\vec{A} = \frac{\vec{a_\phi}\mu_0 Jr}{2\pi} \int_{z_1-\frac{L_m}{2}}^{z_1+\frac{L_m}{2}} \int_{-\frac{\pi}{2}}^{\frac{\pi}{2}} \frac{\sin(\dot{\phi})}{R_m} d\dot{\phi} d\dot{z}$$

$$J = \frac{B_r}{\mu_r \mu_0}$$

$$\frac{1}{R_m} = \frac{1}{R\sqrt{1 + \frac{r^2}{R^2} - \frac{2r}{R}\sin\theta \sin\dot{\phi}}}$$

(2)

$$F_{Ru} = \mu_0 \pi R_u R_m M_u M_m (I_1 + I_2 + I_3 + I_4)$$

$$I_1 = \int_0^\infty x^m e^{-(S_u+L_m)x} J_1(R_m x) J_1(R_u x) \mathrm{d}x$$

$$I_2 = \int_0^\infty x^m e^{-(S_u+L_u)x} J_1(R_m x) J_1(R_u x) \mathrm{d}x$$

$$I_3 = \int_0^\infty x^m e^{-S_u x} J_1(R_m x) J_1(R_u x) \mathrm{d}x$$

$$I_4 = \int_0^\infty x^m e^{-(S_u+L_m+L_u)x} J_1(R_m x) J_1(R_u x) \mathrm{d}x$$

(3)

$$\phi_y = -uw\ln(r-u) - vw\ln(r-v) + uv\tan^{-1}\frac{uv}{rw} - rw$$

$$u = u_{ij} = \alpha_c + (-1)^j A_c - (-1)^i a_c$$

$$v = v_{kl} = \beta_c + (-1)^l B_c - (-1)^k b_c$$

$$w = w_{pq} = \gamma_c + (-1)^q C_c - (-1)^p c_c$$

$$r = \sqrt{u_{ij}^2 + v_{kl}^2 + w_{pq}^2}$$

(4)

$$a_{i,j}^{(1)} = y_i^u - y_j^u$$

$$a_{i,j}^{(2)} = \frac{(R_m - R_u)^2}{(a_{i,j}^{(1)})^2} + 1$$

$$a_{i,j}^{(3)} = \sqrt{(R_m + R_u)^2 + (a_{i,j}^{(1)})^2}$$

$$a_{i,j}^{(4)} = \frac{4R_m R_u}{(R_m + R_u)^2 + (a_{i,j}^{(1)})^2}$$

$$f_{i,j}^u = K(a_{i,j}^{(4)}) - \frac{1}{a_{i,j}^{(2)}} E(a_{i,j}^{(4)}) + \left(\frac{(a_{i,j}^{(1)})^2}{(a_{i,j}^{(3)})^2} - 1 \right) \Pi \left(\frac{a_{i,j}^{(4)}}{1 - a_{i,j}^{(2)}} | a_{i,j}^{(4)} \right)$$

2.2.4 Modeling the electromotive force

The mechanical energy is converted into electrical energy when the magnetic field changes through the coil, inducing an electromotive force (EMF). In short, the electromotive induced force is described by the Faraday's law of induction. Most of the authors applied this concept directly, while others associated the electromechanical coupling coefficient with the magnet's velocity. When using the Maxwell-Faraday equation very good validation results are obtained for EMF modeling (open circuit). A semi-analytical approach was also used to model the coil as a set of single circular turns and a three dimensional surface bounded by a closed contour defined by each of these turns. The authors who use a methodology based on finite element analysis to simulate the behaviour of this parameter exclusively mention the software used and do not make specifications about the model design. The equations mentioned by the authors to model the electromotive force are detailed in table 2.7.

Table 2.7: Equations of induced electromotive force

Equations	**References**
$V = -\frac{d\phi}{dt}$	[1, 2, 5, 6, 9, 10, 13, 15, 17, 18, 22, 23, 24, 25]
$V = -NBl\frac{\omega_n A}{2\xi}$	[19]
$V = \frac{BlA_z\omega^3}{\sqrt{({\omega_n}^2-\omega^2)^2+(2\xi\omega_n\omega)^2}}$	[16]
$V = 2\pi\frac{\partial}{\partial t}\left(\sum_{k=1}^{N_y}\sum_{j=1}^{N_r}\int_0^{r_j} B_z(r,y_k)r\mathrm{dr}\right)$	[4, 7]

The authors who appeal to FEM analysis, use the following software:

Table 2.8: Software to simulate induced electromotive force

Software	**References**
ANSOFT Maxwell Software	[18]
Finite Element Method Magnetics Software	[23]

2.2.5 Modeling the electric current on the coil

The induced current is generally deduced by using the Ohm's law. There are models that have taken into account the coil's inductance and others who did not. In table 2.9 are inserted the proposed equations to mathematically model this phenomenon.

Table 2.9: Equations of coil induced current

Equations	**References**
$I = \frac{U}{R_i + R_l}$	[1, 5, 17]
$\frac{dI}{dt} = \frac{U - I(R_i + R_l)}{L_i}$	[3, 4, 9, 24, 25]
$\frac{dI}{dt} = \frac{U - IR_l}{L_i}$	[20]
$I(t) = -\left(\frac{\alpha}{R_l + R_i}\right) \Omega a \sin(\Omega t - \gamma)$ **(1)**	[14]

(1) in which "a" come from the equation 3.9 (p. 33)

2.2.6 Modeling the electromechanical coupling coefficient

The electromechanical coupling coefficient relates mechanical and electrical components. In literature, this parameter was usually simplified and taken as constant. This approximation was considered when the magnetic field density was modelled as constant and this assumption leads to a coupling factor with a fixed value. Although not accurate, analysis is strongly simplified. Nevertheless, some authors proposed a method to experimentally determinate α as a function of the magnet's position. The equations mentioned by the authors to model the electromechanical coupling coefficient are detailed in table 2.10.

Table 2.10: Electromechanical coupling coefficient

Equations	**References**
$\alpha = Bl$	[15]
$\alpha = NBl$	[14, 23]
$\alpha(y) = 2\pi r_m N B(y)$	[1]
$\alpha = \sum_{i=1}^{N_r} \sum_{j=1}^{N_y} k_{e\_ij}$ (1)	[5, 12, 13, 17]
$\alpha(y) = a_1 y + a_3 y^3 + a_5 y^5 + a_7 y^7 + a_9 y^9 + a_{11} y^{11} + a_{13} y^{13}$	[3]

(1)

$$k_{e\_ij} = -2\pi r_{ij} \frac{dA_{ij}}{dz}, \quad \text{with } A \text{ defined in table 2.5 } (p.\,22)$$

2.2.7 Modeling the damping coefficients

Authors have modelled mechanical and electric dampings. The mechanical damping was usually related to friction, but other damping sources were also engaged (e.g. air damping). To avoid air compression, the harvesters normally were designed with tiny holes on the extremities so that the air flux can leave the inner container, as the magnet moves in it. Even so, this phenomenon exists and hardly anyone considered it. The frictional force was already modelled using the Karnopp friction model. The latter model considers, for both negative and positive speeds the effect of different viscous friction coefficients, different break-away forces and different Coulomb forces. It also considers a low speed region, where no relative displacement occurs. Of course that the electric damping force only stands if there is a load attached to the generator. The induced current creates its own magnetic field centralized mainly inside the coil, which generates a force that opposes to the motion (plays the role of an electric damping mechanism), which in turn reduces the levitating magnet speed. This arises from the energy conservation theorem. The energy conversion must be such that the mechanical power dissipated by the electromagnetic damping is equal to the power generated. In general, the models report an analytic formula to calculate the electric damping but do not mention a formulation to define the mechanical damping. When validating the model, the damping factor is usually deduced empirically. The equations mentioned by the authors to model the damping coefficients are detailed in table 2.11.

Table 2.11: Damping coefficients

Equations	**References**
$c_e = \frac{\alpha^2}{\sqrt{(R_l+R_i)^2+(\omega L_i)^2}}$	[13]
$c_e = \frac{\alpha^2}{R_l+R_i+j\omega L_i}$	[15]
$c_e = \frac{\alpha^2}{R_l+R_i}$	[5, 14, 17, 18, 23]
$c_e = \frac{(d\Phi/dy)^2}{R_l+R_i}$	[9]
$c = c_{air} + \frac{c_{fr}}{\dot{y}} + \frac{\left(\sum \phi_i'\right)^2}{R_l+R_i+j\omega L_i}$	[24, 25]
$c(y) = \frac{N_i}{R_c+R_l}\left(2\frac{N}{N_y}\phi_{max,ave}\sin\left(\frac{\pi N_y}{p}\right)\right)^2\cos^2\left(\frac{2\pi}{p}(y_0-y)+\alpha_p\right)$ **(1)**	[7]
$c = \xi 2m\omega_n$	[10, 19]
$c = \frac{\omega_n}{Q}$	[1]
$F_{fr} = \frac{\dot{y}}{\lvert\dot{y}\rvert}F_d$	[5, 17]
$F_{fr} = \begin{cases} f_{re} & \text{if } -f_{bw_n} < f_{re} < f_{bw_p} \\ f_{co_p} + k_{v_p}\frac{dy}{dt} & \text{if } \frac{dy}{dt} > v_{min} \\ -f_{co_n} + k_{v_n}\frac{dy}{dt} & \text{if } \frac{dy}{dt} < -v_{min} \end{cases}$ **(2)**	[4]
$F_{lz} = 2\pi I \sum_{k=1}^{N_y}\sum_{j=1}^{N_r} B_r(r_j, y_k) r_j$	[4]

(1)

$$R_c = N\frac{\pi\rho}{S}\left(\frac{NS}{N_y k_c} + 2r_i\right)$$

(2)

$$f_{re} = m\ddot{z} - F_g - F_R - F_{lz}$$

Chapter 3

Method

As reviewed, a method that maximizes the generator's efficiency has not yet been developed.

3.1 Harvester's architecture

As noticed in the previous chapter, several configurations have already been proposed. The architecture assumed for the configuration of the electromagnetic generator is composed by:

- A hollowed cylindrical tube structure;
- Three cylindrical magnets;
  - ▷ Two magnets are fixed to the end extremities of the container;
  - ▷ One magnet is levitating, positioned between the fixed ones;
- A multi-coil-multi-layer is wonded around a portion of the outer container.

This choice, that well demonstrates the process of transduction, relies on its massive use in the literature (see chapter 2). This is a basic configuration and is suitable to validate the concept of customizable harvester, since it has all the necessary elements to the transduction process, but with non-complex architecture.

3.2 Model

The model proposed by Mann and Sims [14] was chosen because:

- It captures the fundamental dynamics/ behavior of the generator;
- It was experimentally validated;
- Presents the analytical resolution of the transduction process. This also provides:
  - ▷ shorter computing time;
  - ▷ lower computational cost;
    - ▷ it allows massive computation (suitable for detailed analysis).

- It was a study that provide a solid basis to further studies (it was quoted 553 times until June 30, 2018, according to the *scopus* database).

3.3 Governing equations

The schematic diagram of the levitation system adopted by the authors is shown in figure 3.1. Two references frames to the model were provided: the reference stated as z is used to describe the external applied signal, specified in terms of amplitude (A_z) and frequency (ω); and the reference stated as x describes the motion of the levitating magnet.

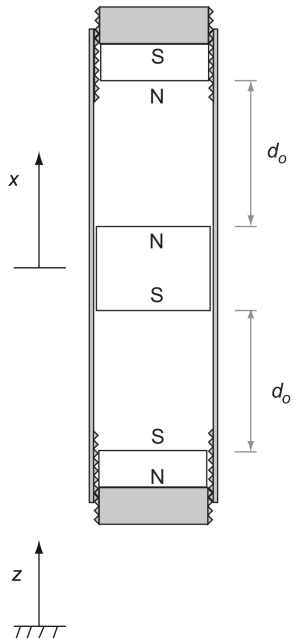

Figure 3.1: Schematic diagram of the magnetic levitation system proposed by Mann and Sims [14].

They modelled the resulting magnetic force as a cubic nonlinear spring such that the harvesting system behaves as a Duffing oscillator. So, the equivalent force-displacement curve is given by a vector summation of the restoring forces (F_R) acting on the bottom and top magnets, according to equation 3.1:

$$F_R = kx + k_3x^3 \tag{3.1}$$

where k is the linear stiffness and k_3 is the non-harmonic term.
The following governing equation is valid for undamped and unforced oscilations:

$$m\ddot{x} + kx + k_3x^3 = -mg \tag{3.2}$$

where m is the levitating magnet mass and g is acceleration due to gravity. The static equilibrium, x_e, can be found by setting the acceleration parameter to zero:

$$x_e{}^3 + \frac{k}{k_3}x_e + \frac{mg}{k_3} = 0 \tag{3.3}$$

The governing equation for the electrical circuit is obtained through Kirchoff's law:

$$I(R_l + R_i) - \alpha(\dot{x} - \dot{z}) = 0 \tag{3.4}$$

where $\alpha = NBl$ is the electromechanical coupling coefficient, N is the number of coil turns, B is the average magnetic field density, l is the coil length, $z = A_z \cos(\omega t)$ are harmonic base excitations, I is the current induced on the coil, R_l is the load resistance and R_i is the coil internal resistance, according to figure 2.2 (p. 5).

The differential equation that model the mechanical dynamics is given by:

$$m\ddot{x} + c(\dot{x} - \dot{z}) + k(x - z) + k_3(x - z)^3 = -mg \tag{3.5}$$

where $c = c_m + c_e$ is the total damping coefficient, c_m is the mechanical damping and $c_e = \dfrac{\alpha^2}{R_l + R_i}$ is the electrical damping.

In order to write the governing equations in terms of the relative displacement between the levitating magnet and the main structure, a variable change $y = x - z$ is established.

The model that describes the interplay between electrical and mechanical dynamics can then be expressed as:

$$\begin{cases} m\ddot{y} + c_m\dot{y} + ky + k_3y^3 + \alpha I + mg = \omega^2 A_z \cos(\omega t) \\ I = \frac{\alpha}{R_l + R_i}\dot{y} \end{cases} \tag{3.6}$$

Before analytically solve this system, it was rewritten as:

$$\ddot{y} + 2\xi\omega\dot{y} + \omega^2 y + \beta y^3 = F_0 + F_1 \cos(\Omega t) \tag{3.7}$$

Where the new coefficients are denoteted as:

$$2\xi\omega = \frac{c}{m} \tag{3.8a}$$

$$\omega^2 = \frac{k}{m} \tag{3.8b}$$

$$\beta = \frac{k_3}{m} \tag{3.8c}$$

$$F_0 = g \tag{3.8d}$$

$$F_1 = \Omega^2 A_z \tag{3.8e}$$

After analysing the previous equation by means of the multiple scales perturbation technique, and after introducing a polar form ($A(\tau_1) = \frac{1}{2}a(\tau_1)e^{i\phi(\tau_1)}$), they provided an analytical solution for the nonlinear system dynamics under harmonic base excitation, as follows [14]:

$$\begin{aligned} \left(\frac{3\beta}{8\omega}\right)^2 a^6 + \left(\frac{9\beta^2 F_0^2}{8\omega^6} + \frac{3}{4}\beta\left(1 - \frac{\Omega}{\omega}\right)\right) a^4 \\ + \left(\left(\frac{3\beta F_0^2}{2\omega^5}\right)^2 + \frac{3\beta F_0^2}{\omega^4}\left(1 - \frac{\Omega}{\omega}\right) + (\Omega - \omega)^2 + (\xi\omega)^2\right) a^2 - \left(\frac{F_1}{2\omega}\right)^2 = 0 \end{aligned} \tag{3.9}$$

A 1 MΩ resistence of electrical load was used to compute the electric dynamics. This was due to the fact that the model that does not take into account the electrical dynamics. However, the greater the velocity of the levitating magnet, the greater the generated current and, therefore, the larger the force that opposes the movement. Consequently, one cannot use low resistance loads when simulating the model proposed by Mann and Sims [14]. It is important to note that the maximum power is generated if the load resistence equals the internal resistance of the windings (maximum power transfer theorem). By using a high magnitude resistance, low current will flow through the circuit, which translates in significatively low electrical damping. Therefore, Mann and Sims' [14] approach is only plausible when high impedance loads are used. As a result, this study will emphasize the mechanical dynamics, in particular the levitating magnet velocity. By using a high resistance load, the behaviour of the system enhances its resemblances to an open circuit. It is expected that the current and power levels in the winding terminals to be low.

The predicted relative velocity over time is due to the term "a". Hereinafter, for each frequency, the corresponding velocity is presentad as its maximum absolute value with the notation $|\dot{y}|$, and is calculated from:

$$|\dot{y}| = |-\Omega a| \tag{3.10}$$

The formulas to get the current flowing through the electrical load and the electrical power, for each frequency is computed as:

$$I = -\left(\frac{\alpha}{R_l + R_i}\right)\Omega a \tag{3.11}$$

$$P = I^2 R_l \tag{3.12}$$

By differentiating equation 3.9 with respect to Ω and a, the frequency of maximum response (can occur away from the linear ressonance) is found as:

$$a_{max} = \frac{F_1}{2\xi\omega^2} \tag{3.13}$$

$$\Omega_{max} = \frac{3\beta}{8\omega}a_{max}^2 + \frac{3\beta F_0^2}{2\omega^5} + \omega \tag{3.14}$$

3.4 Limitations of the model

This analytical solution was achieved using, however, a simplified model since:

- B was considered constant (the average magnetic field strength along the coils was assumed);
- α was considered constant (according to the previous assumption);
- the magnetic repulsive force is restricted to a third degree polynomial approximation;
- the electrical damping coefficient was statically taken into account;
- the coil inductance was not introduced in the electrical dynamics;
- the analytical solution is only valid for $R_l >> R_i$.

Even when its limitations are taken into account, the model developed by Mann and Sims [14] was used, since it approaches the fundamental dynamics of these harvesters and provides the first analytical analysis to the problem.

3.5 Parametric analysis

Intensive computation with multiple parameter variation inputs was performed. *MATLAB* (v9.0, R2016a, *Mathworks*) was used to solve equations 3.9, 3.10, 3.11, 3.12, 3.13 and 3.14. The length, frequency, acceleration and damping factor of the generator, as well as the mass of the levitating magnet (isolated simulation) were changed. The parametric analysis follows in detail below.

3.5.1 Constant parameters

The constant model parameters used for this simulation were the same considered by Mann and Sims and are listed on table 3.1.

Table 3.1: Constant parameters

Parameter	**Value**	**Units**
m	0.0195	kg
k ($\Delta d = 0$)	35.0396	N/m
$k3$ ($\Delta d = 0$)	138400	N/m^3
d_0	37.3	mm
g	9.81	m/s^2
α	7.752	Vs/m
R_{int}	188	Ω
R_{load}	1	MΩ

3.5.2 Variation of length

- range between its actual size plus $[-d_0/2\ ,\ d_0/4]$ [mm]
  - ▷ 100 intermediary values from $-d_0/2$ to 0
  - ▷ 100 intermediary values from 0 to $d_0/4$

The curve that characterizes repulsive magnetic force changes as the structure of the generator changes. Figure 3.2 shows the force-displacement relationships when the harvester is shortened and stretched along Δd. The curve without offsets is also displayed for comparative purposes.

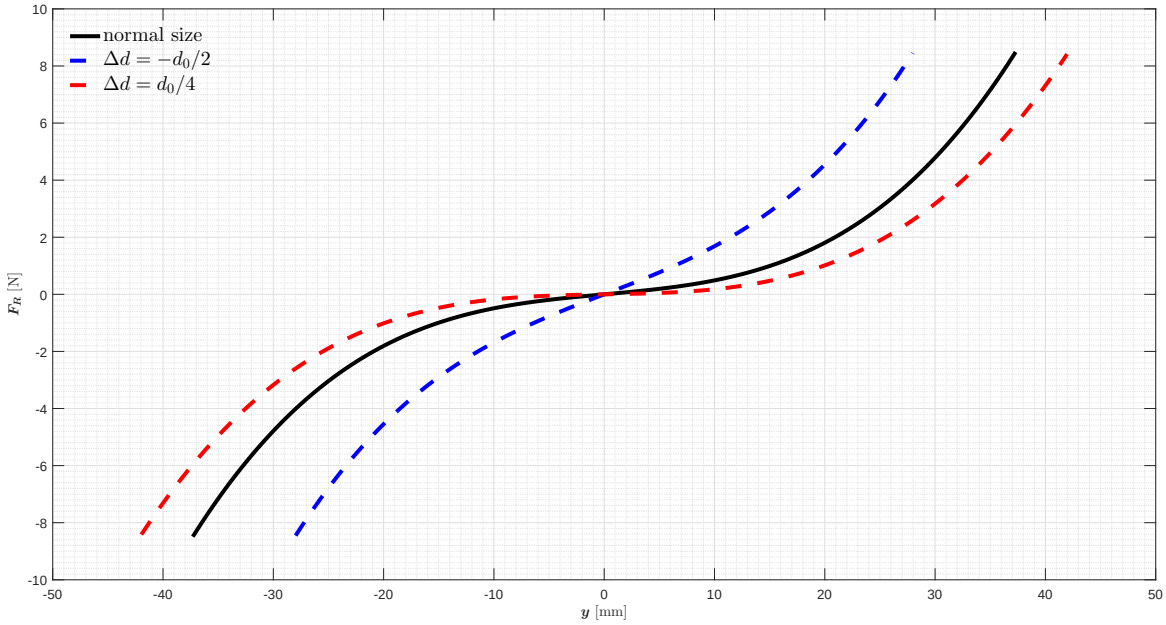

Figure 3.2: Force-displacement relationship with the generator length at its normal size (black solid line), $\Delta d = -d_0/2$ (blue dashed line) and $\Delta d = d_0/4$ (red dashed line).

A local search algorithm from *MATLAB* (unconstrained nonlinear optimization using *fminsearch* to find the minimum of the squared error function) was used to find k and k_3 parameters. After every iteration, ω and β were immediately recalculated, as they depend on k and k_3, respectively.

There are some limitations in the variation of Δd. It cannot be extended to more than $d_0/4$ mm due to the inexistence of k and k_3 coefficients combinations (and, then, the inexistance of a fitting curve approximation) that correctly describe the magnetic forces for $\Delta d > d_0/4$ mm. In the ideal curve, if Δd mm are added to the length of the generator, the half curve expressing the force for positive y's is displaced $\Delta d/2$ mm to the right. The opposite also occurrs for the region with negative y's. The central region ($-\Delta d/2$ to $\Delta d/2$) will exhibit a nearly zero force. Either a good approximation is made when the magnets are close to each other, (and it is inevitable that the coefficients have values such that for positive y's there are negative forces near the central zone, which is wrong) or it is taken into account that for positive y's only positive forces can preside. This would result in a less inclined curve at the ends of the graph, which ultimately traduces in the alteration of the magnetic properties.

The length of the transducer cannot also be reduced to less than $d_0/2$ mm, because it is impossible to find suitable curves (slope at the extremities) with only 2 coefficients. For $\Delta d < -d_0/2$ mm, the curve is altered in such a way that it becomes a straight line, which slope differs from the base curve.

$$2d_0 - \frac{d_0}{2} \leqslant 2d_0 \leqslant 2d_0 + \frac{d_0}{4}$$

$$-\frac{d_0}{2} \leqslant \Delta d \leqslant \frac{d_0}{4}$$

3.5.3 Variation of excitation frequency

- range between [0 , 100] [Hz]
    - ▷ with 3000 intermediary values altogether

In order to have a good resolution, the frequency ranged from 0 to 100 Hz with small increments.

3.5.4 Variation of the excitation amplitudes

- range between [0.1 , 8.4] [m/s^2]
    - ▷ with an increment of 0.1 m/s^2, representing 84 values of excitation amplitudes to consider

Despite the fact that an analogy is made mainly with 3 accelerations in the model proposed by Mann and Sims [14], its maximum and minimum values correspond to the limits imposed in this study. The increment refines the analysis, enabling a detailed analysis to the harvester dynamics.

3.5.5 Variation of the damping ratio

- range between [0.05 , 0.4]
    - ▷ with 3 intermediary values, corresponding to 5 values altogether

In the model proposed by Mann and Sims [14], the relative velocity responses were calculated with the damping ratio set to 0.05 and 0.09; in the experimental validation, only the damping value of 0.115 was considered. In the present parametric analysis, a wider range was analysed, since harvesters with higher coefficients than those used by the authors can be designed.

3.5.6 Variation of the levitating magnet mass

- range between [10 , 500] [g]
    - ▷ 500 intermediary values

In order to evaluate the impact of the mass of the levitating magnet on the system dynamics', it was performed 3 independent simulations. For that, the acceleration was set to 4 m/s^2 and the damping was set to 0.05. The frequency was varied from 0 to 100 Hz with 6000 intermediary small increments and the Δd was set to -d_0/2, 0 and d_0/4 mm.

3.6 Results analysis

The velocity response of the levitating magnet in the range [6, 14] [Hz] frequency for two excitation amplitudes (0.5 and 4 m/s^2) is presented in figure 3.3. In the top figure, at a low excitation level, the harvester behaves as a linear system since the velocity variable has a single periodic attractor. The bottom figure shows that increasing the external acceleration

will cause the appearance of multiple periodic attractors and hysteresis. It is noteworthy to observe the range of large amplitude responses that are provided when the system engages nonlinearity [14].

The analytical behaviour due to nonlinear phenomenon for upward frequency sweeps follow an increasing magnet relative velocity up to a maximum velocity (identified with the red cross point) and then an abrupt decrease of velocity occurs, switching back to the black line. Conversely, for downward frequency sweeps, velocity values follow the black line (from right to the left) but suddenly jumping to a maximum velocity identified with the red circle dot and continuing through the black line. This behaviour was already experimentally validated [14, 18].

If the excitation is enough to cause hysteresis, the response of the system is represented by the black line. The red circle dot is a solution achievable in both trajectories (ascending and descending).

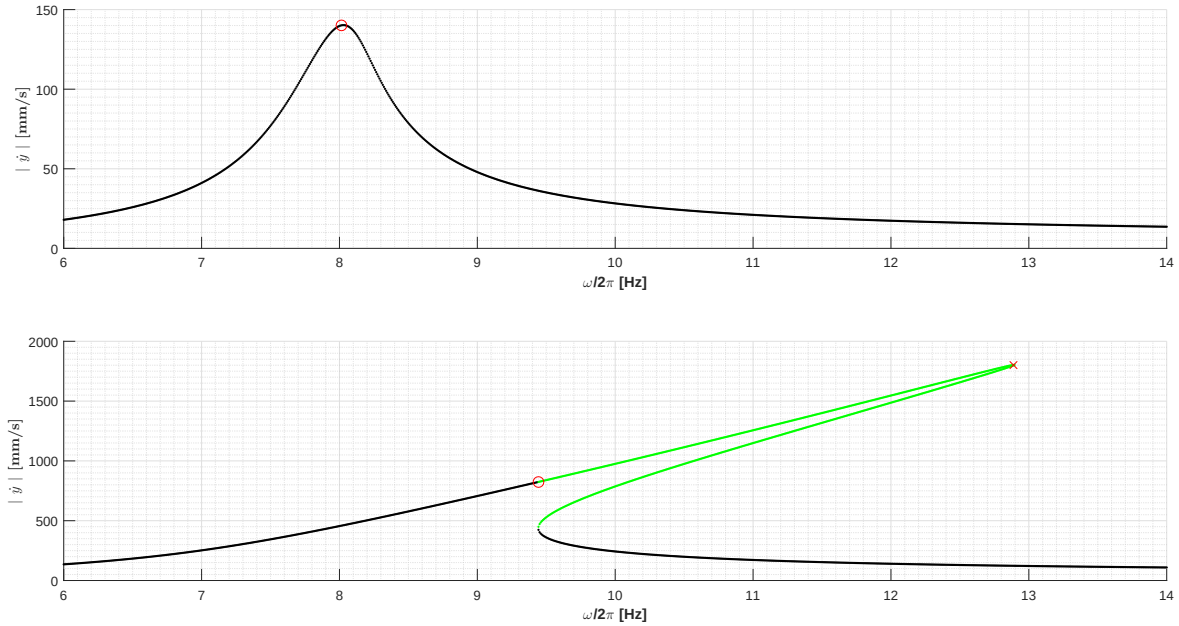

Figure 3.3: Relative velocity response for different excitation amplitudes: $F_1 = 0.5m/s^2$ (top) and $F_1 = 4m/s^2$ (bottom) with the damping ratio set to $\xi = 0.05$.

3.7 Parameterization

A harvester available in the Automation and Robotics Laboratory of the Department of Mechanical Engineering of University of Aveiro was parametrized according to the model proposed by Mann and Sims [14]. A simulation was performed in order to validate the impact of adjusting the physical structure of the magnetic levitation system. This section describes not only the architecture of the transducer but also the experimental measurements conducted to reach the magnetic force-displacement relationship and related constraints, electromechanical coupling coefficient and damping factor.

3.7.1 Harvester's architecture

The harvester's architecture (figure 3.4) is a combination of various arquitectures already proposed in the literature. There are similarities with the harvester proposed in [24, 25, 7] (because of its multi-coil-multi-magnet configuration), the harvester developed by [12, 13] (since it also contains cylindrical annuli magnets and a shaft), the model [1] (as the levitating magnets are disposed with opposite poles facing each other). It can also be stated that the harvester's architecture is similar to the transducer in [23], although with different configuration and number of magnets in the stack. The electromagnetic generator is composed by:

- acrylic tube for the inner structure: ⌀26x30 mm, 104 mm height
- fixed neodymium magnets: N42 magnetization, nickel-plated, 27x16x5 mm ring magnets
- stack: composed by 2 neodymium magnets with opposite poles facing each other, N38 magnetization, nickel, 25xM5x14 mm threaded pot magnets (each one has 7 mm height)
- coils: composed by 3 separated windings, AWG35 wire. Each winding has 20 mm height, $\varnothing_{int}$33 mm, $\varnothing_{ext}$47mm.

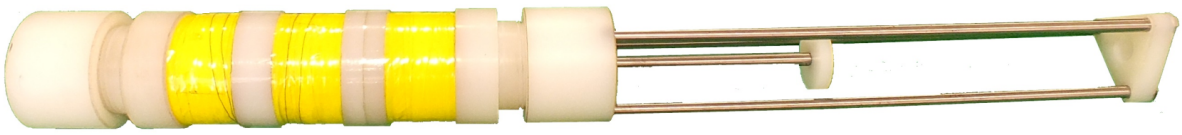

Figure 3.4: Electromagnetic harvester.

The structure that is assembled to the harvester (right side of figure 3.4) has the purpose of holding a sensor unit for the position monitoring of the levitating magnet over time.

3.7.2 Experimental apparatus

Sensor

A **microsonic® nano 15/CU** ultrasonic sensor was used to measure the levitating magnet position using the assembled external structure. This sensing device has a 20 mm to 350 mm measuring range, 0.069 mm resolution and a 0-10 linear voltage output.

Data acquisition

A control unit, using an **Arduino® NANO** board, is available to record the data acquired by the ultrasonic sensor. 1kHz data acquisition was performed to allow high resolution monitoring.

Data storage

The data from experimental tests were written and stored in .txt files using the ***CoolTerm*** software. This program reaches the selected serial port and prints the received information into a desired format file.

Controller board

The harvester output voltage and the levitating magnet position were monitored by a **DSP controller board** (DS1102 from dSPACE). I/O modules of DS1102 were initialized and configured in *Simulink* by the Real Time Workshop and Real Time Interface. An application was developed in ControlDesk to interact with the real-time application [4].

3.7.3 Repulsive magnetic forces

Several experimental tests were conducted to identify the force-displacement behavior between the levitating magnet and a fixed one. Magnets with different masses were vertically positioned in order to monitor magnetic repulsive forces. Each red dot describes the force between the magnets (on the bottom and the corresponding stack position). By repeating this process 15 times, it was possible to fit those measurements to a power series, as it can be seen in figure 3.5.

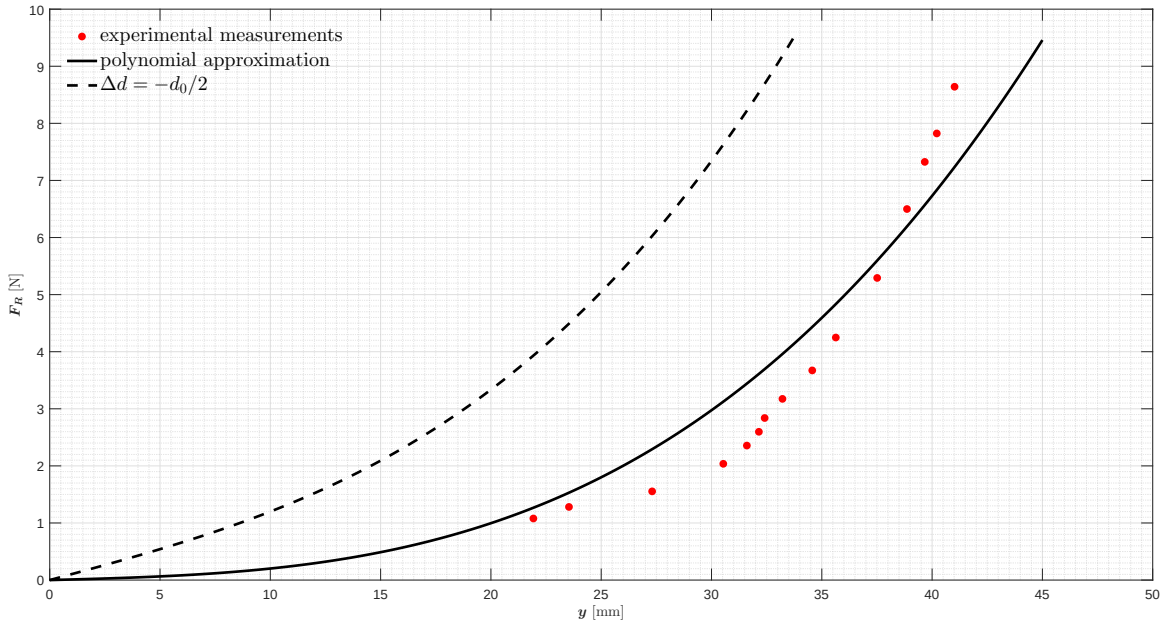

Figure 3.5: Experimental measurements of the restoring force and respective distance between magnets (red dots); curve fitting approximation to a cubic polynomial (solid black line); force-displacement relationship when $\Delta d = -d_0/2$ (dashed black line).

The repulsive forces of neodymium magnets cannot accurately be described with a polynomial approximation. Much better approximation require 1st order Bessel functions (see table 2.5) [4]. Nevertheless, no significant changes in the mechanical dynamics will occur if such polynomial approximation is considered.

The *fminsearch* tool, available in *MATLAB*, was used to find the k and $k3$ that more properly fitted the experimental measurements. The best approximation is also represented in the previous figure and matches $k = 10.3313$ [N/m] and $k_3 = 98694$ [N/m^3].

As previously mentioned, this generator has a higher than required length that would approach it to the one described in Mann and Sims' model. Therefore, length variation was considered until $-d_0/2$ (it can only be shortened).

3.7.4 Damping factor

The free-fall test was performed by dropping vertically the levitating magnet from 45 mm above the bottom fixed magnet in order to determine the damping factor. The magnet's position over time was stored in *CoolTerm* software. The walled cylindrical tube was removed in this measurement to provide zero electromechanical coupling.

The model with neither external excitation nor electric parameters was implemented in *Simulink* (v8.7, R2016a, *Mathworks*), as demonstrated in figure 3.6. The main goal was to simulate the overall mechanical dynamics (d_0 mm above the bottom magnet).

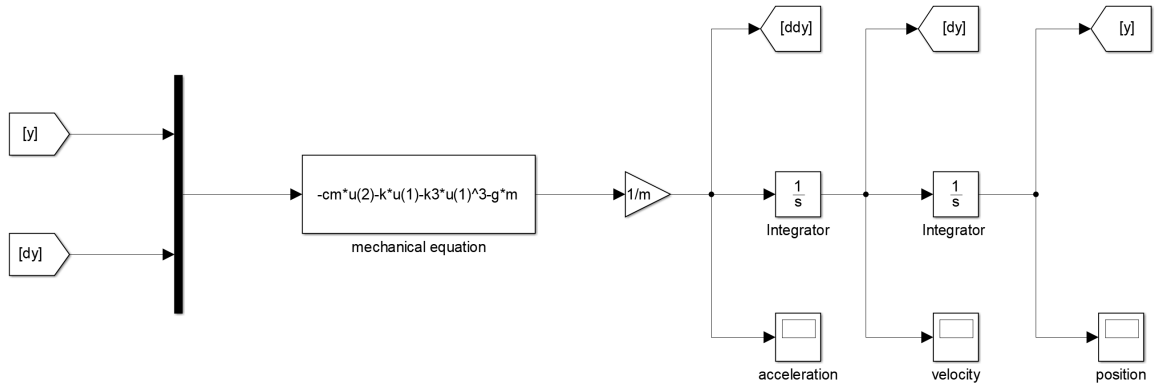

Figure 3.6: Block diagram implemented in *Simulink* to simulate the mechanical dynamics of the harvester.

The *fminsearch* tool was once again used, in addiction to the results obtained in *Simulink*, to find the best damping value obtained by the smallest error between the simulated and the experimentally tested curve. Figure 3.8 highlights the experimental free fall test and simulation results with $\xi = 0.9$.

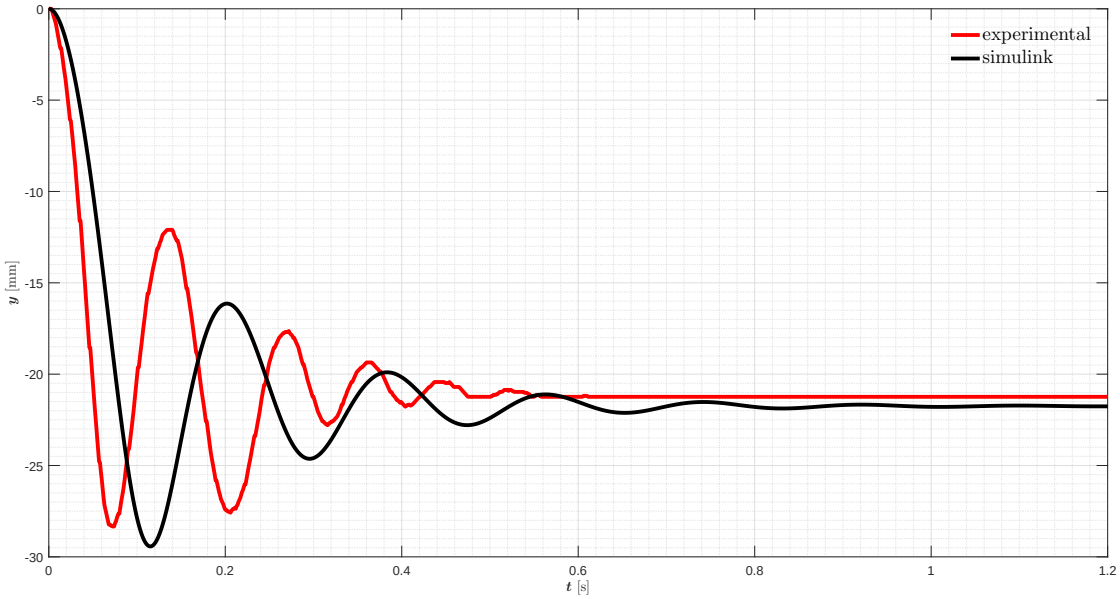

Figure 3.7: Stack fall test curves from 45 mm height obtained through: experimental measurements (red); best approximation with *Simulink* simulation results, ξ=0.9 (black).

3.7.5 Electromechanical coupling coefficient

A DSP board (DS1102 from DSPACE) was used to monitor both the levitating magnet position and harvested voltage in a experimental test. The main goal was to obtain an approximate electromechanical coupling coeficient. The stack's position was experimentally varied during 10 seconds.

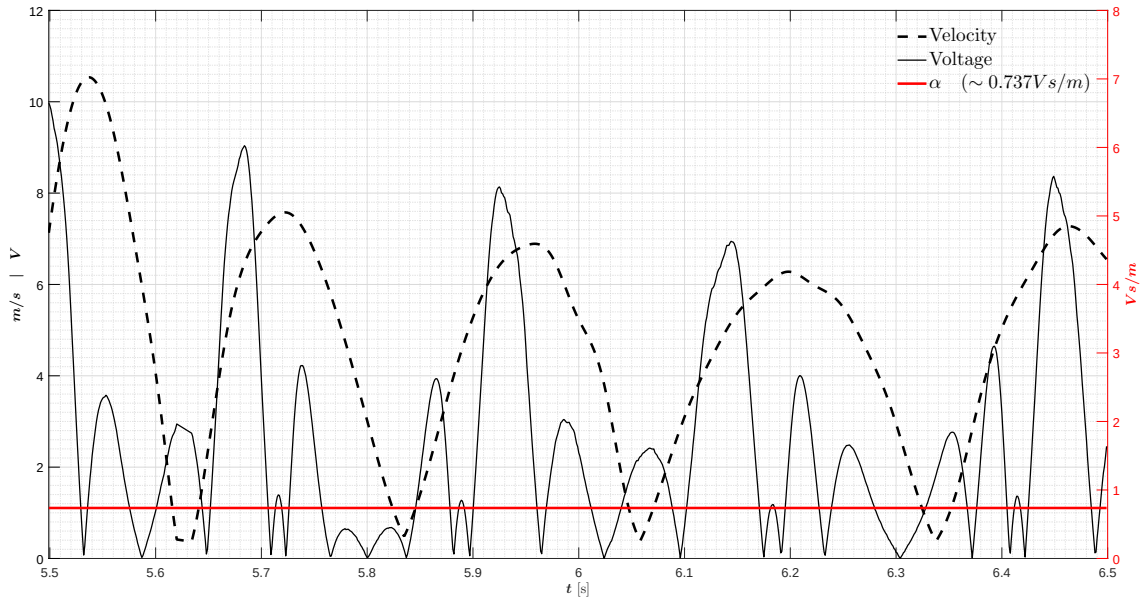

Figure 3.8: Stack's experimental velocity (dashed black line) and output voltage (solid black line); average electromechanical coupling coefficient (red line).

3.7.6 Parametric analysis of parameterized harvester

For the simulation with the parameterized electromagnetic harvester, the total length, the excitation and frequency were variable parameters. Table 3.3 shows parameters under analysis and range of analysis. The constant model parameters used for this simulation are listed in table 3.2.

Table 3.2: Constant parameters - parametrized harvester

Parameter	**Value**	**Units**
m	0.10354	kg
k ($\Delta d = 0$)	10.3313	N/m
$k3$ ($\Delta d = 0$)	98694	N/m^3
d_0	45	mm
g	9.81	m/s^2
α	0.737	Vs/m
ξ	0.9	-
R_{int}	2200	Ω
R_{load}	1	MΩ

Table 3.3: Variable parameters - parametrized harvester

Parameter	**Range**	**Units**
$\Omega/2\pi$	[0,300] 6000 generated values	Hz
F_1	$[0.1, 8.4]$ 84 generated values	m/s^2
Δd	$[-d_0/2, 0]$ 200 generated values	mm

Chapter 4

Results

This chapter is divided in two subchapters: the first one focused on results related to the approach to the harvester developed by Mann and Sims [14] and the second concerns the parametrized harverster. The addressed issues in each configuration are the relative velocity of the central magnet, the current intensitiy and the power dissipated on the resistive load.

4.1 Mann and Sims' model

The first analysis regards the total length of the harvester. Two-dimensional curves in the hysteresis zone are shown. A detailed analysis concerning the relative velocity's response to the frequency and length of the generator, is presented in a three-dimensional illustration in figure 4.7.

Figure 4.1 describes the harvester's response to five length variations, with Δd between -$d_0/2$ and 0 mm: the larger the generator's length, the higher the velocity, with increasingly smaller frequencies needed to achieve such velocities. Although power behaves slightly different (given its value of current square), current and power behave similarly to velocity, as figures 4.2 and 4.3 illustrate. For Δd=-$d_0/2$ mm, the system acquires a 14 Hz resonance frequency and a 465 mm/s velocity. For Δd=0 mm, velocity reaches 830 mm/s when oscillating with a 9.5 Hz resonance frequency. It can be concluded that a 78% increment in the velocity and a 32% decrease in frequency are detected when Δd is increased from -$d_0/2$ to 0 mm. Current and power's frequency variation is analogous to the velocity's, to same Δd variations. From Δd=-$d_0/2$ to Δd=0 mm, current intensity rises from 1.9×10^{-8} to 9×10^{-8} A, which translates in a 370% increment. Power, on the other hand, evolves from 3.6×10^{-10} to 8.1×10^{-9} W, corresponding to a 22.5 gain.

The relative velocity's pattern to five variations of the generator's length is described in Figure 4.4, for $0< \Delta d < d_0/4$ mm. In this range, the larger the length, the higher the velocity, mainly if the excitation frequency rises significantly, as exhibited in figures 4.5 and 4.6. When Δd changes from 0 to $d_0/4$ mm, resonance frequency rises from 9.5 to 64 Hz and velocity grows from 830 to 6250 mm/s, which translates in 7.5 gain. When current is concerned, an evolvement from 9×10^{-8} to 7.5×10^{-7} A can be seen, bearing a 733% increase. Power grows from 8.1×10^{-9} to 5.7×10^{-7} W, defining an 70.4 power gain.

In the three-dimensional graphic (figure 4.7), when Δd rises from -$d_0/2$ to 0 mm, a small decrease in the resonance frequency is observed, along with a slight increase in the velocity. For Δd variations from 0 to $d_0/4$ mm, a sudden growth in frequency and velocity is noticed.

The velocity peaks seen as from 1000 mm/s are due to the assumption made in section 3.5 (hysteresis zone is not considered). An abrupt velocity variation zone is highlighted in this figure. This is the consequence of the used Δd resolution. In fact, lower resolutions would have resulted in lower peak-to-peak values. The 93 μm resolution (adopted in the Δd >0 mm interval) arises as insufficient to eliminate these variations.

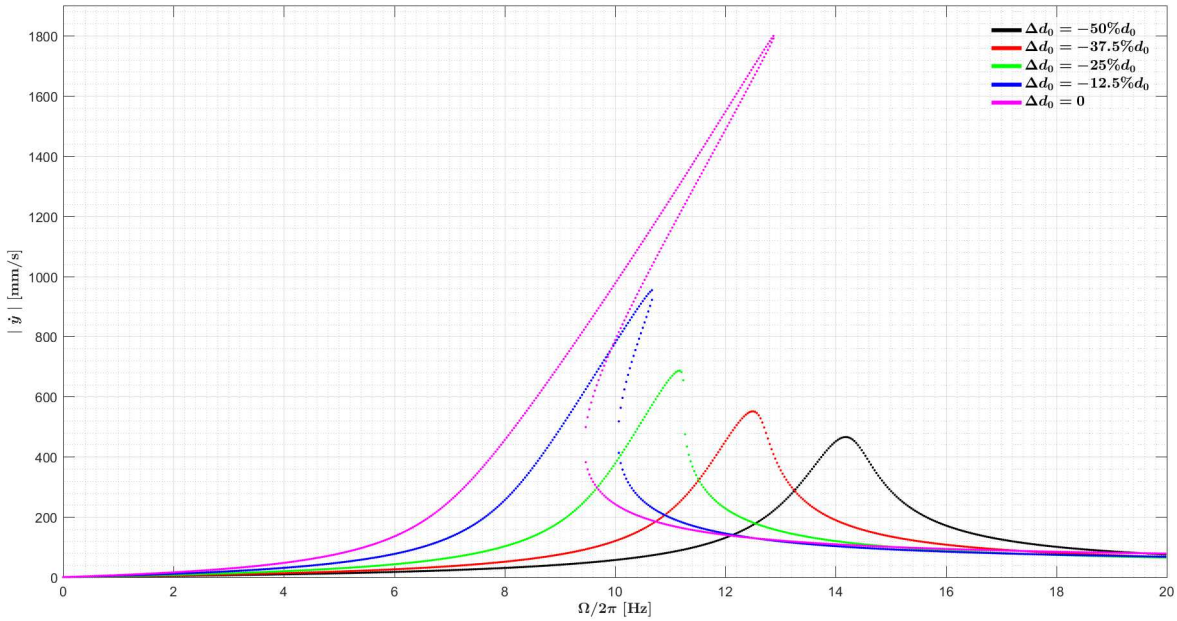

Figure 4.1: Relative velocity response for different Δd lengths ($-d_0/2 < \Delta d < 0$). The F_1 was set to 4 m/s^2 and ξ was set to 0.05. Parameters from table 3.1 were used.

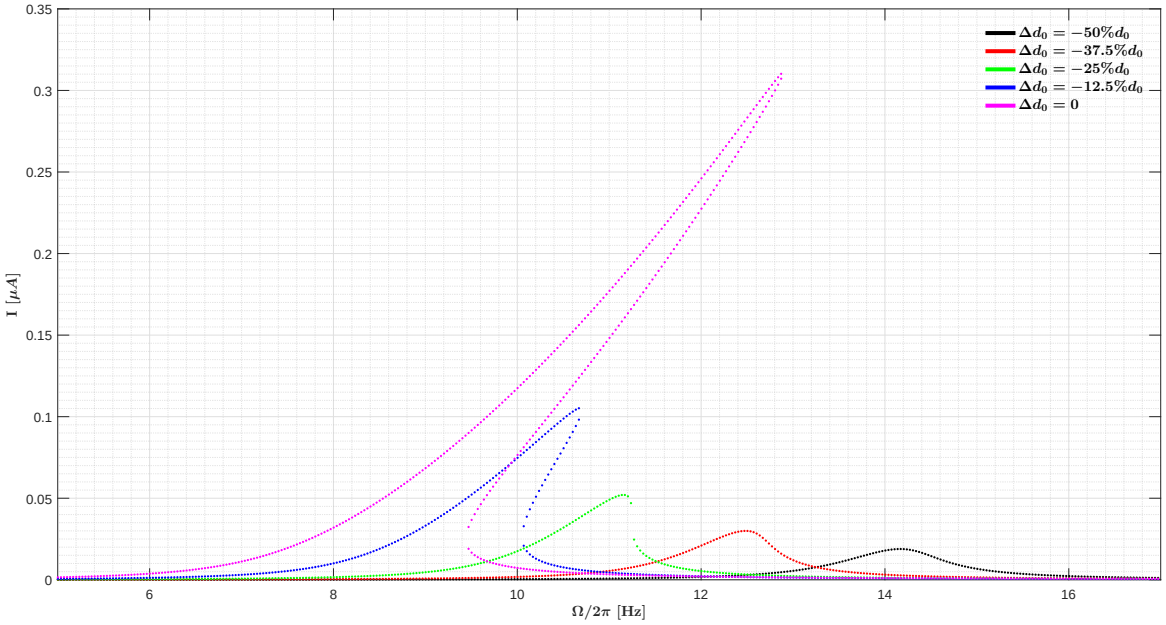

Figure 4.2: Electric current for different Δd lengths ($-d_0/2 < \Delta d < 0$). The F_1 was set to 4 m/s^2 and ξ was set to 0.05. Parameters from table 3.1 were used.

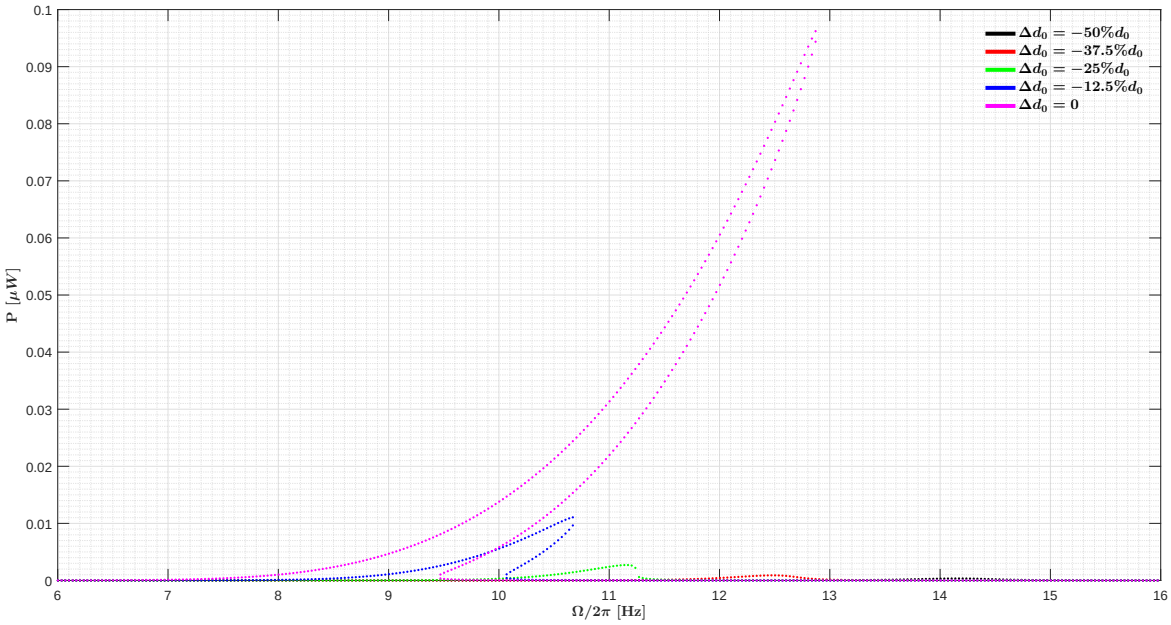

Figure 4.3: Electric power for different Δd lengths ($-d_0/2 < \Delta d < 0$). The F_1 was set to 4 m/s^2 and ξ was set to 0.05. Parameters from table 3.1 were used.

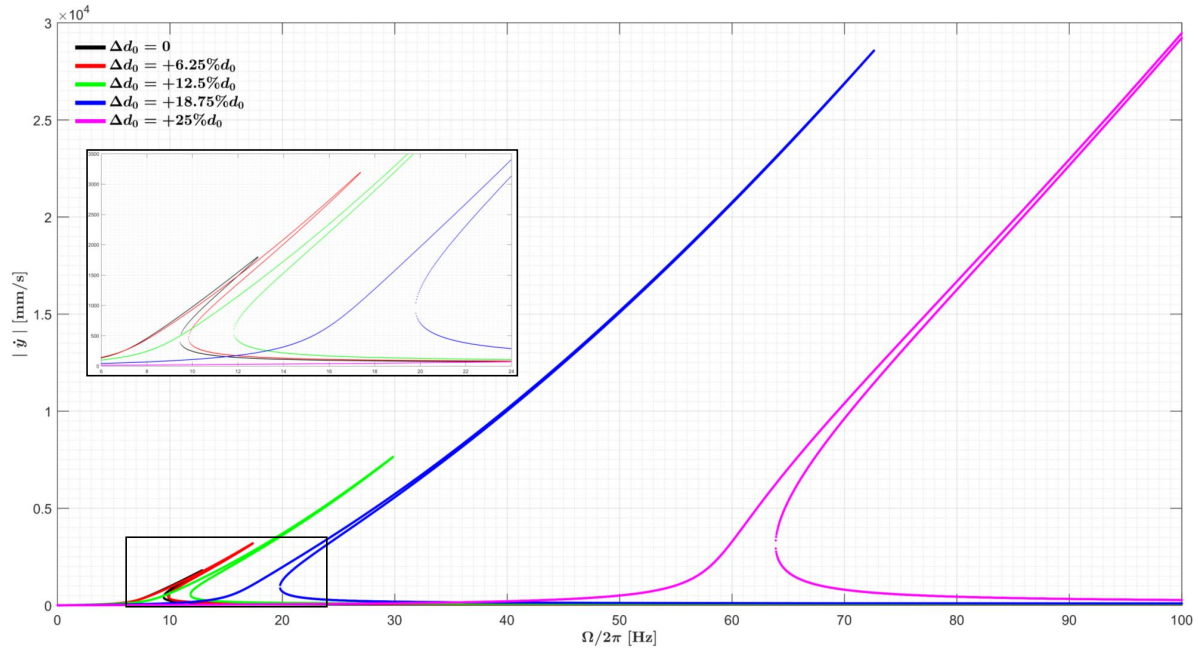

Figure 4.4: Relative velocity response for different Δd lengths ($0 < \Delta d < d_0/2$). The F_1 was set to 4 m/s^2 and ξ was set to 0.05. Parameters from table 3.1 were used.

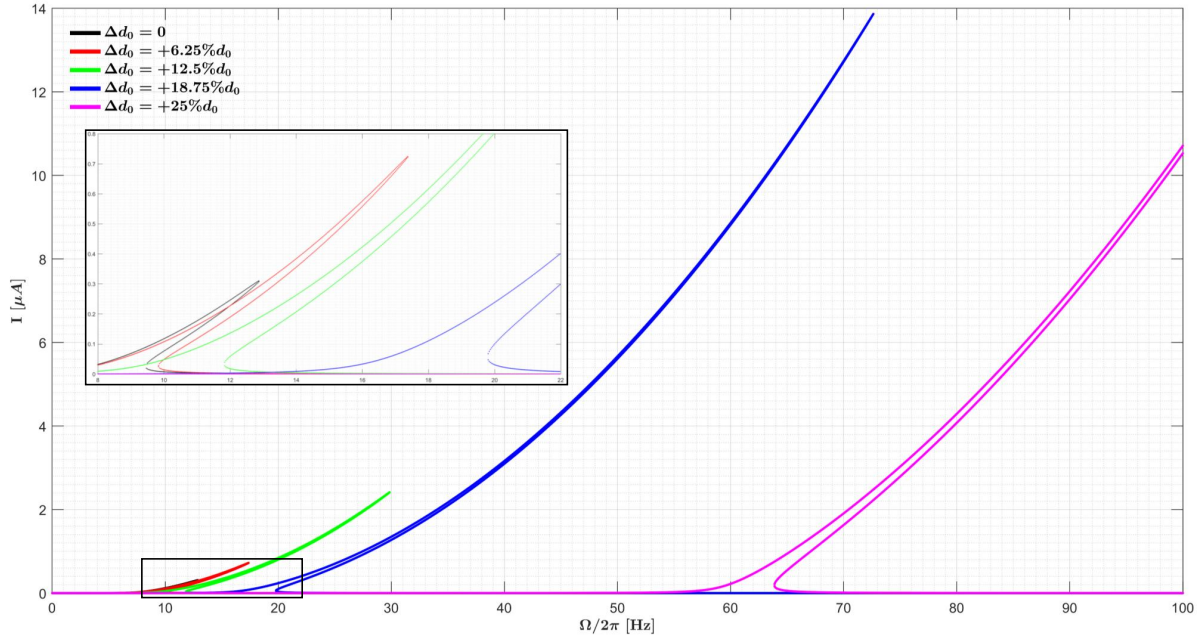

Figure 4.5: Electric current for different Δd lengths ($0 < \Delta d < d_0/2$). The F_1 was set to 4 m/s^2 and ξ was set to 0.05. Parameters from table 3.1 were used.

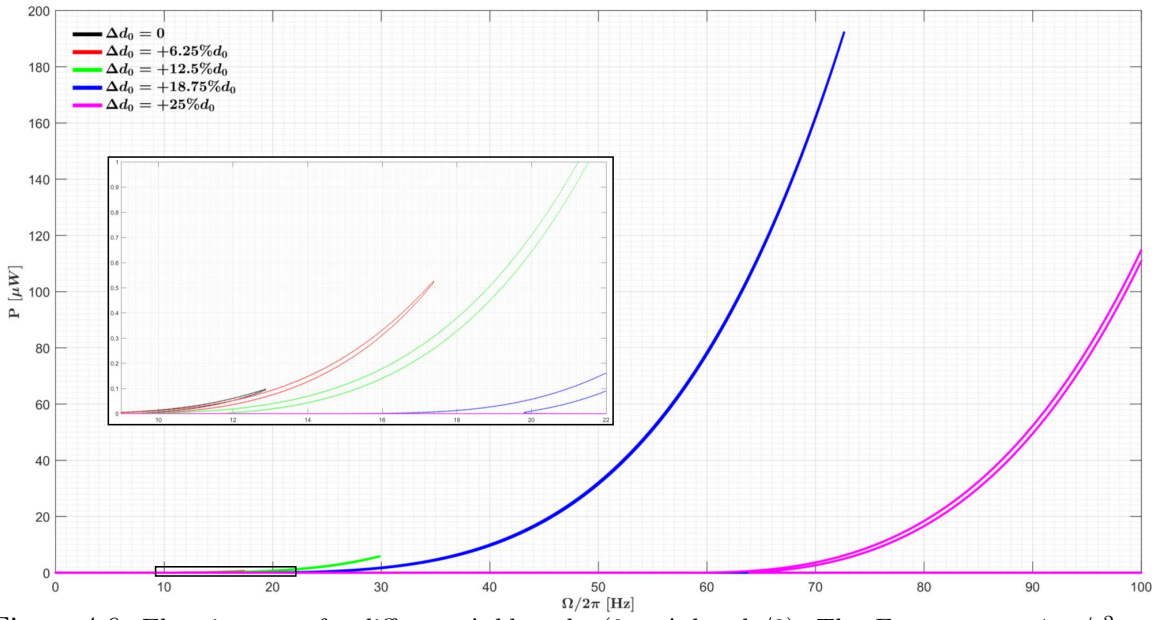

Figure 4.6: Electric power for different Δd lengths ($0 < \Delta d < d_0/2$). The F_1 was set to 4 m/s^2 and ξ was set to 0.05. Parameters from table 3.1 were used.

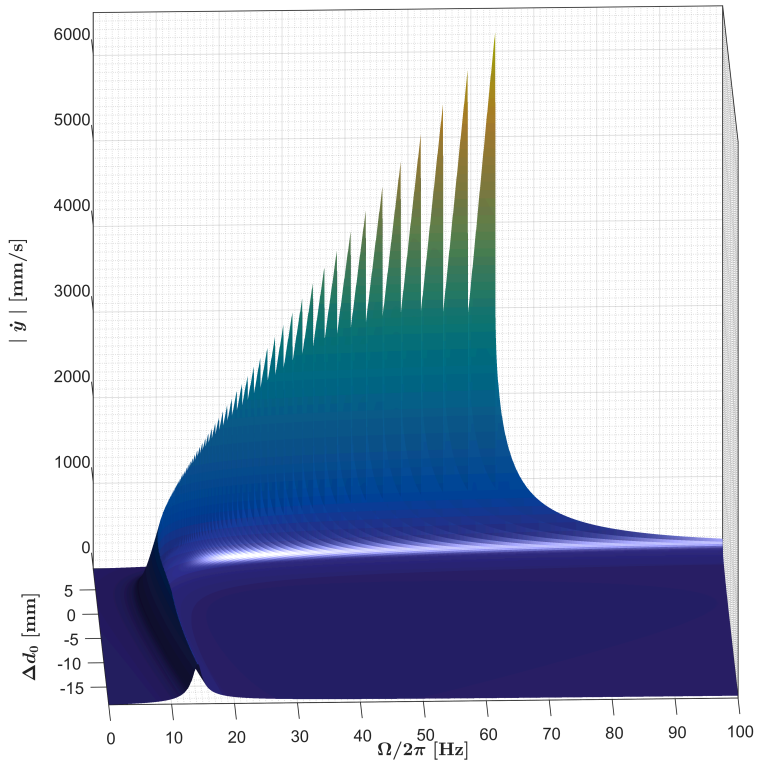

Figure 4.7: Relative velocity response for every Δd lengths and frequency. The excitation amplitude (F_1) was set to 4 m/s^2 and damping ratio (ξ) was set to 0.05. Parameters from table 3.1 were used.

The maximum velocity, current and power that are reachable for each frequency and Δd are also significant in the design of energy harvesters and control of their performance. Firstly, the study is conducted using five excitations with constant damping.

Figures 4.8 and 4.9 describe a relevant phenomena: when the structure shortens ($-d_0/2 < \Delta d < 0$ mm), no significant differences are observed in the maximum velocity and only slightly changes are noticed as Δd approaches $-d_0/2$ mm. Minimal Δd from which the velocity shown in figure 4.8 starts to decay is different between excitations. For example, Δd corresponding to 8 m/s^2 is -15 mm; for 6m/s^2, a -11 mm Δd is verified; for 4 m/s^2, a -7 mm Δd is observed; for an excitation of 2 m/s^2, Δd from which a velocity decay is observed is 0 mm. Nevertheless, significant increases in magnet velocity will occur as $\Delta d > 5$ mm. A similar analysis can be made for current, as seen in figure 4.10. Significant increases in power arise when $\Delta d > 5$ mm, as described in figure 4.11.

Figure 4.12 labels the frequency associated to figures 4.8, 4.10 and 4.11. These velocity, current and power gains come with frequency changes. As Δd is moved away from $-d_0/2$ mm, a frequency decrease is predicted. In contrast, significant frequency increases are expected as Δd approaches $d_0/2$ mm. To $-10 < \Delta d < 7$ mm harvester's length values, the resonance frequency variation appears to be greater between 0.1 e 8 m/s^2 (to same Δd). The greater the excitation, the greater the associated resonance frequency (to same Δd). The lowest frequencies (to which the velocities are maximum) occur for lengths between $-5 < \Delta d < 5$ mm. The overall dynamics considering the effects of Δd, excitations and frequency are illustrated in figure 4.13.

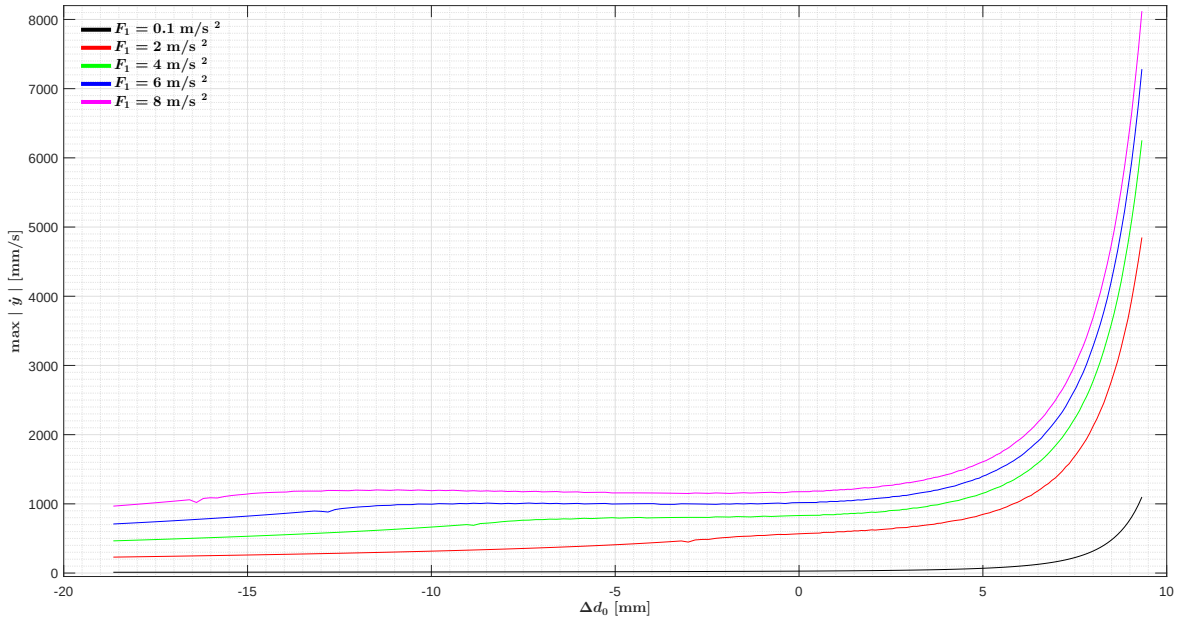

Figure 4.8: Maximum relative velocity response in function of Δd for different excitation amplitudes. The ξ was set to 0.05. Parameters from table 3.1 were used.

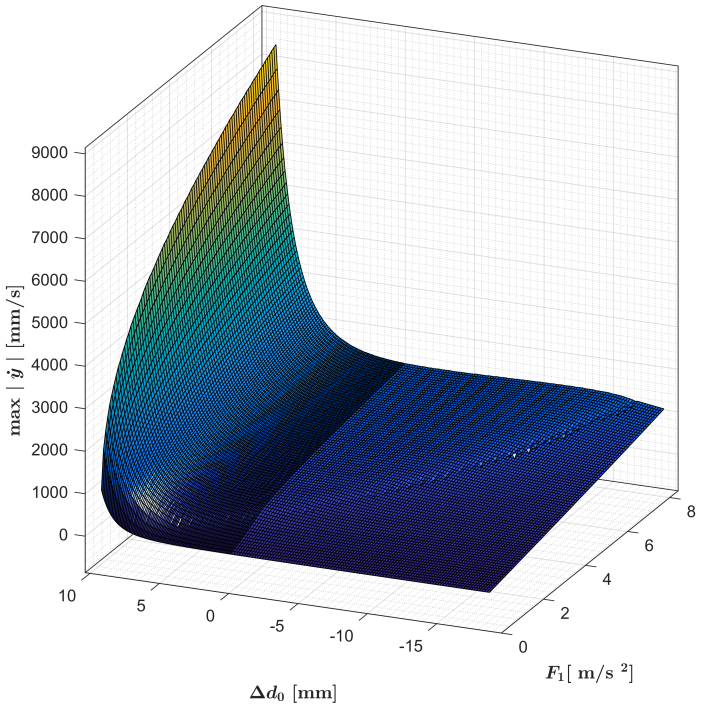

Figure 4.9: Maximum relative velocity response for every Δd and excitation amplitudes. The ξ was set to 0.05. Parameters from table 3.1 were used.

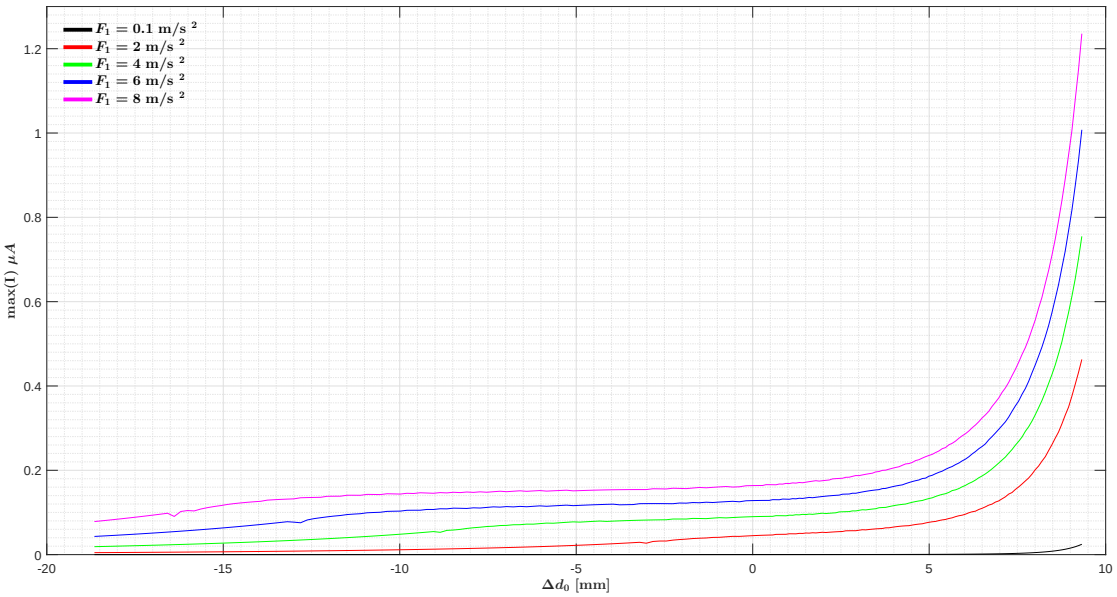

Figure 4.10: Maximum electric current in function of Δd for different excitation amplitudes. The ξ was set to 0.05. Parameters from table 3.1 were used.

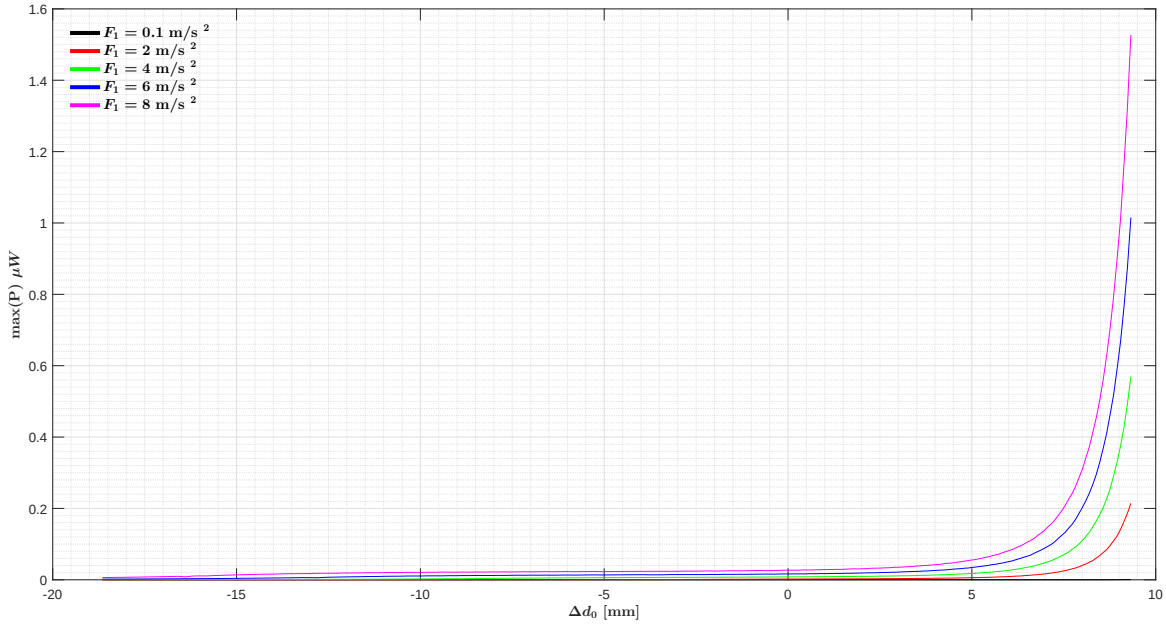

Figure 4.11: Maximum electric power in function of Δd for different excitation amplitudes. The ξ was set to 0.05. Parameters from table 3.1 were used.

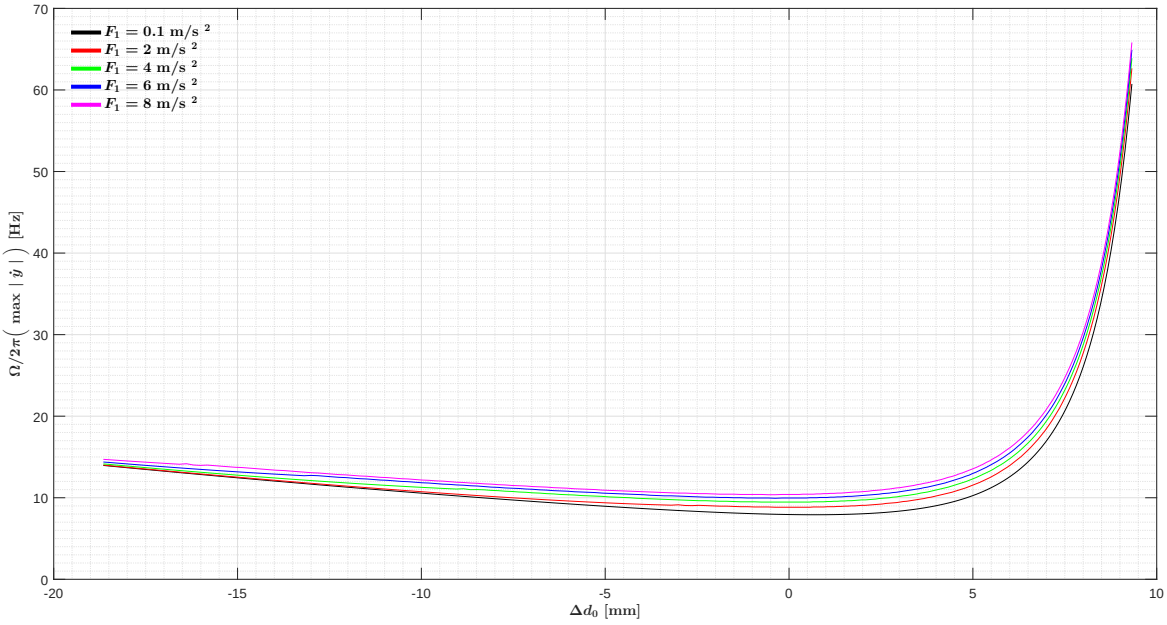

Figure 4.12: Matching frequency to maximum relative system response in function of Δd for different excitation amplitudes. The ξ was set to 0.05. Parameters from table 3.1 were used.

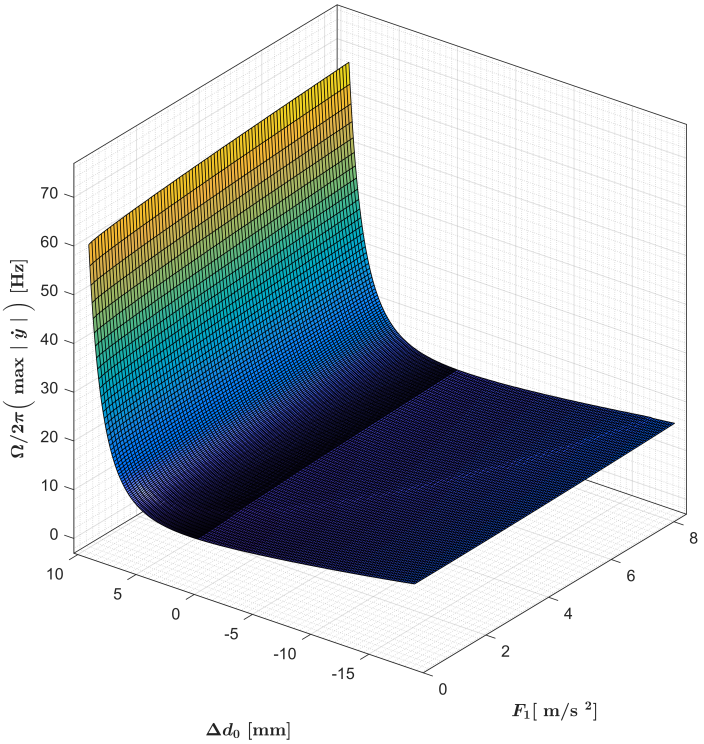

Figure 4.13: Matching frequency to maximum relative system response for every Δd and excitation amplitudes. The ξ was set to 0.05. Parameters from table 3.1 were used.

Figure 4.14 is an overlap of figure 4.8 and figure 4.12. It presents the maximum velocity in function of resonant frequency for every Δd. Figure 4.15 and 4.16 are the analogy for current (combining figure 4.10 with figure 4.12) and power (combining figure 4.11 with figure 4.12), respectively.

For growing variations of -$d_0/2 < \Delta d <$0 mm, maximum velocities tend to increase and are followed by the resonance frequencies' decrease. When Δd grows between 0$< \Delta d < d_0/4$ mm a large increase is seen in both velocity and frequency. This means that for any excitation, the maximum velocity/ current / power with the smaller resonant frequency are obtained with Δd=0 mm. When Δd=-$d_0/2$ mm, for an 0.1 m/s^2 excitation, the maximum velocity of 11.5 mm/s is reached at 14 Hz, while for an 8m/s^2 excitation, a 14.7 Hz frequency is needed to achieve maximum velocity (970 mm/s). Hence, there is a 5% increase in frequency and a 8335% increase in velocity. If Δd=$d_0/4$ mm, differences are much greater: for 0.1 m/s^2 excitations, a 60.7 Hz resonance frequency is observed, corresponding to a 1100 mm/s velocity; for 8 m/s^2 excitations, a 65.8 Hz resonance frequency is observed, which corresponds to a 8120 mm/s velocity. Therefore, from 0.1 to 8 m/s^2, gains of 8.4% in frequency and 638% in velocity are obtained. For lengths equivalent to $\Delta d >$0 mm, the rate of increase in velocity and current is greater for greater excitations.

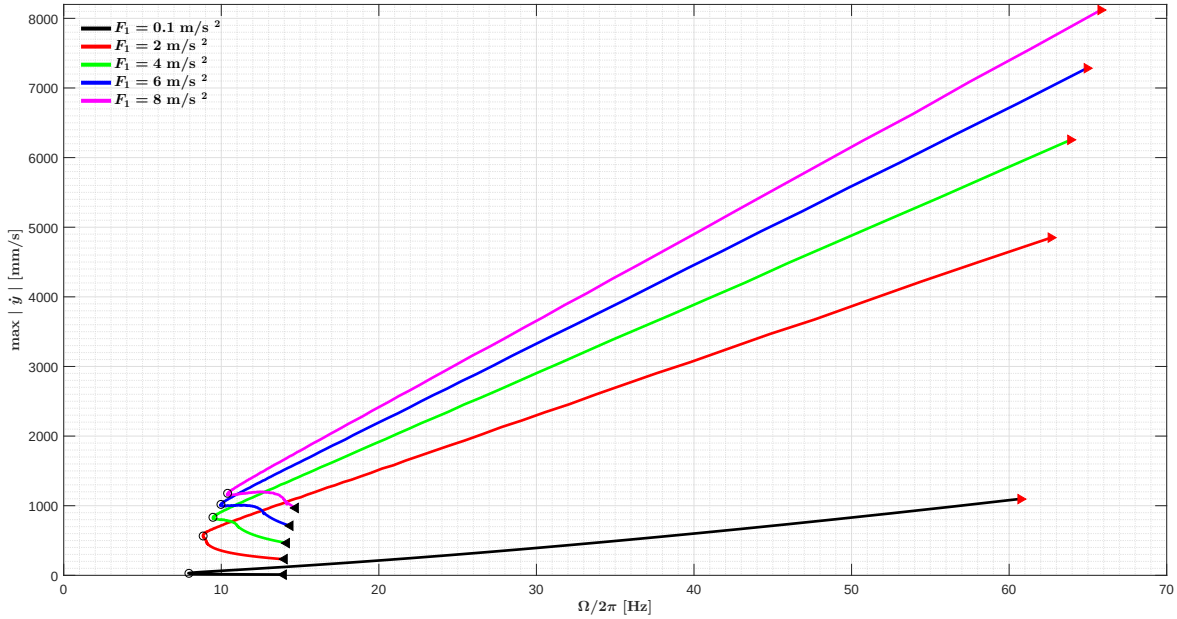

Figure 4.14: Maximum relative velocity response and combined frequency. Each trajectory describes the dynamics while varying Δd from -$d_0/2$ to $d_0/4$ (from black to red triangle; Δd=0 is identified by a black circle dot). The ξ was set to 0.05. Parameters from table 3.1 were used.

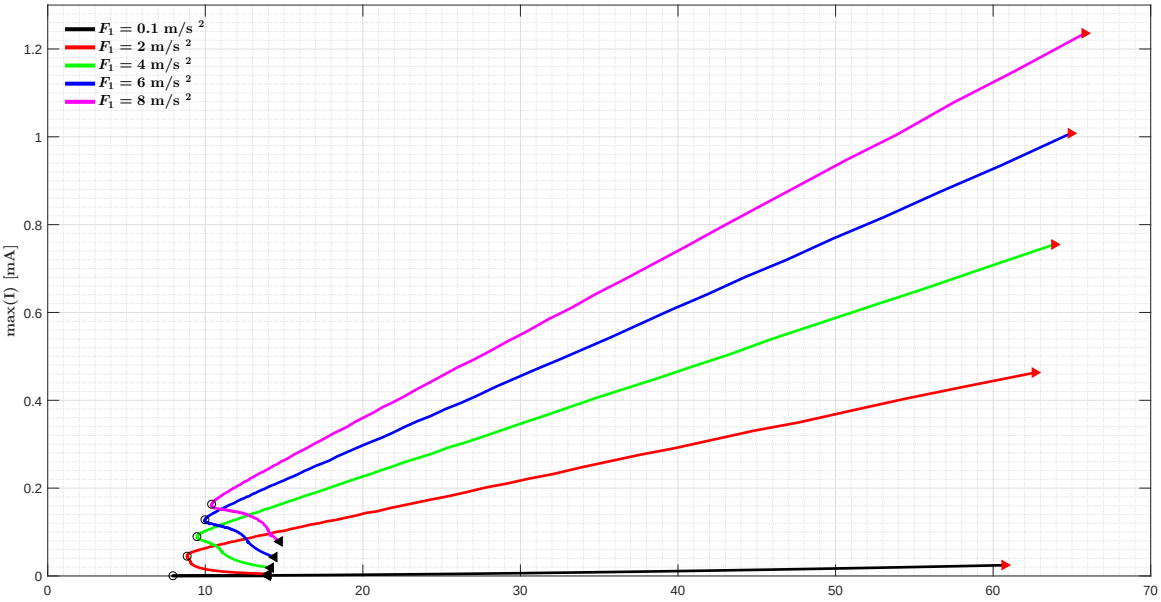

Figure 4.15: Maximum electric current and combined frequency. Each trajectory describes the dynamics while varying Δd from -$d_0/2$ to $d_0/4$ (from black to red triangle; Δd=0 is identified by a black circle dot). The ξ was set to 0.05. Parameters from table 3.1 were used.

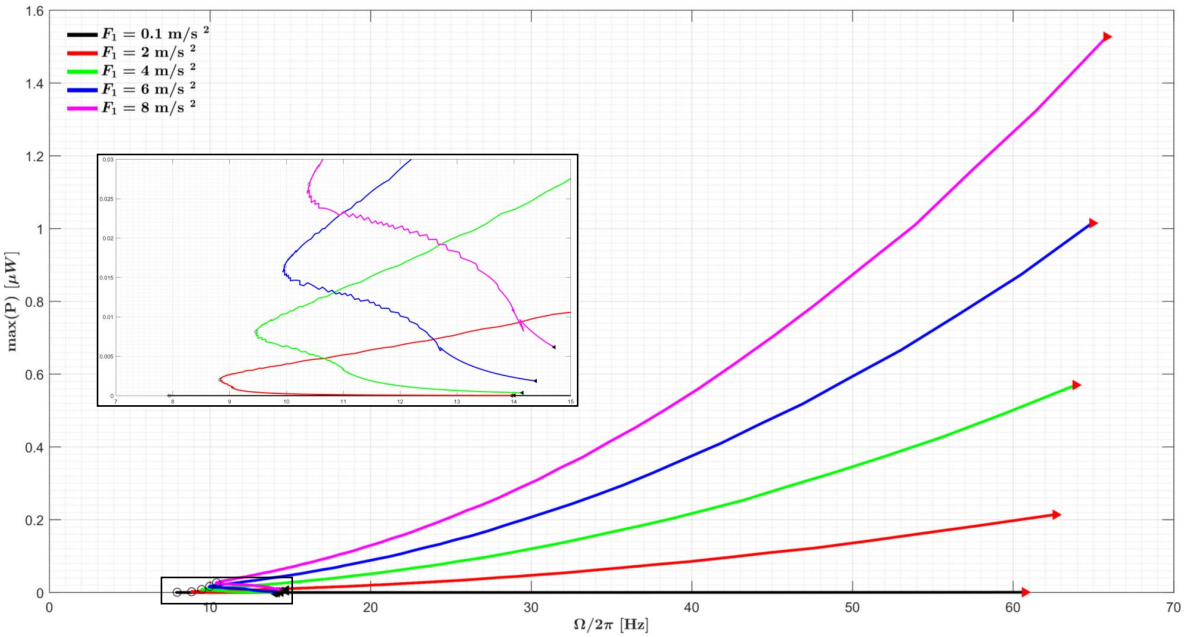

Figure 4.16: Maximum electric power and combined frequency. Each trajectory describes the dynamics while varying Δd from -$d_0/2$ to $d_0/4$ (from black to red triangle; Δd=0 is identified by a black circle dot). The ξ was set to 0.05. Parameters from table 3.1 were used.

A similar dynamics is observed for constant excitations and variable dampings. Maximum velocity, current and power to any frequency, in function of the harvester's Δd is shown in figure 4.17, 4.18 and 4.19, respectively.

In general, as damping increases, decreases in velocity, current and power are expected. When the harvester's length has a Δd=0 mm, maximum velocity in the most favourable scenario (ξ=0.05) is 830 mm/s, while in the least favourable scenario (ξ=0.4) maximum velocity is 140 mm/s. Thus, damping changes from 0.4 to 0.05 translates in a 493% increase in velocity. Significant increments in power begin when Δd >5 mm. The greater velocity discrepancies to the different damping factors happen when Δd=d0/4 mm.

The frequency where maximum velocity/ current / power occurs according to Δd development is represented in figure 4.20. Resonance frequency variation between different excitations is greater for -5< Δd <5 mm length variations.

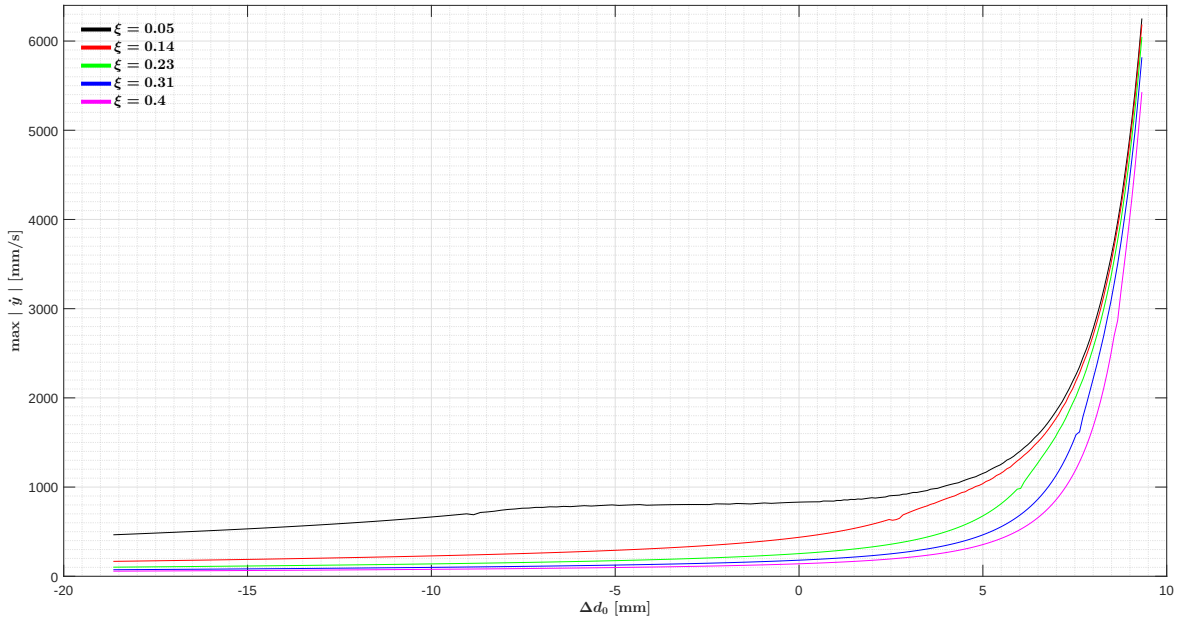

Figure 4.17: Maximum relative velocity response in function of Δd for different damping ratio. The F_1 was set to 4 m/s^2. Parameters from table 3.1 were used.

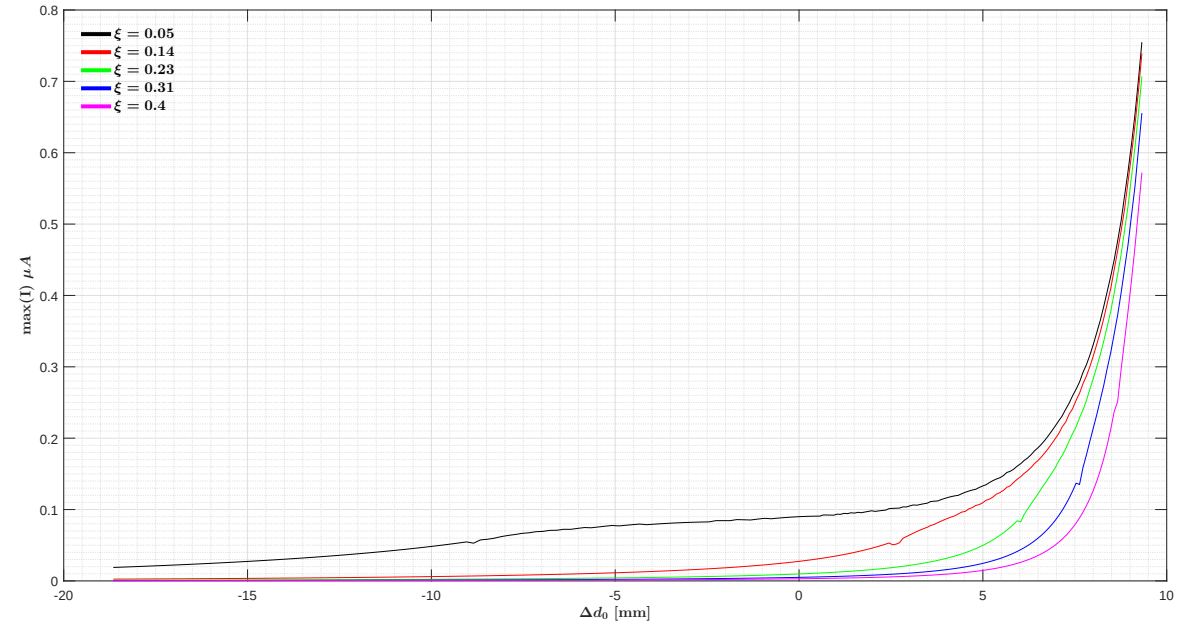

Figure 4.18: Maximum electric current in function of Δd for different damping ratio. The F_1 was set to 4 m/s^2. Parameters from table 3.1 were used.

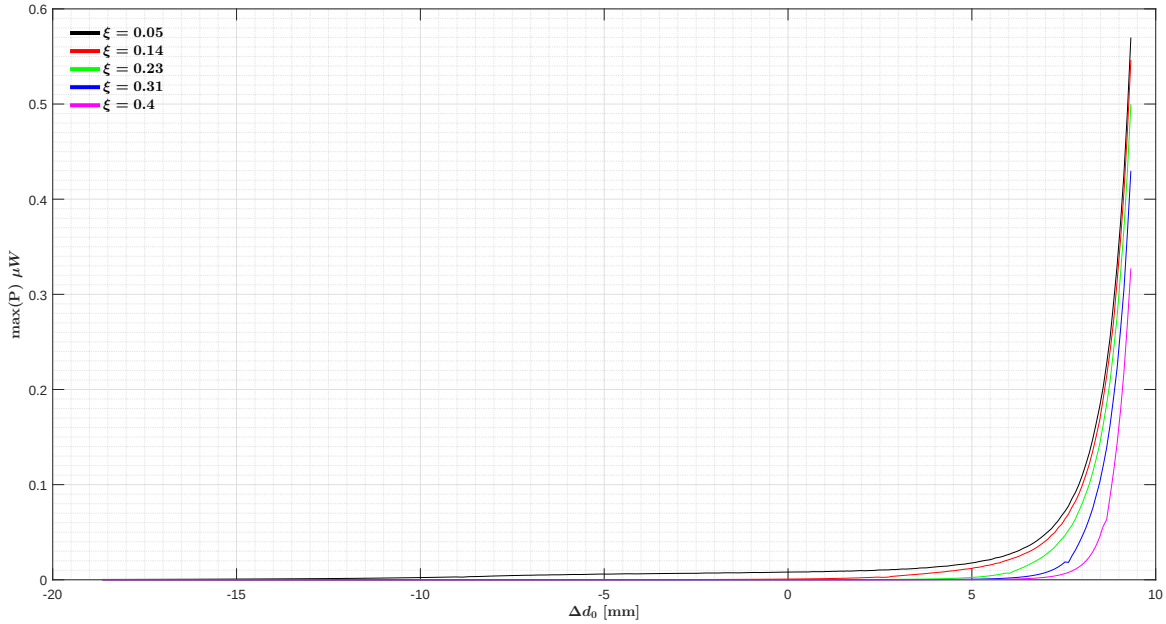

Figure 4.19: Maximum electric power in function of Δd for different damping ratio. The F_1 was set to 4 m/s^2. Parameters from table 3.1 were used.

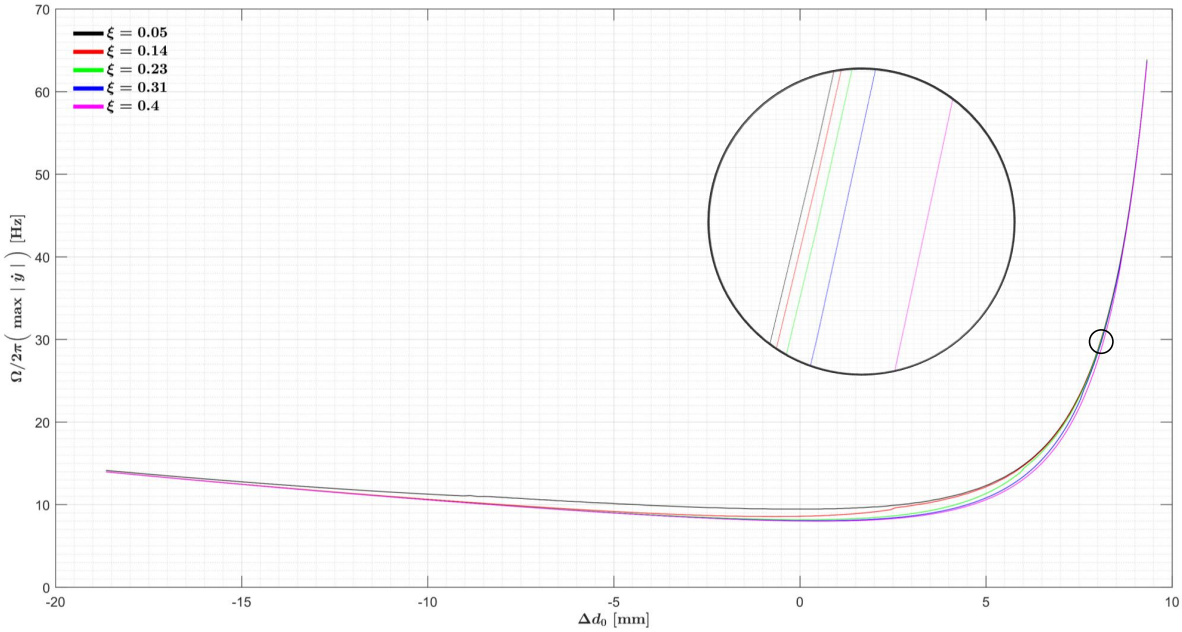

Figure 4.20: Matching frequency to maximum relative system response in function of Δd for different damping ratio. The F_1 was set to 4 m/s^2. Parameters from table 3.1 were used.

It is valid to make an association as seen in figure 4.14, 4.15 and 4.16, but specific to the variations in the damping factor (figure 4.21, 4.22 and 4.23).

The behaviour of the system for higher damping factors translates in lower frequencies and responses to any Δd. Similar behaviours are found for Δd >0 mm (the slope for any damping value remains the same).

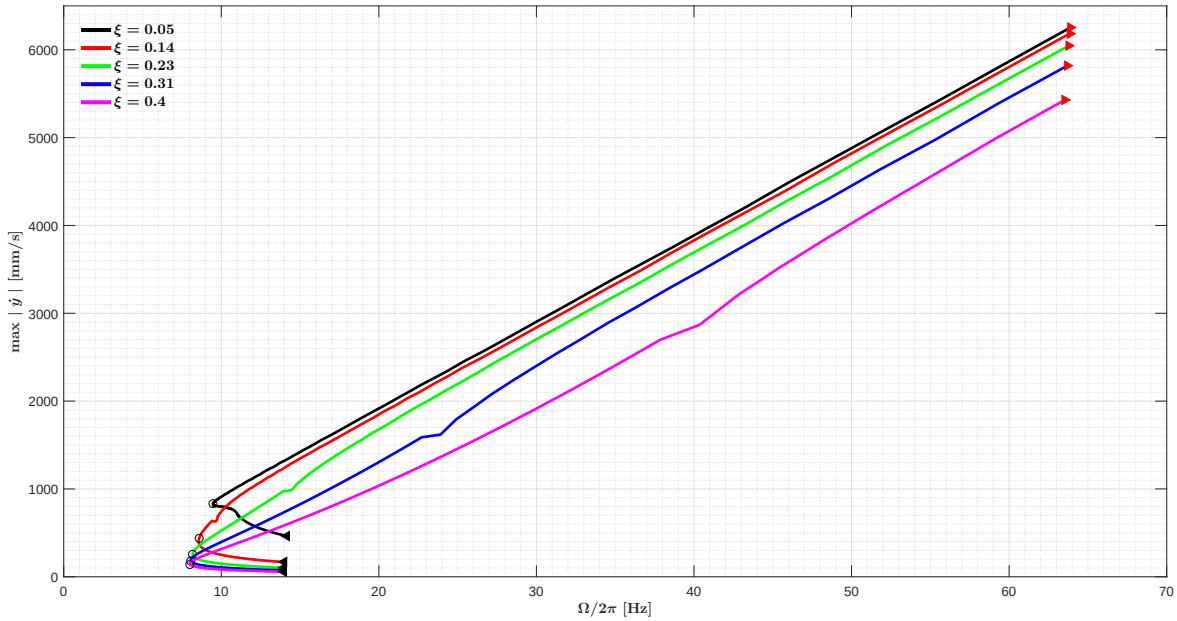

Figure 4.21: Maximum relative velocity response and combined frequency. Each trajectory describes the dynamics while varying Δd from -$d_0/2$ to $d_0/4$ (from black to red triangle; Δd=0 is identified by a black circle dot). The F_1 was set to 4 m/s^2. Parameters from table 3.1 were used.

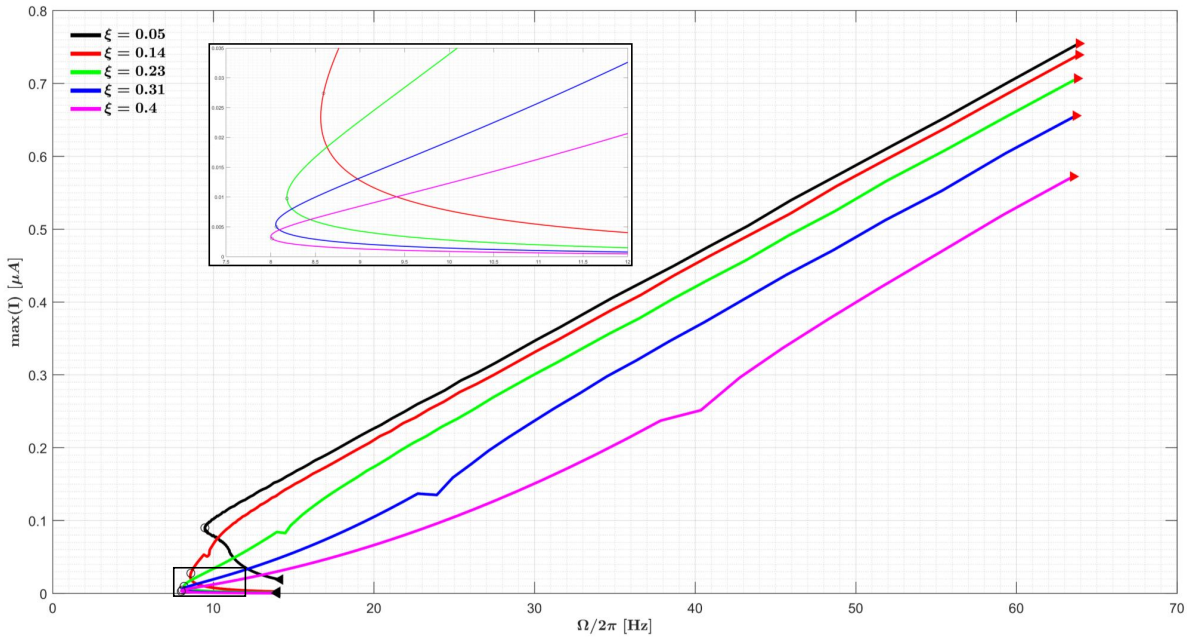

Figure 4.22: Maximum electric current and combined frequency. Each trajectory describes the dynamics while varying Δd from -$d_0/2$ to $d_0/4$ (from black to red triangle; Δd=0 is identified by a black circle dot). The F_1 was set to 4 m/s^2. Parameters from table 3.1 were used.

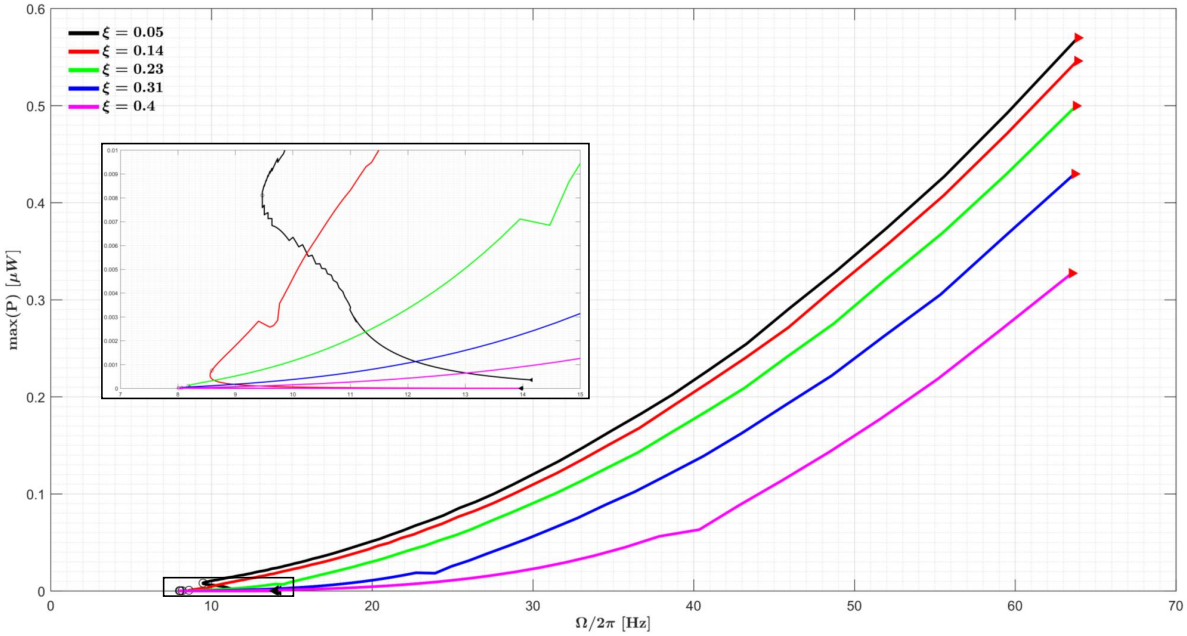

Figure 4.23: Maximum electric power and combined frequency. Each trajectory describes the dynamics while varying Δd from -$d_0/2$ to $d_0/4$ (from black to red triangle; Δd=0 is identified by a black circle dot). The F_1 was set to 4 m/s^2. Parameters from table 3.1 were used.

The adjustment of the harvester's length when facing excitation variations is demonstrated in figures 4.24, 4.26 and 4.27, in what maximum velocity, current intensity and power in function of frequency is concerned, respectively. Figure 4.25 highlights the overall dynamics taking the effects of frequency and excitation on maximum velocity into account (considering the best Δd).

In order to draw a curve from figure 4.24, it is first necessary to determine the system's response to each Δd (200 velocity dynamics in function of frequency) to a specific exterior excitation. The curve is defined by the (200) maximum solutions obtained in the previous step, for each frequency.

Once again, the multiple abrupt velocity variation zones are emphasized. The Δd >0 mm resolution of 93 μm is unsatisfactory. In fact, lower resolutions would have resulted in lower peak-to-peak values.

With adaptative control, with 0.1, 2, 4, 6 and 8 m/s^2, there are velocity gains of 11.2, 6.1, 3.6, 2.2, 1 and 86, 36.9, 23, 17.6, 15.3 to frequencies of 10 and 20 Hz, respectively (when compared to a harvester that lacks adaptive control). Heavy velocity gains of 196.1, 88.8, 60.5, 79.4, 61.9 apply for a frequency of 60 Hz, when the same described excitations are concerned.

Regarding current, for excitations of 0.1, 4 and 8 m/s^2, gains of 128.5, 13.3, 1 (for a 10 Hz frequency), 7.8×10^3, 523.8, 233.8 (for a 20 Hz frequency) and 3.5×10^4, 3.6×10^3, 3.8×10^3 (for a 60Hz frequency) are obtained, respectively.

When power is concerned, for excitations of 0.1, 4 and 8 m/s^2, gains of 1.6×10^4, 176.7, 1 (for a 10 Hz frequency), 6.1×10^7, 2.8×10^5, 5.4×10^4 (for a 20 Hz frequency) and 1.3×10^9, 1.3×10^7, 1.4×10^7 (for a 60 Hz frequency) are acquired, respectively.

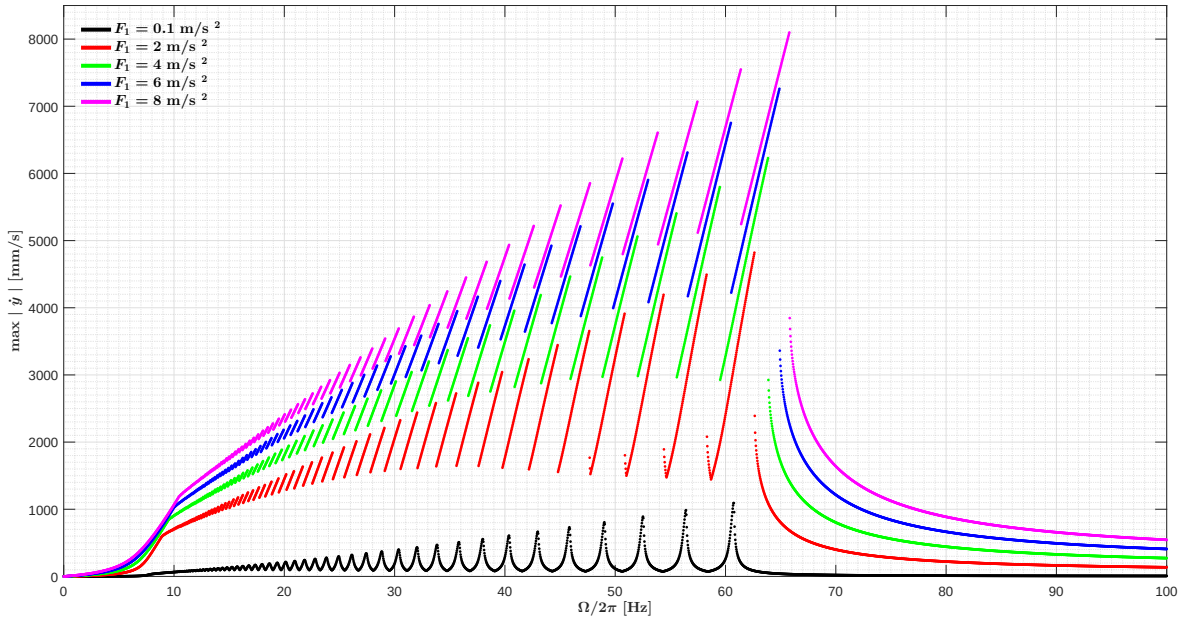

Figure 4.24: Maximum relative velocity response (considering the best values of Δd) according to the external frequency for different excitation amplitudes. The ξ was set to 0.05. Parameters from table 3.1 were used.

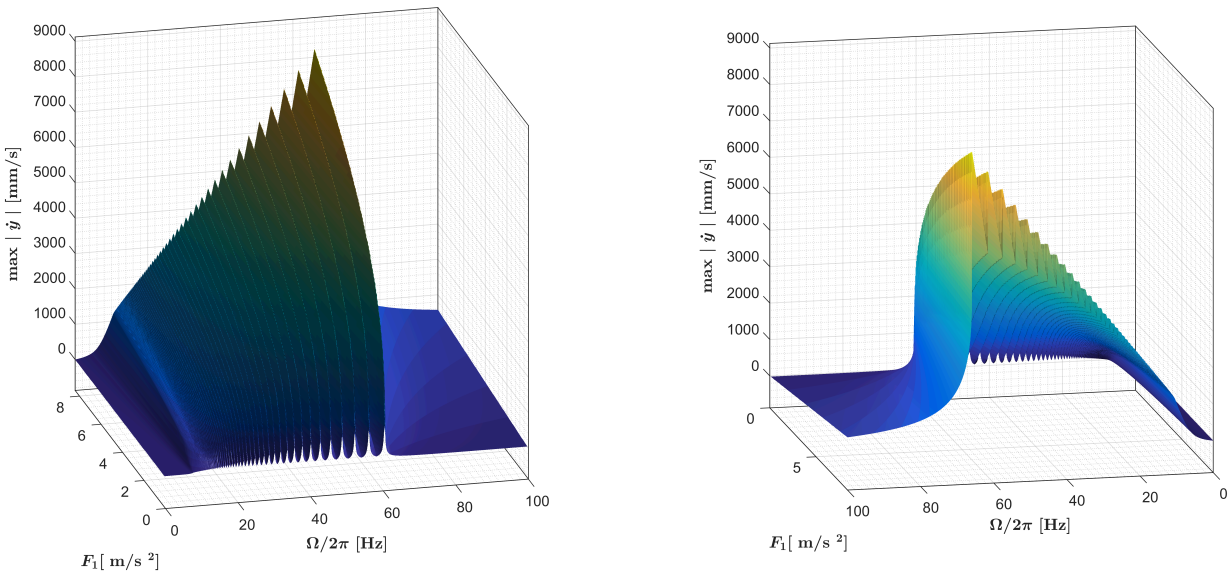

Figure 4.25: Maximum relative velocity response (considering the best values of Δd) according to the external frequency for every excitation amplitudes. The ξ was set to 0.05. Parameters from table 3.1 were used.

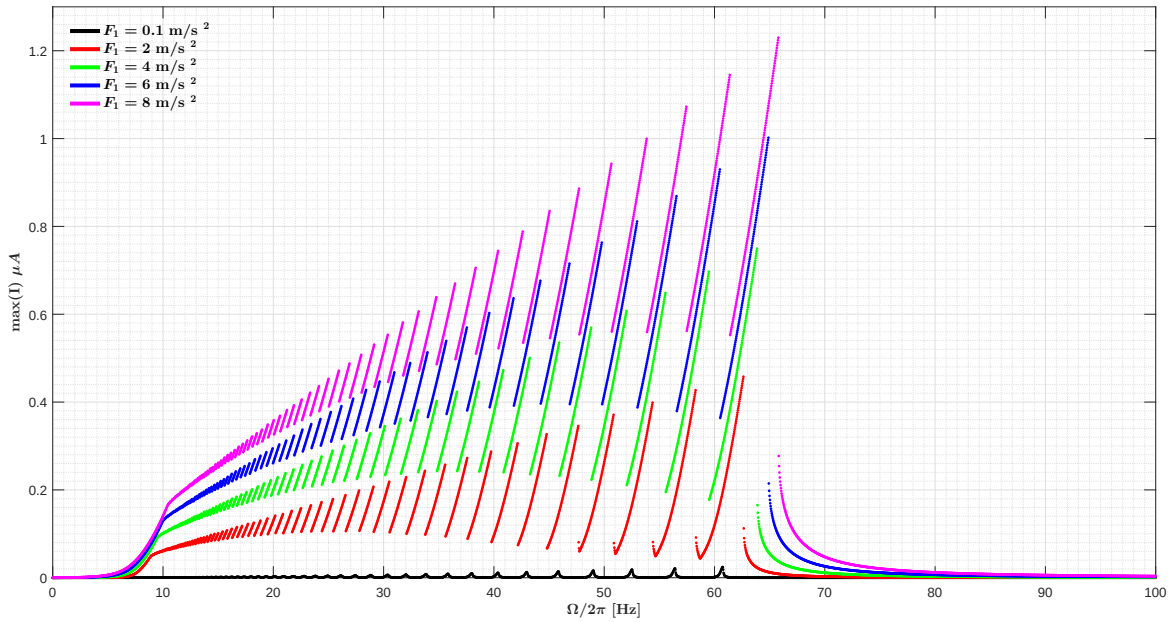

Figure 4.26: Maximum electric current (considering the best values of Δd) according to the external frequency for different excitation amplitudes. The ξ was set to 0.05. Parameters from table 3.1 were used.

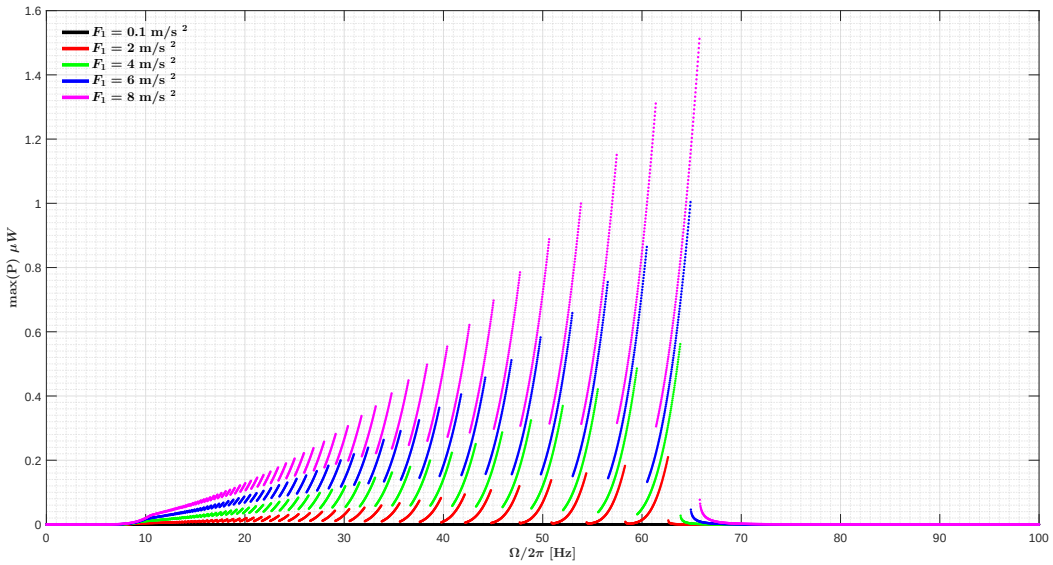

Figure 4.27: Maximum electric power (considering the best values of Δd) according to the external frequency for different excitation amplitudes. The ξ was set to 0.05. Parameters from table 3.1 were used.

In order to achieve such maximums, figures 4.28 and 4.29 describe the values that Δd must take to accomplish the system's best performance and are in agreement with the previous analysed graphics.

The best Δd for any the excitation is always positive. Δd adopts a value of 3.5 mm for frequencies very close to zero. Considering an acceleration of 0.1 m/s^2, the ideal Δd decreases in a linear way to 1 mm until frequencies of 8 Hz are achieved. On the other hand, when an acceleration of 8 m/s^2 is considered, Δd evolves linearly up to a 10 Hz frequency, reaching the 0.3 mm value. For higher than mentioned frequencies, there is an offset increase until Δd reaches its maximum (Δd=d0/4 mm), at a frequency of 60 Hz. Hence, the most efficient harvester's configuration for higher than 60 Hz frequencies is achieved when $\Delta d = d_0/4$ mm.

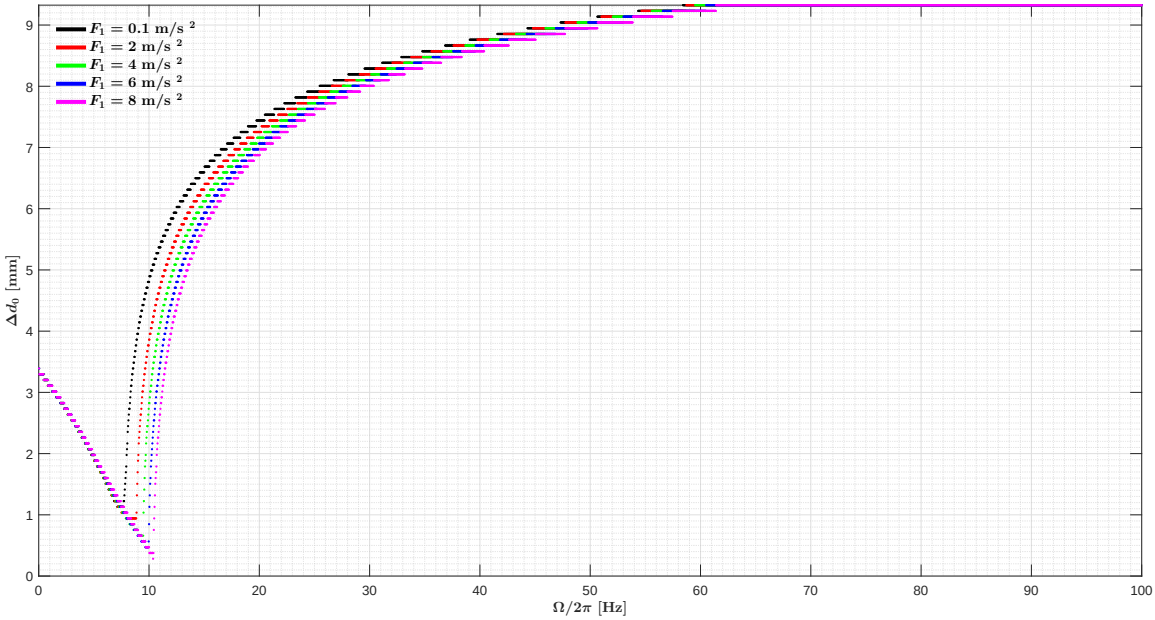

Figure 4.28: Optimized Δd length for different excitation amplitudes. The ξ was set to 0.05. Parameters from table 3.1 were used.

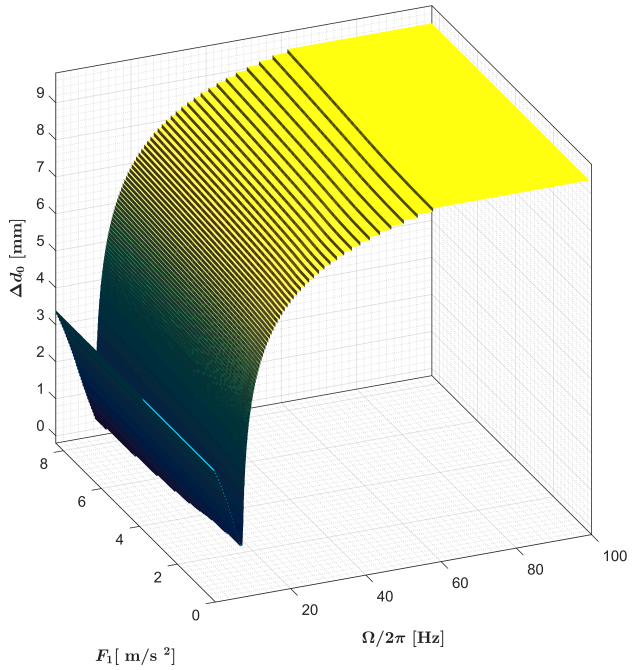

Figure 4.29: Optimized Δd length for every excitation amplitudes. The ξ was set to 0.05. Parameters from table 3.1 were used.

Figures 4.30, 4.31 and 4.32 portray the simulated results when fixed acceleration and variable damping factor are taken in consideration, in which Δd has optimal values according to figure 4.33. When 10 and 60 Hz frequency values are considered, the change in the damping coefficient from 0.4 to 0.05 translates in a 180.4% and 8% increase in velocity, 7.8 and 1.16 current gain improvements and 61.3 and 1.4 power gains, respectively.

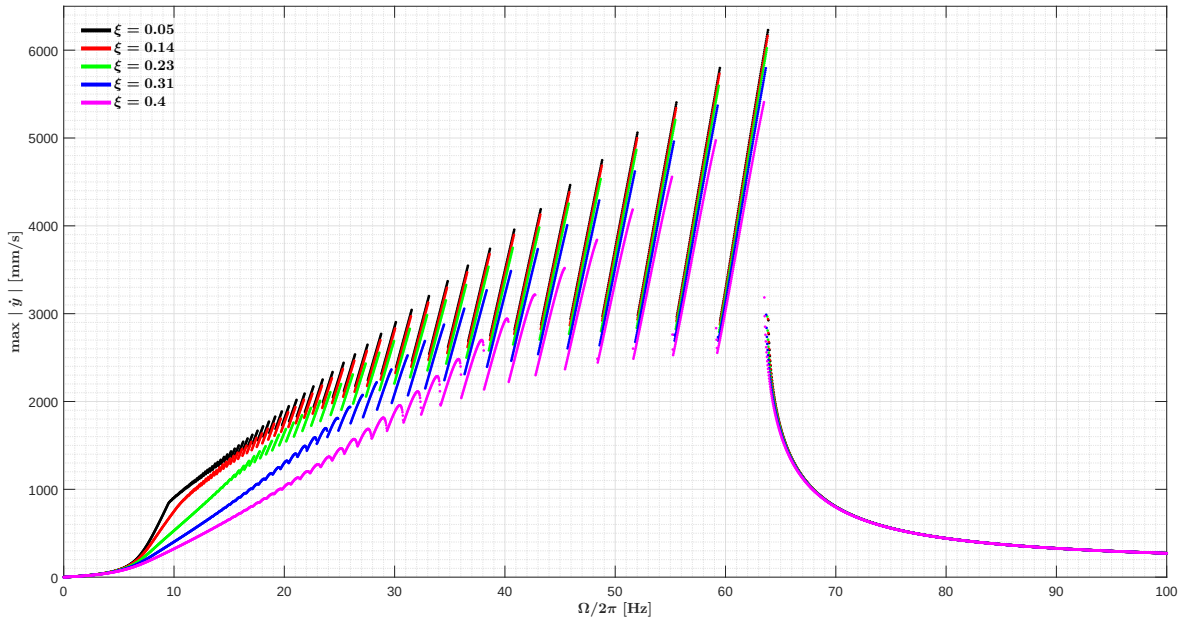

Figure 4.30: Maximum relative velocity response (considering the best values of Δd) according to the external frequency for different excitation amplitudes. The F_1 was set to 4 m/s^2. Parameters from table 3.1 were used.

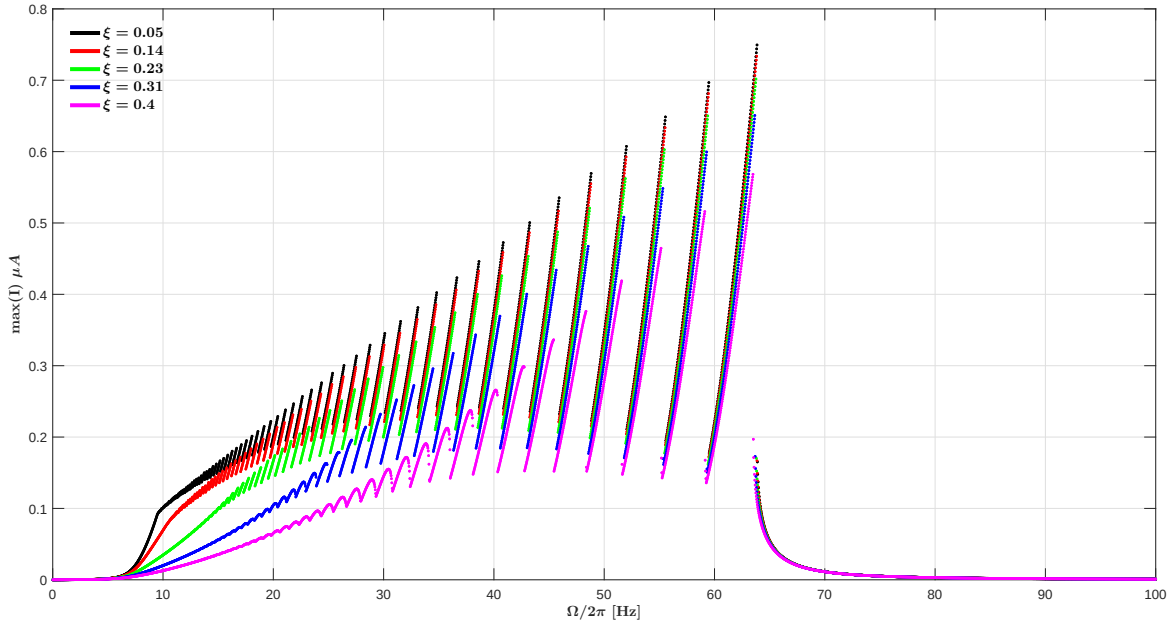

Figure 4.31: Maximum electric current (considering the best values of Δd) according to the external frequency for different excitation amplitudes. The F_1 was set to 4 m/s^2. Parameters from table 3.1 were used.

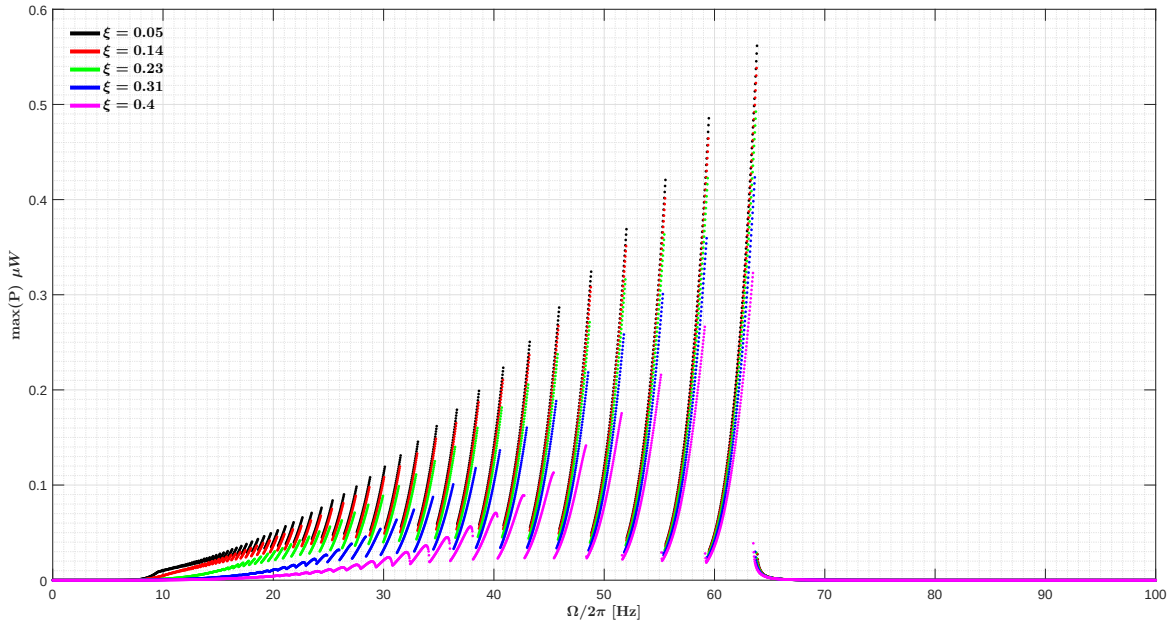

Figure 4.32: Maximum electric power (considering the best values of Δd) according to the external frequency for different excitation amplitudes. The F_1 was set to 4 m/s^2. Parameters from table 3.1 were used.

The conclusion that higher damping values are associated with higher Δd values for frequencies lower than 20 Hz can be drawn from figure 4.33. The minimum optimal Δd is observed when ξ=0.4 and with a 5 Hz oscillation. The highest difference in Δds between coefficients of 0.4 and 0.05 occurs at 9.5 Hz (which corresponds to 4 mm).

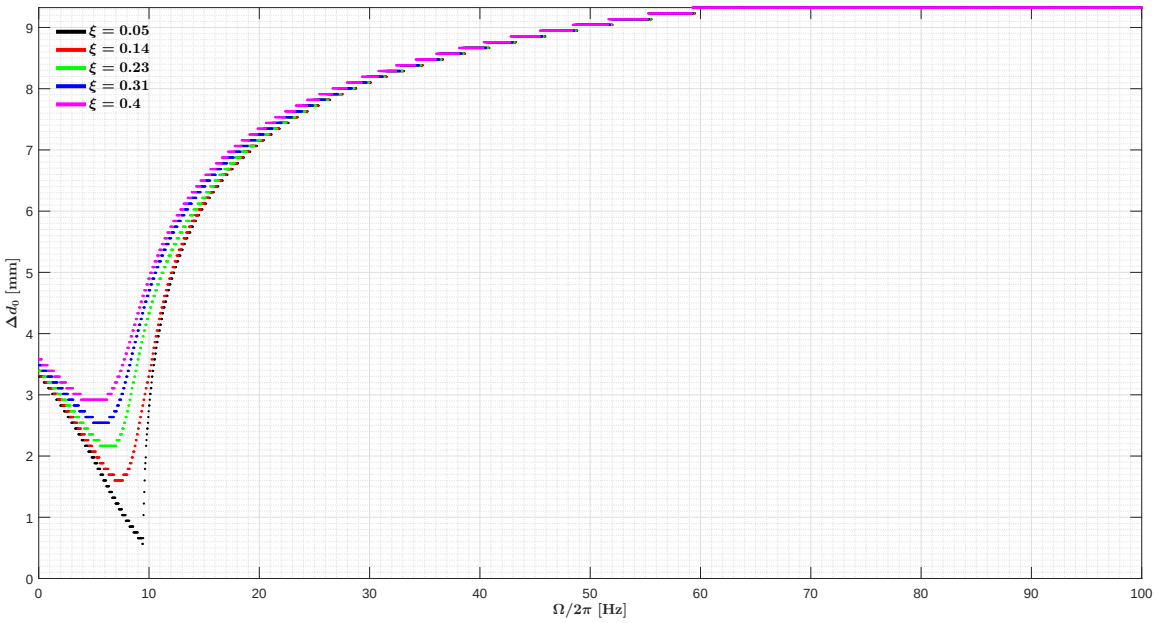

Figure 4.33: Optimized Δd length for different excitation amplitudes. The F_1 was set to 4 m/s^2. Parameters from table 3.1 were used.

The impact of the mass of the levitating magnet on the system dynamics' was also studied.

The system response was analysed under three different circumstances for mass variations: when the generator length has a minimum, zero and maximum offset, which corresponds to a Δd of -$d_0/2$, 0 and $d_0/4$ mm, respectively. In each individual simulation, a constant damping of 0.05 and five different accelerations were considered.

The results presented in figure 4.34 refer to a harvester with $\Delta d = -d_0/2$ mm and the mass in the [10, 500] [g] range. For an excitation of 4 m/s^2, increases from 10 to 195 g in mass result in both growth of the levitating magnet's dynamics (from 300 to 1200 mm/s) and frequency decrease (from 19 to 7 Hz). For mass variations of 195<m<500 g and regarding the same excitation, velocity and frequency reach values of 2350 mm/s and 10 Hz, respectively. Regarding this configuration, the minimal resonance frequency is 5.8 Hz, which corresponds to an acceleration of 0.1 m/s^2.

In which the harvester without offsets is concerned, the maximum relative velocity progression as a function of frequency is represented in figure 4.35, for masses between 10 and 330 g. For example, for an acceleration of 4 m/s^2, the 10<m<19.5 g resonance frequency decreases from 11 to 9.5 Hz. The lowest resonant frequencies prevail with an approximated 19.5 g (current mass) and harvester's length with Δd=0 mm (current length). There is a substantial increase in velocity and frequency when m>19.5 g. When m=330 g (and considering the same Δd and excitation), velocity reaches 2100 mm/s and frequency equals 85 Hz. The mass varied until a limit of growth of 330 g, since behaviors beyond the stipulated frequency limits are not the subject matter of this study.

For each mass, the course of the maximum relative velocity when $\Delta d = d_0/4$ mm is exposed in figure 4.36 The mass varied from 10 to 25 g in this simulation. With increments in the mass, an increase in frequency and velocity can be seen. For instance, given a 4 m/s^2 excitation, the frequency grows from 27 to 88 Hz and the velocity changes from 2100 to 9300 mm/s.

It is known that when an approach to a linear system is made and there is an increase in the levitating magnet's mass, there is a decrease in both frequency and velocity's dynamics. More complex dynamics arise when studying a non linear system. These complex dynamics requires further research.

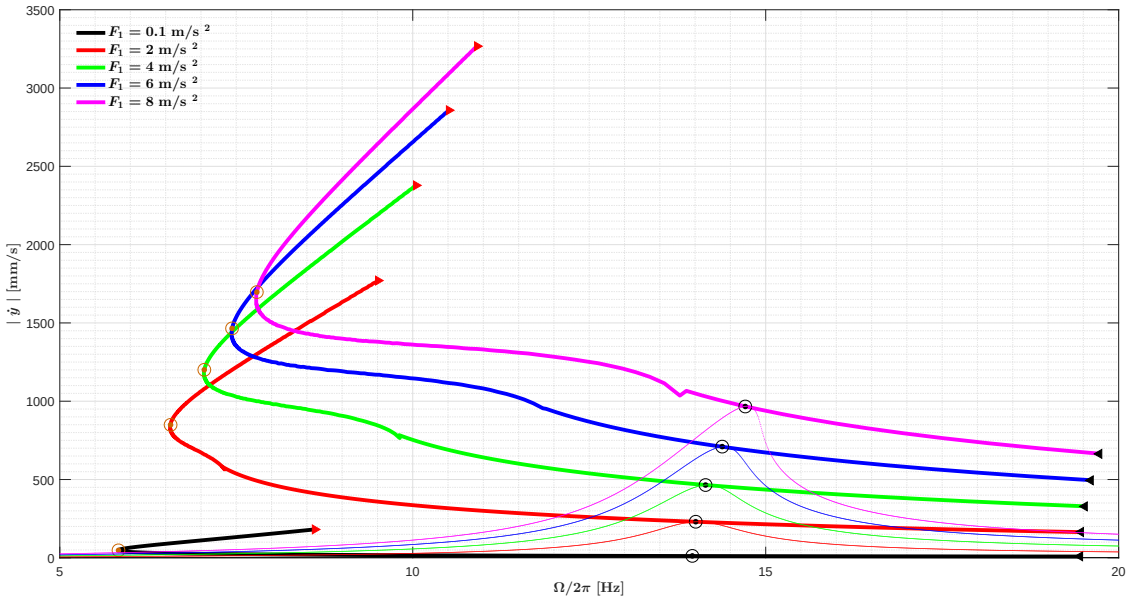

Figure 4.34: Maximum relative velocity response and combined frequency. Each trajectory describes the dynamics while varying mass from 10 to 500 g (from black to red triangle; m=19.5 g is identified with a black circle dot; m=195 g is identified with a orange circle dot). The F_1 was set to 4 m/s^2, ξ was set to 0.05 and Δd was set to -$d_0/2$. Parameters from table 3.1 were used.

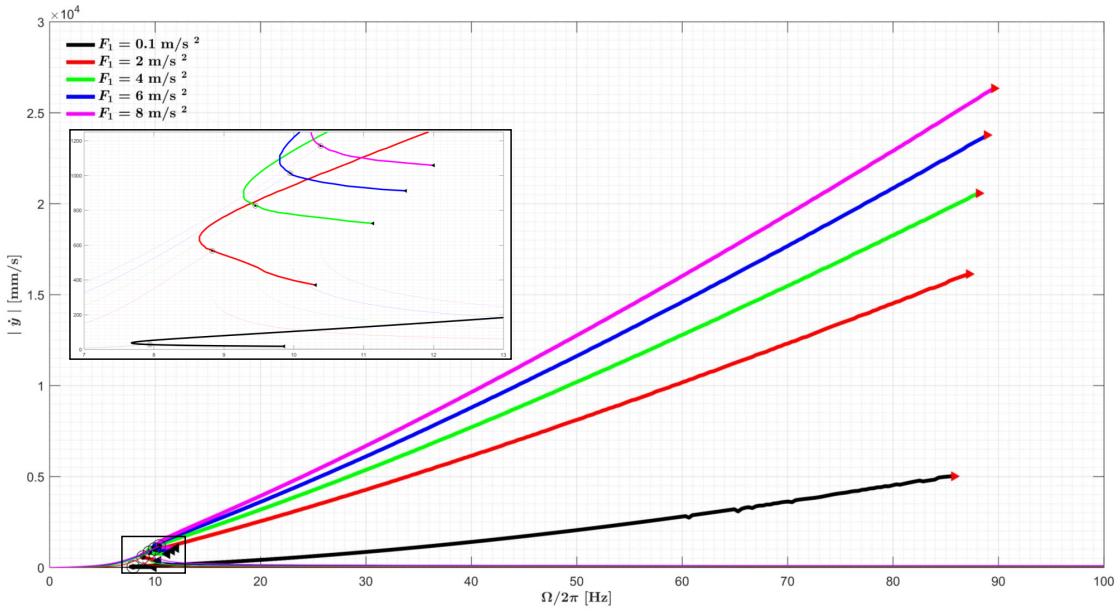

Figure 4.35: Maximum relative velocity response and combined frequency. Each trajectory describes the dynamics while varying mass from 10 to 300 g (from black to red triangle; m=19.5 g is identified with a black circle dot). The F_1 was set to 4 m/s^2, ξ was set to 0.05 and Δd was set to 0. Parameters from table 3.1 were used.

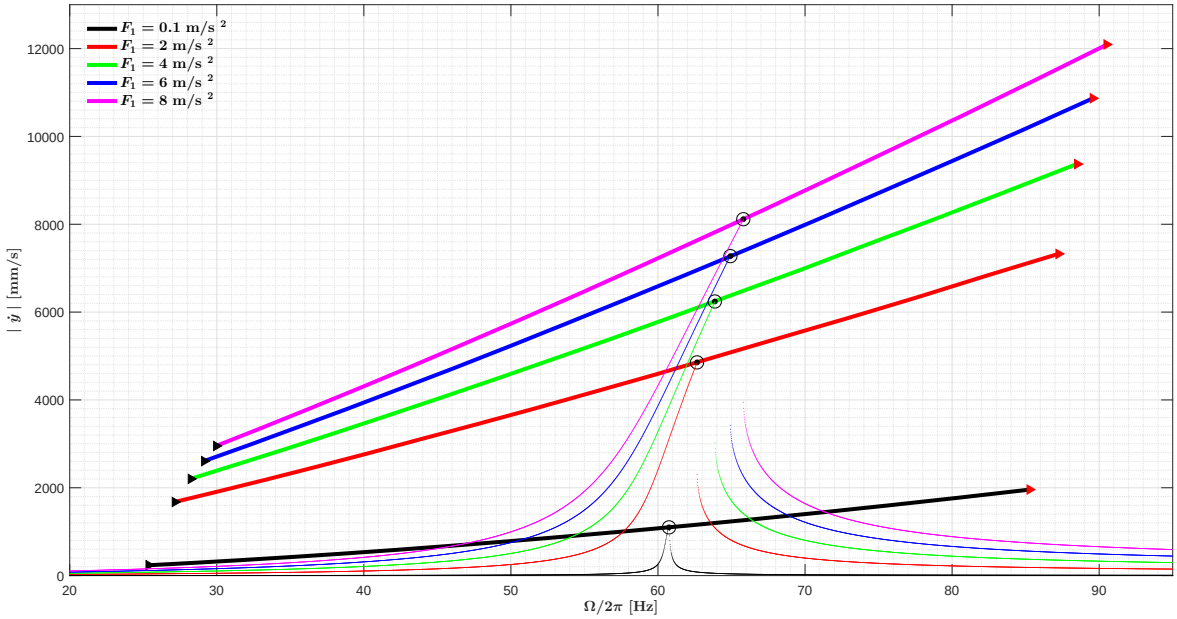

Figure 4.36: Maximum relative velocity response and combined frequency. Each trajectory describes the dynamics while varying mass from 10 to 25 g (from black to red triangle; m=19.5 g is identified with a black circle dot). The F_1 was set to 4 m/s^2, ξ was set to 0.05 and Δd was set to $d_0/4$. Parameters from table 3.1 were used.

4.2 Parameterized model

The parameterized harvester's analysis focuses on the same aspects discussed in the previous section.

Firstly, the relative velocity behaviour for five Δd variations is shown in figure 4.37. For a better understanding about the dynamics regarding the frequency and harvester's length, a three-dimensional illustration is also presented in figure 4.38. This harvester's resonance frequency for a Δd=0 mm is 225 Hz, which corresponds to a velocity of 3.14×10^4 mm/s. When $\Delta d = -d_0/2$ mm, a significant reduction in both velocity (decreases 99.7% to 85 mm/s) and frequency (decreases 97.3% to 6.1 Hz) is observed. As expected for this generator and regarding the same frequencies, current and power's behavior is directly related to the velocity's dynamics. From $0 > \Delta d > -d_0/2$ mm, current evolves from 1.1×10^{-13} to 1.2×10^{-11} A (which corresponds to a 106.3 gain) and power goes from 1.2×10^{-20} to 1.4×10^{-16} W (establishing a 1.1×10^4 gain), as it can be observed from figures 4.39 and 4.40. Due to the high damping coefficient, the curves never enter the hysteresis zone and have different shapes than the ones accounted in the previous section. For small lengths and after reaching the resonant frequency, the velocity decreases less abruptly than in the region to the left of the resonance zone.

The three-dimensional figure (4.38) highlights an abrupt velocity variation zone that starts in 5 m/s. This is the consequence of the used Δd resolution. In fact, lower resolutions would have resulted in lower peak-to-peak values. The 112 μm resolution (adopted in the $\Delta d > -d_0/2$ mm interval) is insufficient to eliminate these variations.

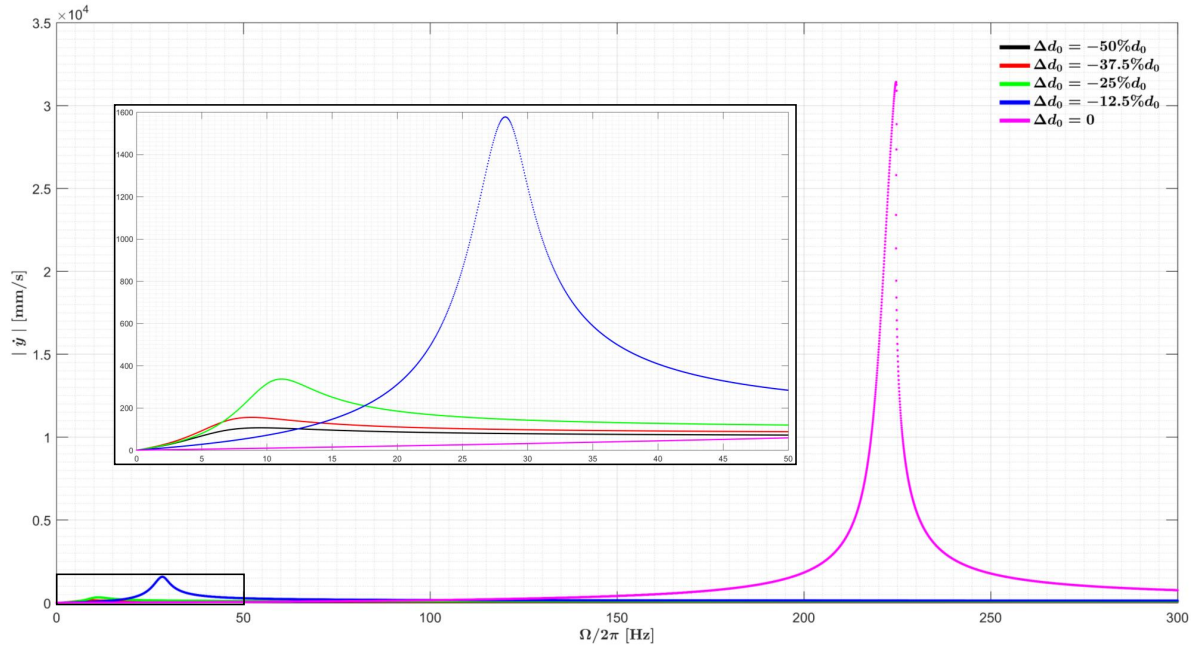

Figure 4.37: Relative velocity response for different Δd lengths. The F_1 was set to 4 m/s^2. Parameters from table 3.2 were used.

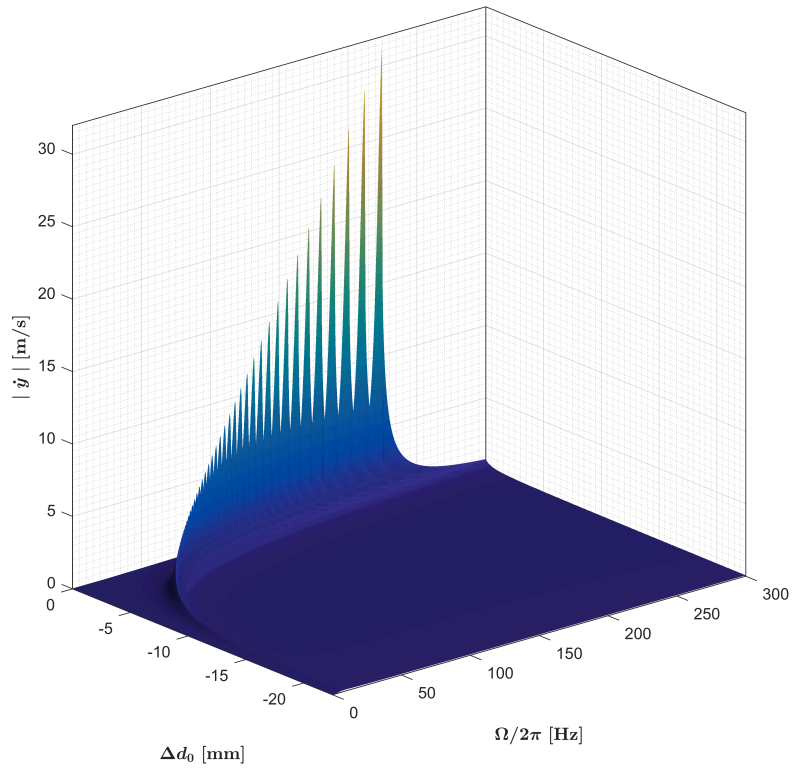

Figure 4.38: Relative velocity response for every Δd lengths. The F_1 was set to 4 m/s^2. Parameters from table 3.2 were used.

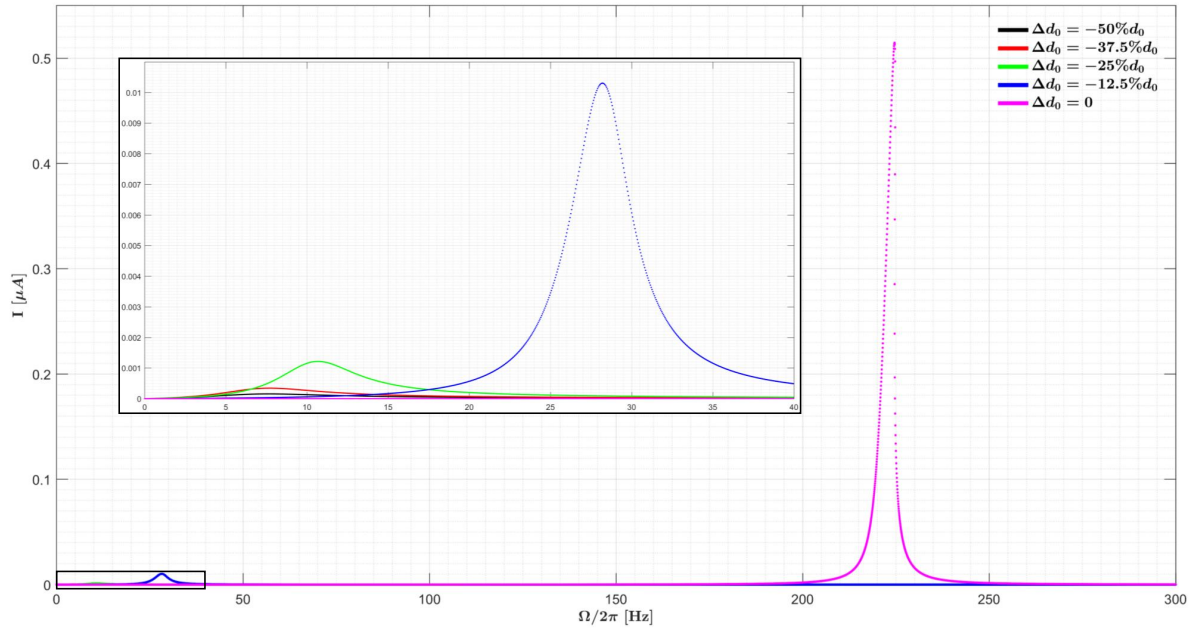

Figure 4.39: Electric current for different Δd lengths. The F_1 was set to 4 m/s^2. Parameters from table 3.2 were used.

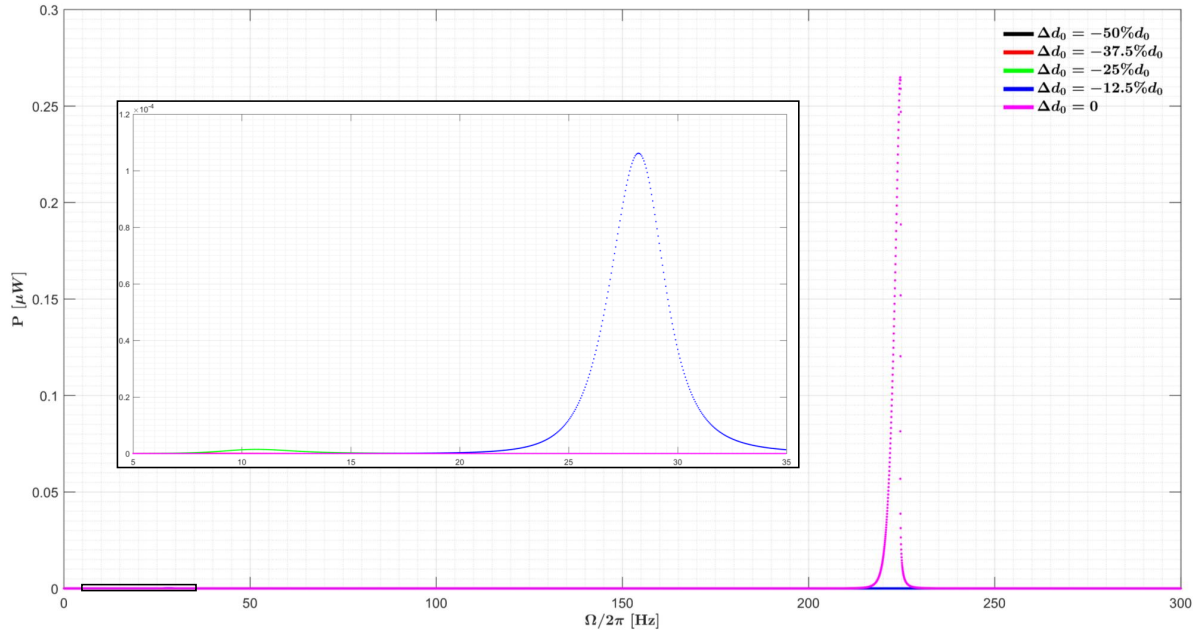

Figure 4.40: Electric power for different Δd lengths. The F_1 was set to 4 m/s^2. Parameters from table 3.2 were used.

Figures 4.41, 4.43 and 4.44 show the maximum velocity, current and power reachable for each frequency and Δd, for five external excitations. Figure 4.41 and 4.42 shows that for Δd <-10 mm variations, no significant differences are observed in the maximum velocity and only slightly changes are noticed as Δd approaches 0 mm. For example, when Δd=0 mm, the maximum velocities for 0.1, 2, 4, 6 and 8 m/s^2 excitations are 775, 1.6×10^4, 3.1×10^4, 4.2×10^4, 4.8×10^4 mm/s, respectively. When faced with the same excitations and Δd, current and power are 3.2×10^{-10}, 1.3×10^{-7}, 5.1×10^{-7}, 8.9×10^{-7}, 1.2×10^{-6} A and 1×10^{-13}, 1.6×10^{-6}, 2.6×10^{-7}, 8×10^{-7}, 1.4×10^{-6} W, respectively.

Figure 4.45 labels the frequency associated to figures 4.41, 4.43 and 4.44. These velocity, current and power gains come with frequency changes. As Δd is moved away from -$d_0/2$ mm, frequency tends to remain approximately constant. In contrast, significant frequency increases are expected as Δd approaches $d_0/2$ mm (and Δd >-12 mm). The lowest frequencies (to which the velocity is maxim) occur for lengths between $-d_0/2 < \Delta d <$-12 mm. The overall dynamics considering the effects of Δd, excitations and frequency are illustrated in figure 4.46.

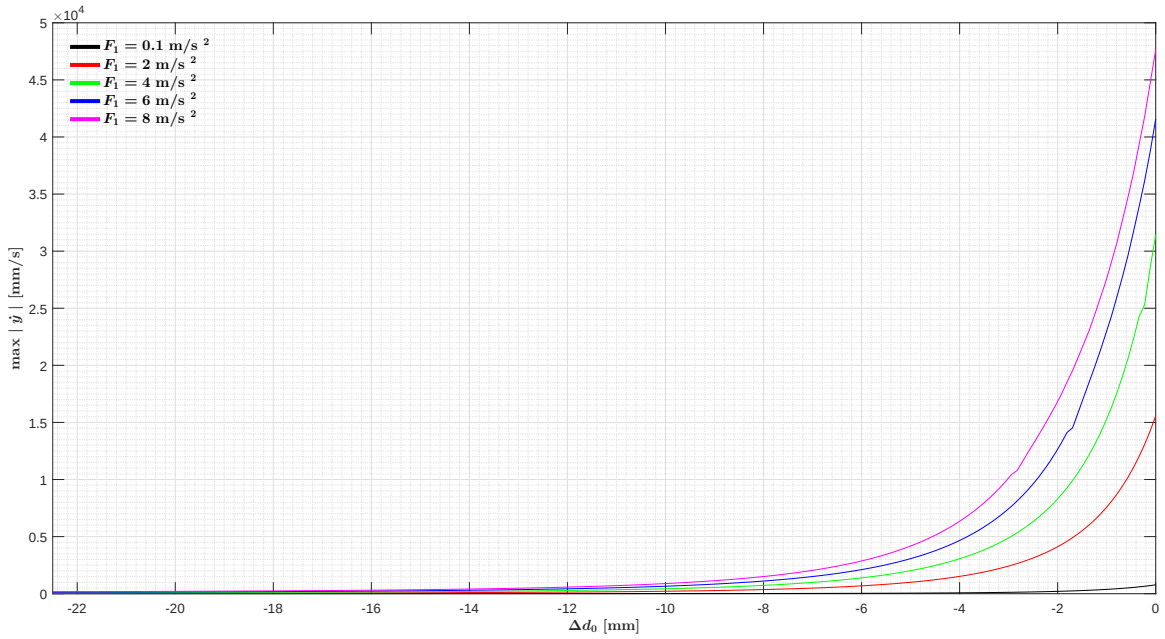

Figure 4.41: Maximum relative velocity response in function of Δd for different excitation amplitudes. Parameters from table 3.2 were used.

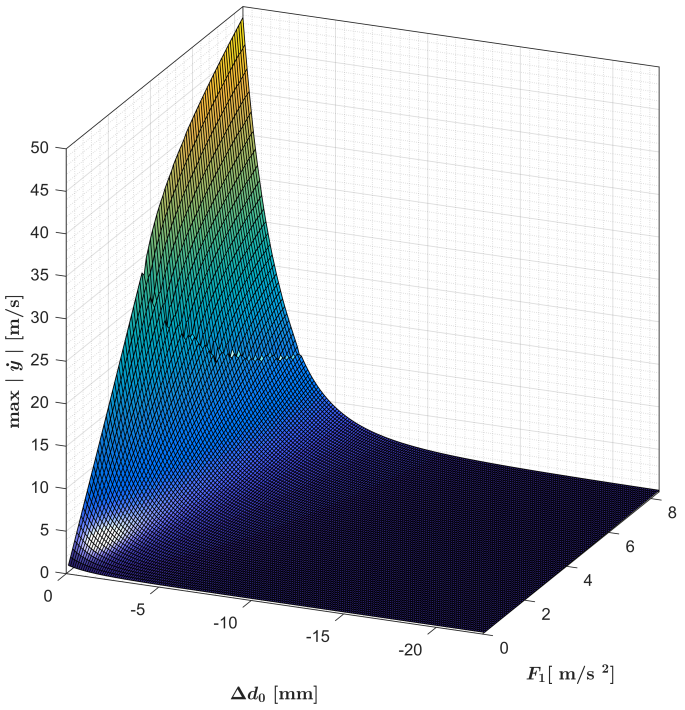

Figure 4.42: Maximum relative velocity response in function of Δd for every excitation amplitudes. Parameters from table 3.2 were used.

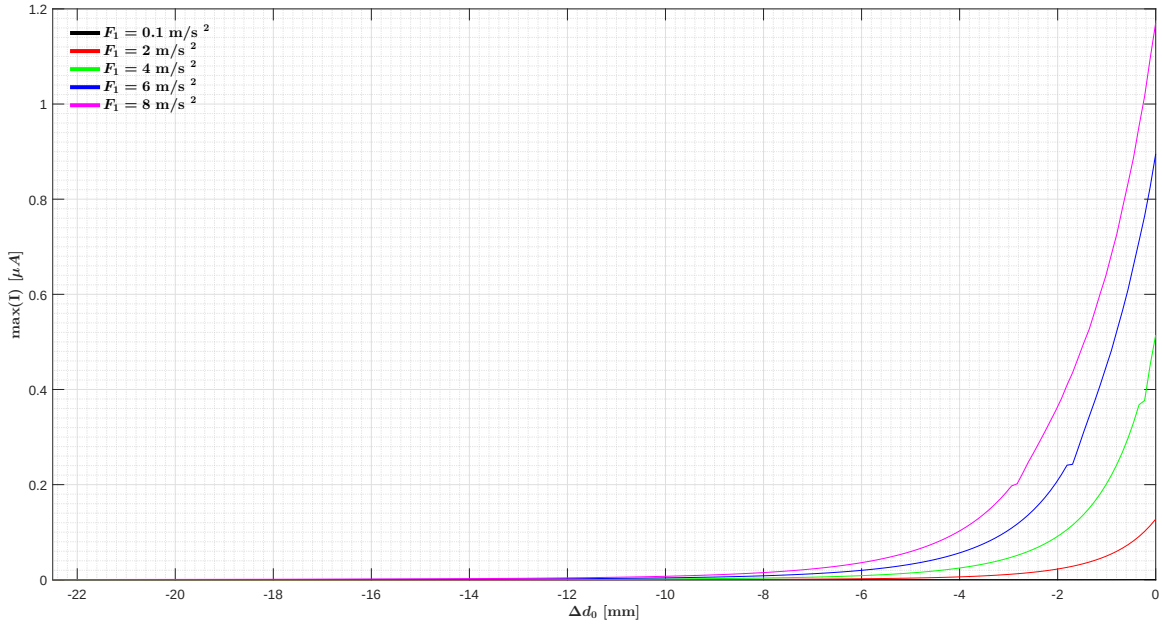

Figure 4.43: Maximum electric current in function of Δd for different excitation amplitudes. Parameters from table 3.2 were used.

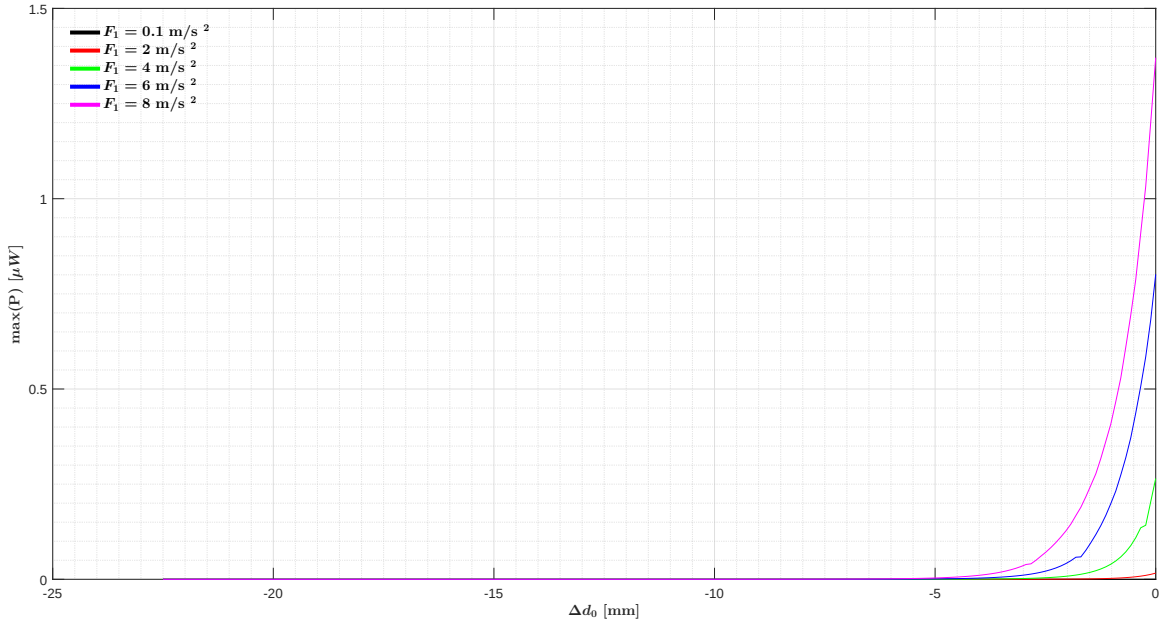

Figure 4.44: Maximum electric power in function of Δd for different excitation amplitudes. Parameters from table 3.2 were used.

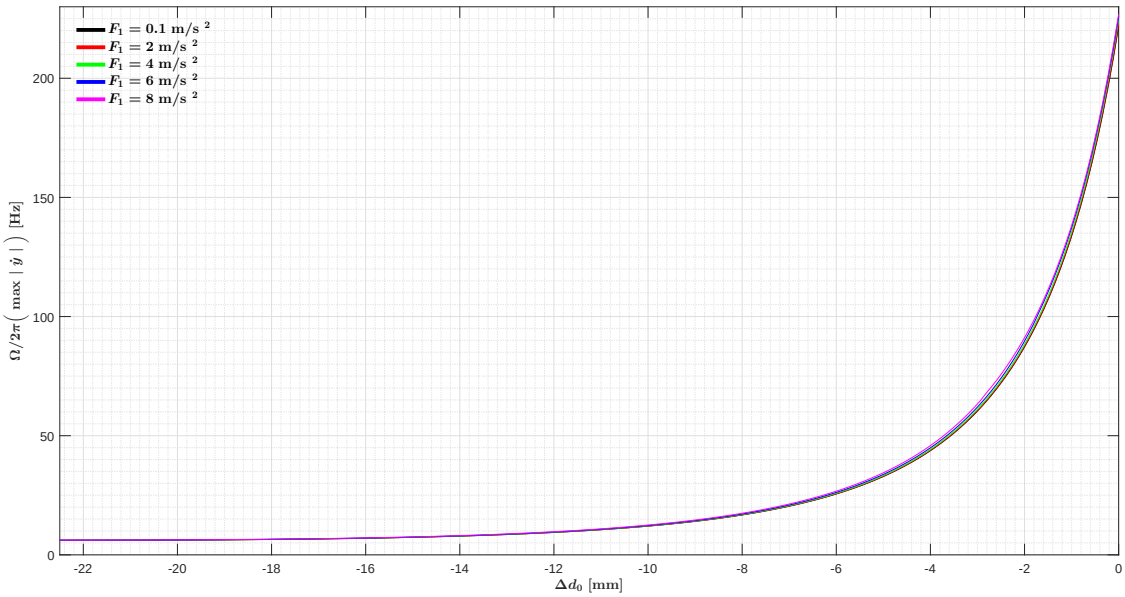

Figure 4.45: Matching frequency to maximum relative system response in function of Δd for different excitation amplitudes. Parameters from table 3.2 were used.

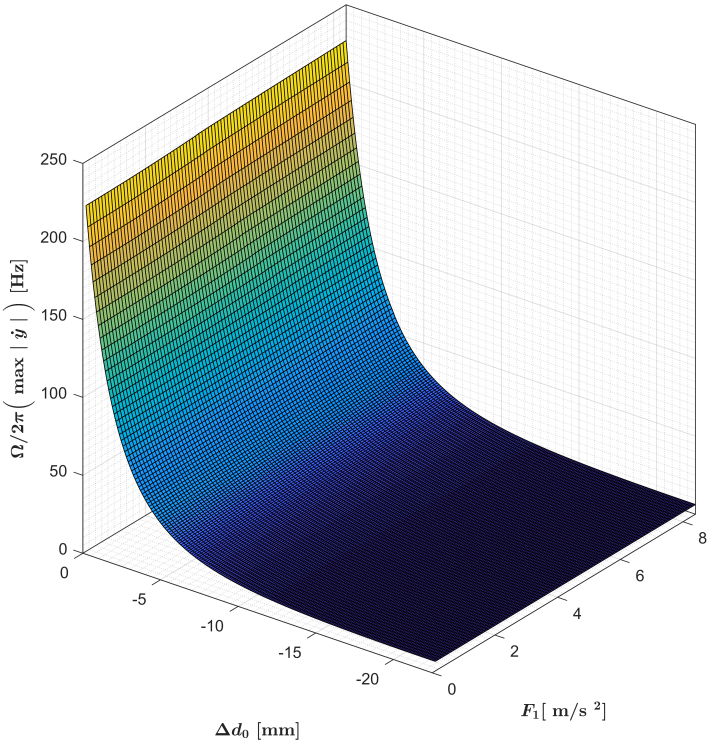

Figure 4.46: Matching frequency to maximum relative system response in function of Δd for every excitation amplitudes. Parameters from table 3.2 were used.

For higher variations of Δd, the associated resonant frequency and velocity / current/ power tend to increase as it can be observed from figures 4.47, 4.48 and 4.49.

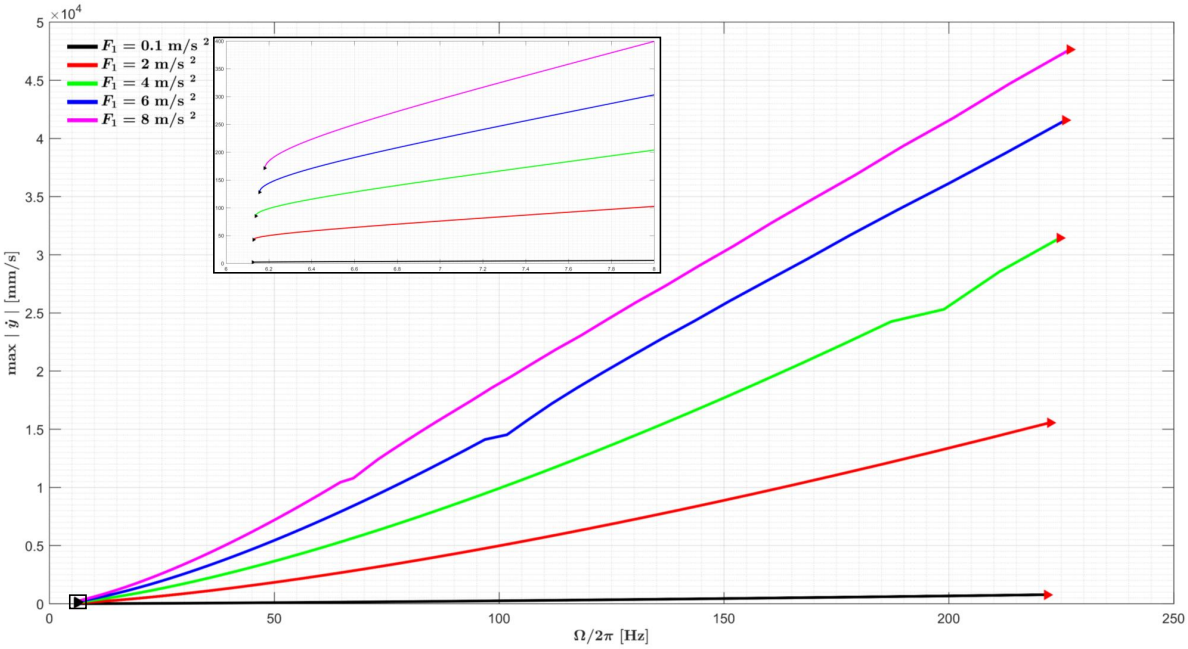

Figure 4.47: Maximum relative velocity response and combined frequency. Each trajectory describes the dynamics while varying Δd from -$d_0/2$ to 0 (from black to red triangle). Parameters from table 3.2 were used.

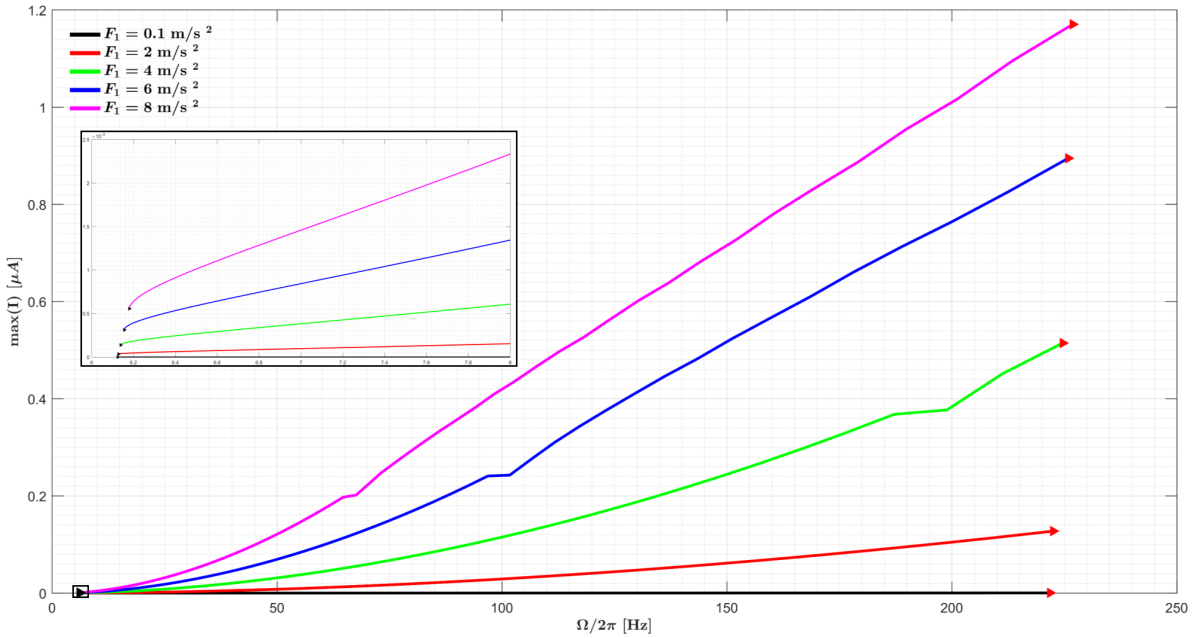

Figure 4.48: Maximum electric current and combined frequency. Each trajectory describes the dynamics while varying Δd from -$d_0/2$ to 0 (from black to red triangle). Parameters from table 3.2 were used.

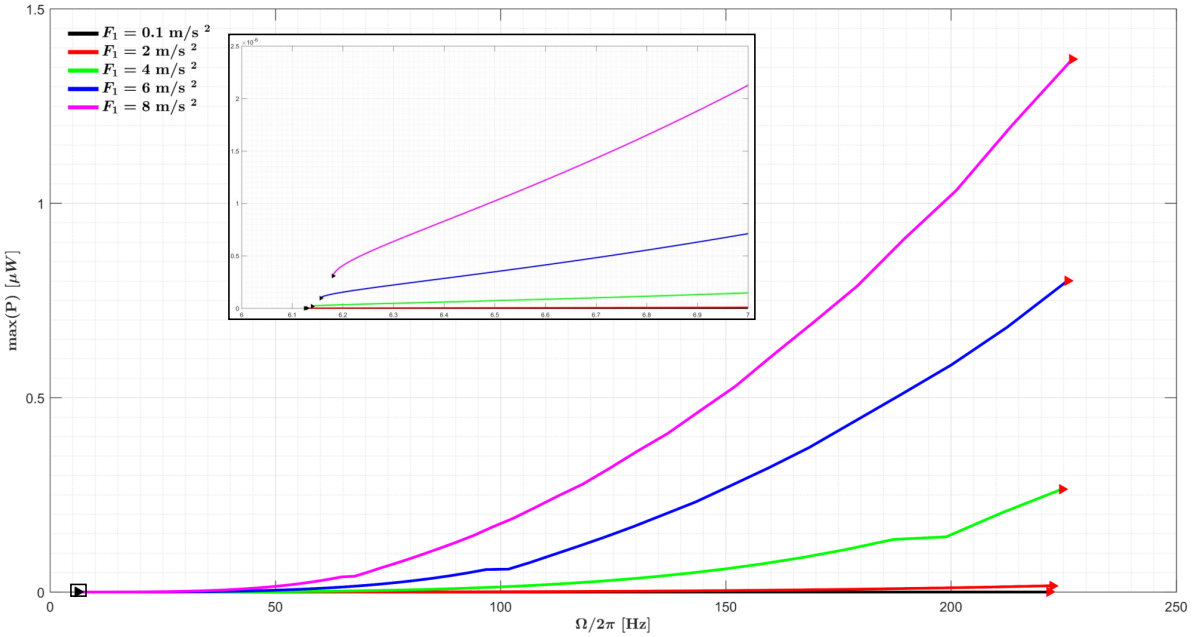

Figure 4.49: Maximum electric power and combined frequency. Each trajectory describes the dynamics while varying Δd from -$d_0/2$ to 0 (from black to red triangle). Parameters from table 3.2 were used.

The adjustment of the harvester's length when facing excitation variations is demonstrated in figures 4.50, 4.52 and 4.53, in what maximum velocity, current intensity and power in function of frequency is concerned, respectively. Figure 4.51 highlights the overall dynamics taking the effects of frequency and excitation on maximum velocity into account (considering the best Δd).

The next analysis compares the use and the lack of adaptive control. For 0.1, 4 and 8 m/s^2 excitations, the velocity gains are 33.6, 33.4, 32.8 for a 10 Hz frequency, 58.6, 62.5, 61.4 for a 50 Hz frequency and 47.7, 60.3, 45.4 for a 100 Hz frequency, respectively. Concerning 0.1, 4 and 8 m/s^2 excitations and frequencies of 10, 50 and 100 Hz, the current gains are 1.1×10^3, 3.4×10^3, 2.3×10^3 (for 0.1 m/s^2); 1.1×10^3, 3.9×10^3, 3.6×10^3 (for 4 m/s^2); 1.1×10^3, 3.8×10^3, 2.1×10^3 (for 8 m/s^2), respectively. Regarding the same excitations and frequencies, the power gains are 1.3×10^6, 1.2×10^7, 5.2×10^6 (for 0.1 m/s^2); 1.2×10^6, 1.5×10^7, 1.3×10^7 (for 4 m/s^2); 1.2×10^6, 1.4×10^7, 4.2×10^6 (for 8 m/s^2), respectively.

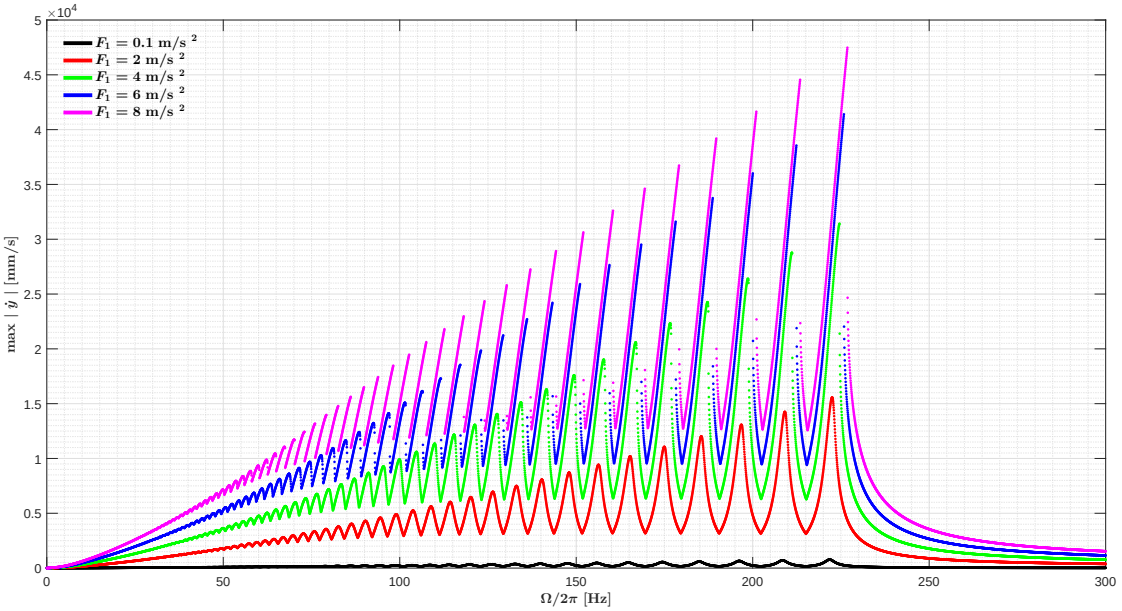

Figure 4.50: Maximum relative velocity response (considering the best values of Δd) according to the external frequency for different excitation amplitudes. Parameters from table 3.2 were used.

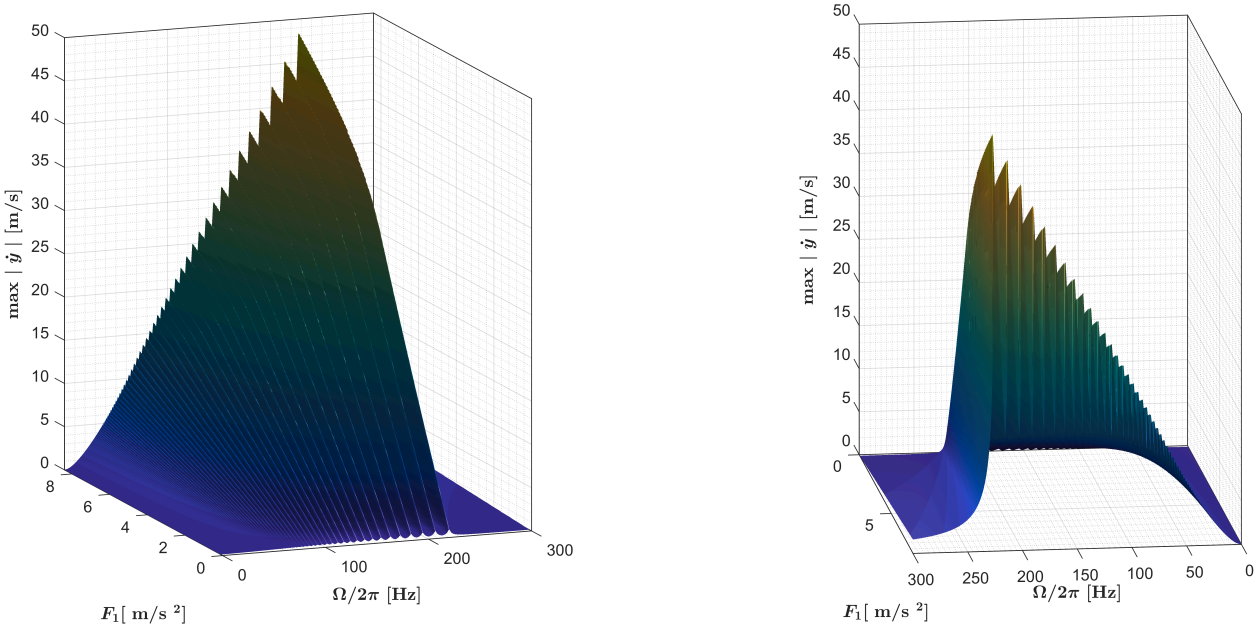

Figure 4.51: Maximum relative velocity response (considering the best values of Δd) according to the external frequency for every excitation amplitudes. Parameters from table 3.2 were used.

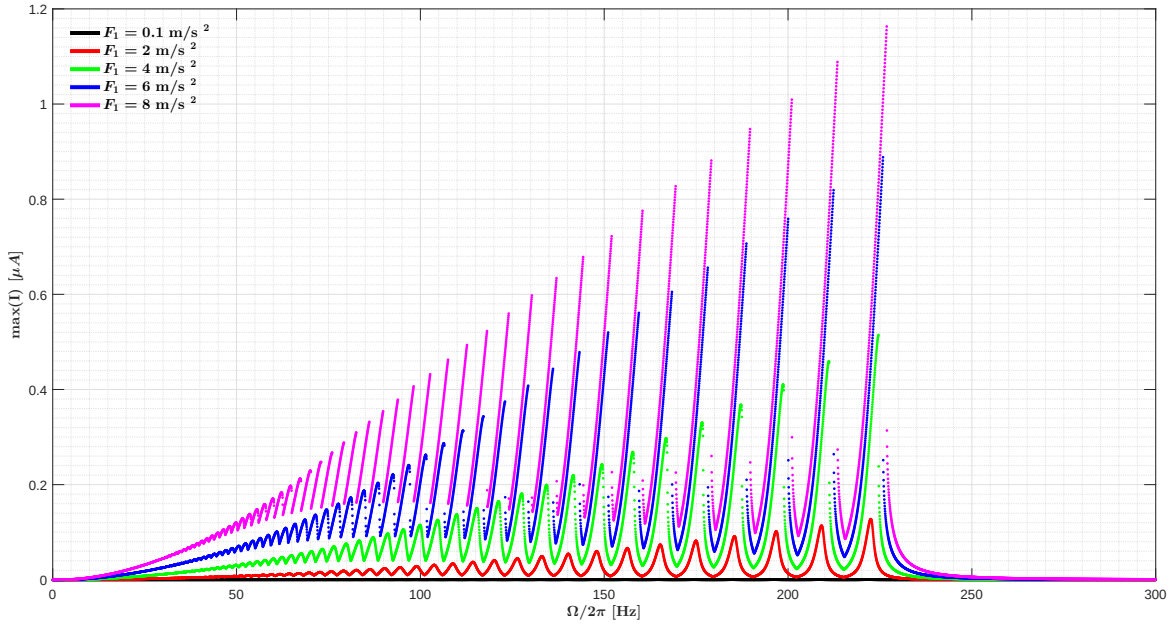

Figure 4.52: Maximum electric current (considering the best values of Δd) according to the external frequency for different excitation amplitudes. Parameters from table 3.2 were used.

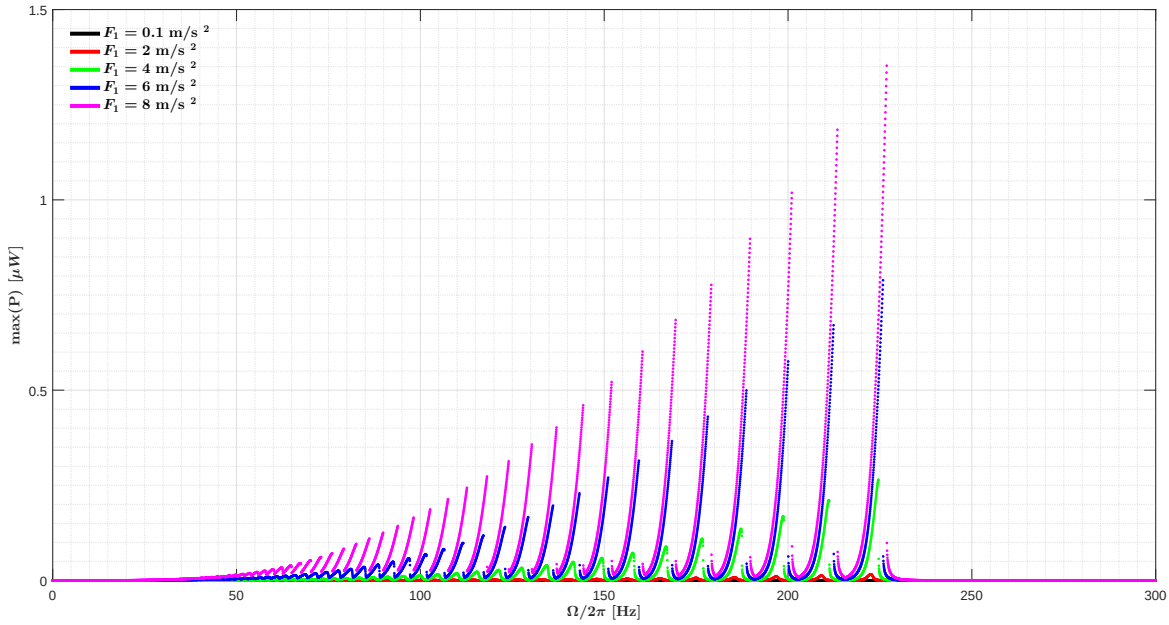

Figure 4.53: Maximum electric power (considering the best values of Δd) according to the external frequency for different excitation amplitudes. Parameters from table 3.2 were used.

The ideal Δd decreases from -15.4 to -15.6 mm, for frequencies up to 2.5 Hz. For higher than 2.5 Hz values, the best Δd rises until a frequency of 215 Hz and achieves its maximum. The optimal Δd is very similar for different excitations.

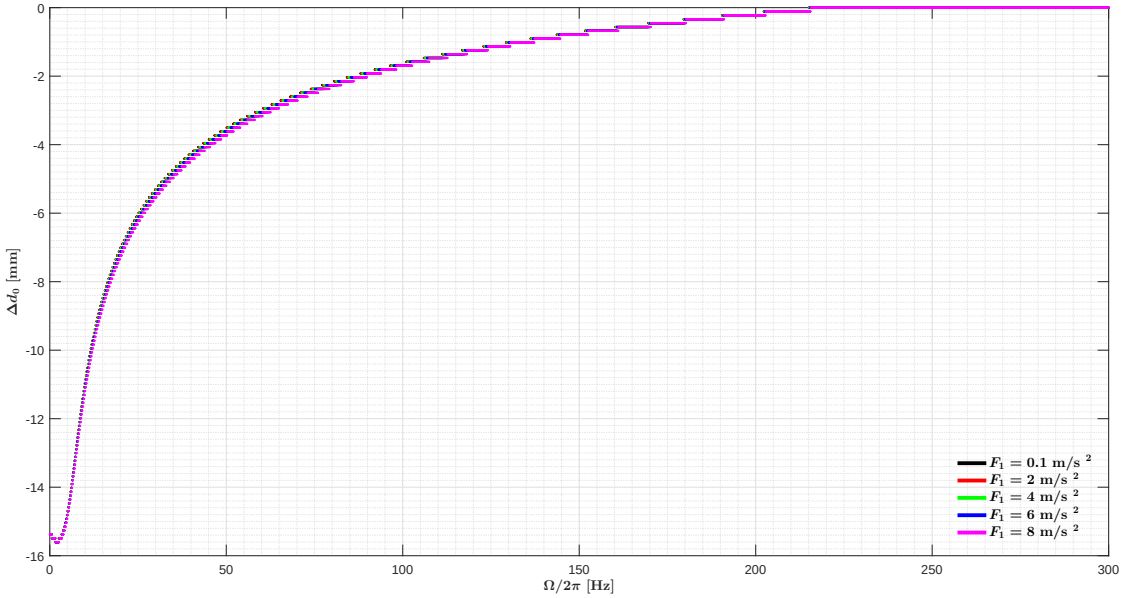

Figure 4.54: Optimized Δd length for different excitation amplitudes. Parameters from table 3.2 were used.

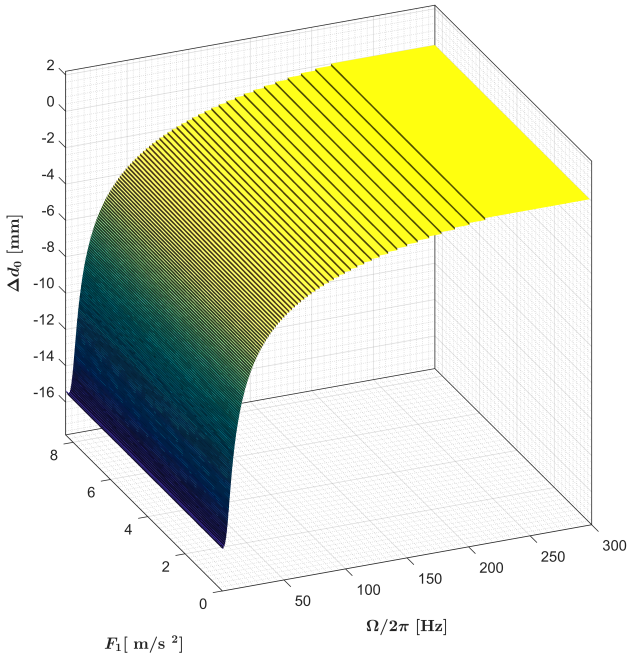

Figure 4.55: Optimized Δd length for every excitation amplitudes. Parameters from table 3.2 were used.

4.3 Overview - velocity gains

As this study is mainly focused on the dynamics of the levitating magnet, figures 4.56 and 4.57 portray the velocity gains for both generators when taking the effects of frequency and five excitation considering the best Δd. The electromagnetic harvester proposed by Mann and Sims [14] provides higher velocity gains for lower excitation amplitudes. The parametrized harvester describes the maximum velocity gain (about 65) when vibrating with a frequency of 50 Hz.

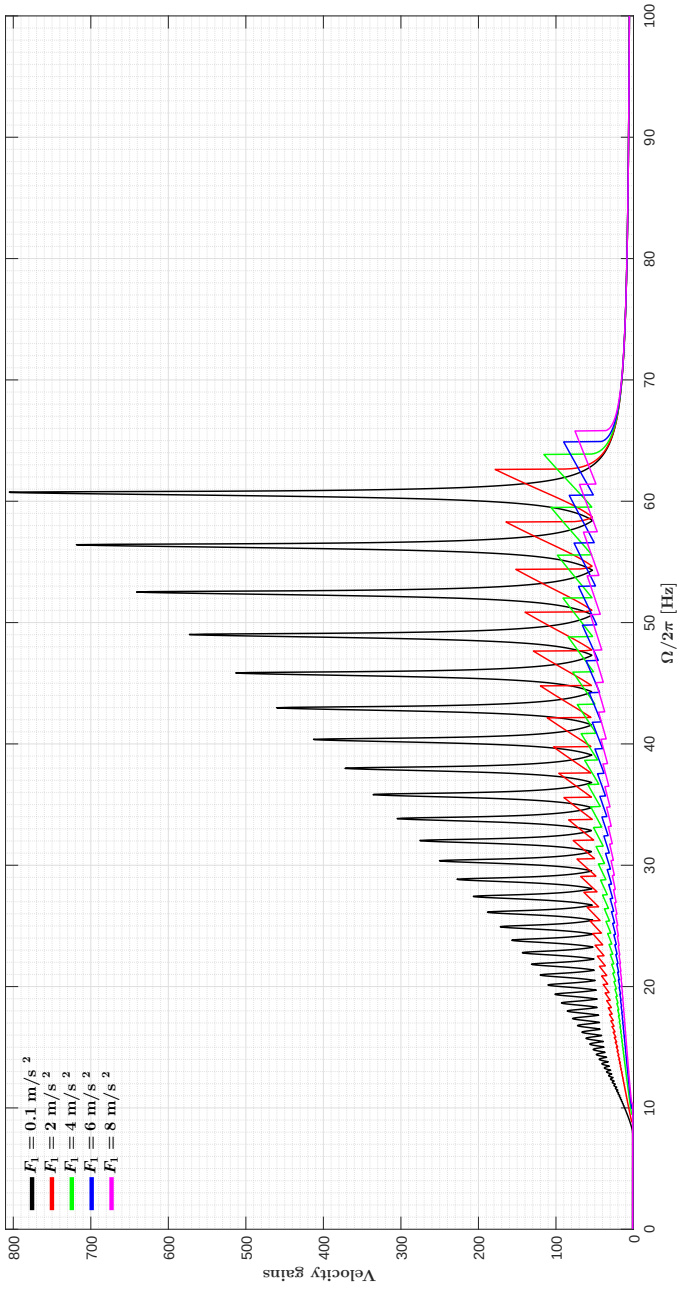

Figure 4.56: Velocity gains according to the external frequency for different excitation amplitudes in which concerns the electromagnetic harvester proposed by Mann and Sims [14]. The ξ was set to 0.05. Parameters from table 3.1 were used.

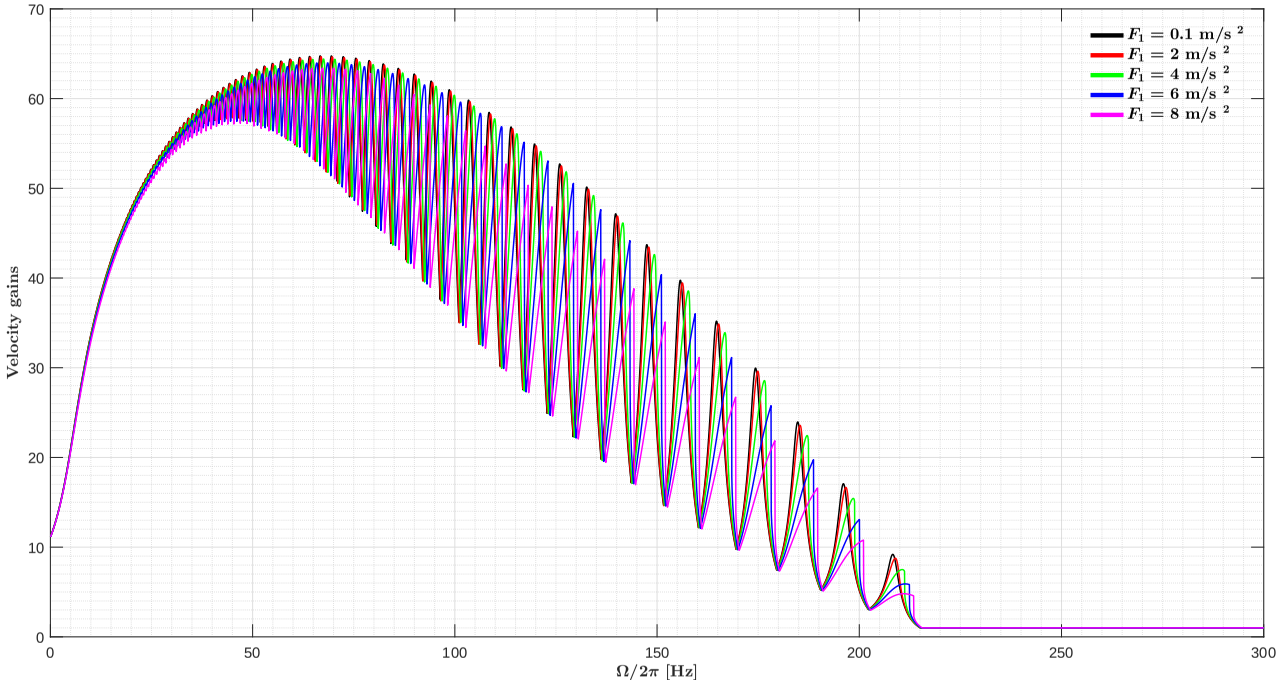

Figure 4.57: Velocity gains according to the external frequency for different excitation amplitudes in which concerns the electromagnetic parametrized harvester. Parameters from table 3.2 were used.

Chapter 5

Discussion and conclusion

Energy harvesting from the oscilations of a levitating magnet mass have a great potential in which converting movement in electric energy is concerned. Their wide variety of functions ranges from implementation in microelectronics, for example, biomedical devices, to macro purposes, such as the sea. The reduced or zero intermittence that autonomous energy harvesting systems exhibit, as well as the low maintenance requirements that arise from the simplicity of both mechanical and electrical architecture result in great advantages. As a result, the application of these systems emerges as remarkable alternative to the use of batteries and other conventional non-renewable energy sources. Predictably, electromagnetic energy harvesters are required to be the most efficient possible. In the attempt to enhance their efficiency, several configurations have been proposed, regarding variations of structural geometry (circular or rectangular section), number of levitating magnets, number of windings, magnet geometry, among others.

Several modulations in the parameters that are directly related to the mechanics of the system are present in the scientific literature, namely empirical, semi analytical, analytical and FEM analysis. The degree of accuracy of each model is dependent on how the constructive parameters are analysed. There is no description of a geometric optimization tool that maximizes the efficiency of the harvesters.

In the present study, by means of a sophisticated method that controls the levitating magnet's dynamics, the length of the generator was made to vary to an optimal value, in order to adapt to excitation variations. This resulted in a tool that ensued the geometrical optimization of the harvester's length to both *a priori* known and variable excitations.

This methodology allows the maximization of the harvester's performance, geometrically optimizing its length prior to its fabrication. It grants adaptive design to no optimized manufacturing, enabling it to be used in harvesters with both fixed length when manufactured (*a priori* known excitation) and variable length (for variable excitations). The adaptive design of the harvester to excitation changes involves low maintenance and no complex mechanical systems. All of these advantages warrant the possibility of optimized operation in a wide range of scenarios and for long time periods.

Nonetheless, this model carries some limitations: both the magnetic field and the electromechanic coefficient are considered as a constant, the electrical damping coefficient is managed as static, the coil's inductance is not introduced in the electrical dynamics, the final solutions are coherent solely if the resistance load is very high (resembling open circuit analysis), it is exclusively valid for limited d_0 variations and it only enables the optimization

of a single parameter.

Overall, an analysis that takes more variables into consideration is still of great importance; the system's dynamics should also be examined using a more complex model that includes the electrical dynamics.

Great improvements in velocity, current and power were obtained. The optimized Δd for certain excitations was identified.

In the future, a system to control the magnetic levitation harvester's physical structure should be developed, in order to magnify the electrical energy produced according to the harvester's dynamics. The possibility of controlling multiple variables is of paramount interest for future researches. Methods to implement this tool ought to be studied relying on a more complex model, which should take the electric dynamics of the system into consideration. The variation of the mass requires greater exploration and has potential to be an issue for future works, since the observed dynamics are not well understood.

Bibliography

[1] Enrico Dallago, Marco Marchesi, and Giuseppe Venchi. "Analytical model of a vibrating electromagnetic harvester considering nonlinear effects". In: *IEEE Transactions on Power Electronics* 25.8 (2010), pp. 1989–1997.

[2] Ahmed Munaz, Byung Chul Lee, and Gwiy Sang Chung. "A study of an electromagnetic energy harvester using multi-pole magnet". In: *Sensors and Actuators, A: Physical* 201 (2013), pp. 134–140.

[3] Krzysztof Kecik, Andrzej Mitura, Stefano Lenci, and Jerzy Warminski. "Energy harvesting from a magnetic levitation system". In: *International Journal of Non-Linear Mechanics* 94 (2017), pp. 200–206.

[4] Marco P. Soares dos Santos, Jorge A. F. Ferreira, José A. O. Simões, Ricardo Pascoal, João Torrão, Xiaozheng Xue, and Edward P. Furlani. "Magnetic levitation-based electromagnetic energy harvesting: a semi-analytical non-linear model for energy transduction". In: *Scientific Reports* 6.1 (2016), p. 18579.

[5] D. F. Berdy, D. J. Valentino, and D. Peroulis. "Kinetic energy harvesting from human walking and running using a magnetic levitation energy harvester". In: *Sensors and Actuators, A: Physical* 222 (2015), pp. 262–271.

[6] M. L. Morgado, L. F. Morgado, N. Silva, and R. Morais. "Mathematical modelling of cylindrical electromagnetic vibration energy harvesters". In: *International Journal of Computer Mathematics* 92.1 (2015), pp. 101–109.

[7] M. Geisler, S. Boisseau, M. Perez, P. Gasnier, J. Willemin, I. Ait-Ali, and S. Perraud. "Human-motion energy harvester for autonomous body area sensors". In: *Smart Materials and Structures* 26.3 (2017).

[8] Abdullah Nammari and Hamzeh Bardaweel. "Design enhancement and non-dimensional analysis of magnetically-levitated nonlinear vibration energy harvesters". In: *Journal of Intelligent Material Systems and Structures* 28.19 (2017), pp. 2810–2822.

[9] Ahmed Haroun, Ichiro Yamada, and Shin'Ichi Warisawa. "Micro electromagnetic vibration energy harvester based on free/impact motion for low frequency-large amplitude operation". In: *Sensors and Actuators, A: Physical* 224 (2015), pp. 87–98.

[10] C. R. Saha, T. O'Donnell, N. Wang, and P. McCloskey. "Electromagnetic generator for harvesting energy from human motion". In: *Sensors and Actuators, A: Physical* 147.1 (2008), pp. 248–253.

[11] P. Carneiro, Marco P. Soares dos Santos, and Jorge A. F. Ferreira. "Levitação magnética na geração autónoma de energia". In: *Proceedings of the 1st Congresso do Centro de Tecnologia Mecânica e Automação* (2018), p. 20.

[12] P. Constantinou, P. H. Mellor, and P. Wilcox. “A model of a magnetically sprung vibration generator for power harvesting applications”. In: *Proceedings of IEEE International Electric Machines and Drives Conference, IEMDC 2007* 1 (2007), pp. 725–730.

[13] Peter Constantinou, Phil H. Mellor, and Paul D. Wilcox. “A magnetically sprung generator for energy harvesting applications”. In: *Journal of Materials Chemistry* 22.28 (2012), p. 14119.

[14] B. P. Mann and N. D. Sims. “Energy harvesting from the nonlinear oscillations of magnetic levitation”. In: *Journal of Sound and Vibration* 319.1-2 (2009), pp. 515–530.

[15] Abu Riduan Md Foisal, Chinsuk Hong, and Gwiy Sang Chung. “Multi-frequency electromagnetic energy harvester using a magnetic spring cantilever”. In: *Sensors and Actuators, A: Physical* 182 (2012), pp. 106–113.

[16] Raul Morais, Nuno M. Silva, Paulo M. Santos, Clara M. Frias, Jorge A.F. Ferreira, António M. Ramos, José A.O. Simões, José M.R. Baptista, and Manuel C. Reis. “Double permanent magnet vibration power generator for smart hip prosthesis”. In: *Sensors and Actuators, A: Physical* 172.1 (2011), pp. 259–268.

[17] D. F. Berdy, D. J. Valentino, and D. Peroulis. “Design and optimization of a magnetically sprung block magnet vibration energy harvester”. In: *Sensors and Actuators, A: Physical* 218 (2014), pp. 69–79.

[18] Wei Wang, Junyi Cao, Nan Zhang, Jing Lin, and Wei Hsin Liao. “Magnetic-spring based energy harvesting from human motions: Design, modeling and experiments”. In: *Energy Conversion and Management* 132 (2017), pp. 189–197.

[19] K. Pancharoen, D. Zhu, and S. P. Beeby. “Temperature dependence of a magnetically levitated electromagnetic vibration energy harvester”. In: *Sensors and Actuators, A: Physical* 256 (2017), pp. 1–11.

[20] E. Arroyo, A. Badel, F. Formosa, Y. Wu, and J. Qiu. “Comparison of electromagnetic and piezoelectric vibration energy harvesters: Model and experiments”. In: *Sensors and Actuators, A: Physical* 183 (2012), pp. 148–156.

[21] Manuel Gutierrez, Amir Shahidi, David Berdy, and Dimitrios Peroulis. “Design and characterization of a low frequency 2-dimensional magnetic levitation kinetic energy harvester”. In: *Sensors and Actuators, A: Physical* 236 (2015), pp. 1–10.

[22] Miah A. Halim, Hyunok Cho, Md Salauddin, and Jae Y. Park. “A miniaturized electromagnetic vibration energy harvester using flux-guided magnet stacks for human-body-induced motion”. In: *Sensors and Actuators, A: Physical* 249 (2016), pp. 23–31.

[23] Masoud Masoumi and Ya Wang. “Repulsive magnetic levitation-based ocean wave energy harvester with variable resonance: Modeling, simulation and experiment”. In: *Journal of Sound and Vibration* 381 (2016), pp. 192–205.

[24] C. Martín Saravia, José M. Ramírez, and Claudio D. Gatti. “A hybrid numerical-analytical approach for modeling levitation based vibration energy harvesters”. In: *Sensors and Actuators, A: Physical* 257 (2017), pp. 20–29.

[25] Martín Saravia and Alex Oberst. “Analysis and Design of Levitation Based Vibration”. In: *Asociación Argentina de Mecánica Computacional* XXXV (2017), pp. 1471–1488.

[26] Abdullah Nammari, Logan Caskey, Johnny Negrete, and Hamzeh Bardaweel. "Fabrication and characterization of non-resonant magneto-mechanical low-frequency vibration energy harvester". In: *Mechanical Systems and Signal Processing* 102 (2018), pp. 298–311.